Journal of Sedimentary Research

Journal of Sedimentary Research, 2021, v. 91, 34–65
Research Article
DOI: 10.2110/jsr.2020.047

INTERACTIONS BETWEEN DEEP-WATER GRAVITY FLOWS AND ACTIVE SALT TECTONICS

ZOË A. CUMBERPATCH,[1] IAN A. KANE,[1] EUAN L. SOUTTER,[1] DAVID M. HODGSON,[2] CHRISTOPHER A-L. JACKSON,*[3] BEN A. KILHAMS,[4] AND YOHANN POPRAWSKI[5]

[1]SedRESQ, Department of Earth and Environmental Sciences, University of Manchester, Oxford Road, Manchester M13 9PL, U.K.
[2]The Stratigraphy Group, School of Earth and Environment, University of Leeds, Leeds LS2 9JT, U.K.
[3]Basins Research Group (BRG), Department of Earth Science & Engineering, Imperial College, London SW7 2BP, U.K.
[4]Shell Upstream International, York Road, London SE1 7LZ, U.K.
[5]LPG-BIAF UMR-CNRS 6112, UNIV Angers, CNRS, UFR Sciences, 2 bd Lavoisier 49045, Angers CEDEX 01, France
e-mail: zoe.cumberpatch@manchester.ac.uk

ABSTRACT: **Behavior of sediment gravity flows can be influenced by seafloor topography associated with salt structures; this can modify the depositional architecture of deep-water sedimentary systems. Typically, salt-influenced deep-water successions are poorly imaged in seismic reflection data, and exhumed systems are rare, hence the detailed sedimentology and stratigraphic architecture of these systems remains poorly understood.**

The exhumed Triassic (Keuper) Bakio and Guernica salt bodies in the Basque–Cantabrian Basin, Spain, were active during deep-water sedimentation. The salt diapirs grew reactively, then passively, during the Aptian–Albian, and are flanked by deep-water carbonate (Aptian–earliest Albian Urgonian Group) and siliciclastic (middle Albian–Cenomanian Black Flysch Group) successions. The study compares the depositional systems in two salt-influenced minibasins, confined (Sollube basin) and partially confined (Jata basin) by actively growing salt diapirs, comparable to salt-influenced minibasins in the subsurface. The presence of a well-exposed halokinetic sequence, with progressive rotation of bedding, beds that pinch out towards topography, soft-sediment deformation, variable paleocurrents, and intercalated debrites indicate that salt grew during deposition. Overall, the Black Flysch Group coarsens and thickens upwards in response to regional axial progradation, which is modulated by laterally derived debrites from halokinetic slopes. The variation in type and number of debrites in the Sollube and Jata basins indicates that the basins had different tectonostratigraphic histories despite their proximity. In the Sollube basin, the routing systems were confined between the two salt structures, eventually depositing amalgamated sandstones in the basin axis. Different facies and architectures are observed in the Jata basin due to partial confinement.

Exposed minibasins are individualized, and facies vary both spatially and temporally in agreement with observations from subsurface salt-influenced basins. Salt-related, active topography and the degree of confinement are shown to be important modifiers of depositional systems, resulting in facies variability, remobilization of deposits, and channelization of flows. The findings are directly applicable to the exploration and development of subsurface energy reservoirs in salt basins globally, enabling better prediction of depositional architecture in areas where seismic imaging is challenging.

INTRODUCTION

The sedimentology and stratigraphic architecture of deep-water systems deposited in unconfined basins (e.g., Johnson et al. 2001; Baas 2004; Hodgson 2009; Prélat et al. 2009; Hodgson et al. 2011; Spychala et al. 2017), or in basins with static or relatively static topography (e.g., Kneller et al. 1991; Haughton 1994; McCaffrey and Kneller 2001; Sinclair and Tomasso 2002; Amy et al. 2004; Soutter et al. 2019), are reasonably well established compared to those in basins influenced by active topography (e.g., Hodgson and Haughton 2004; Cullen et al. 2019).

Seafloor topography is generated by a variety of geological processes, including relief above mass-transport deposits (MTDs) (e.g., Ortiz-Karpf et al. 2015, 2016; Soutter et al. 2018; Cumberpatch et al. 2021), syndepositional tectonic deformation (e.g., Hodgson and Haughton 2004; Kane et al. 2010) and salt diapirism (Fig. 1; e.g., Hodgson et al. 1992; Kane et al. 2012; Prather et al. 2012; Oluboyo et al. 2014). Salt-tectonic deformation influences over 120 basins globally (Hudec and Jackson 2007), including some of the world's largest petroleum-producing provinces (e.g., Booth et al. 2003; Oluboyo et al. 2014; Charles and Ryzhikov 2015; Rodriguez et al. 2018, in press; Grant et al. 2019, 2020a, 2020b; Pichel et al. 2020).

Subsurface studies have shown that salt structures deforming the seafloor can exert substantial control on the location, pathway, and architecture of lobe, channel-fill, levee, and mass-transport deposits (Fig. 1; e.g., Mayall et al. 2006, 2010; Jones et al. 2012; Wu et al. 2020; Howlett et al., in press). Turbidity currents that were ponded, diverted, deflected, and confined by salt structures (Fig. 1) are well documented in the eastern

*Present Address: SedRESQ, Department of Earth and Environmental Sciences, University of Manchester, Oxford Road, Manchester M13 9PL, U.K.

Published Online: January 2021
 1527-1404/21/091-034

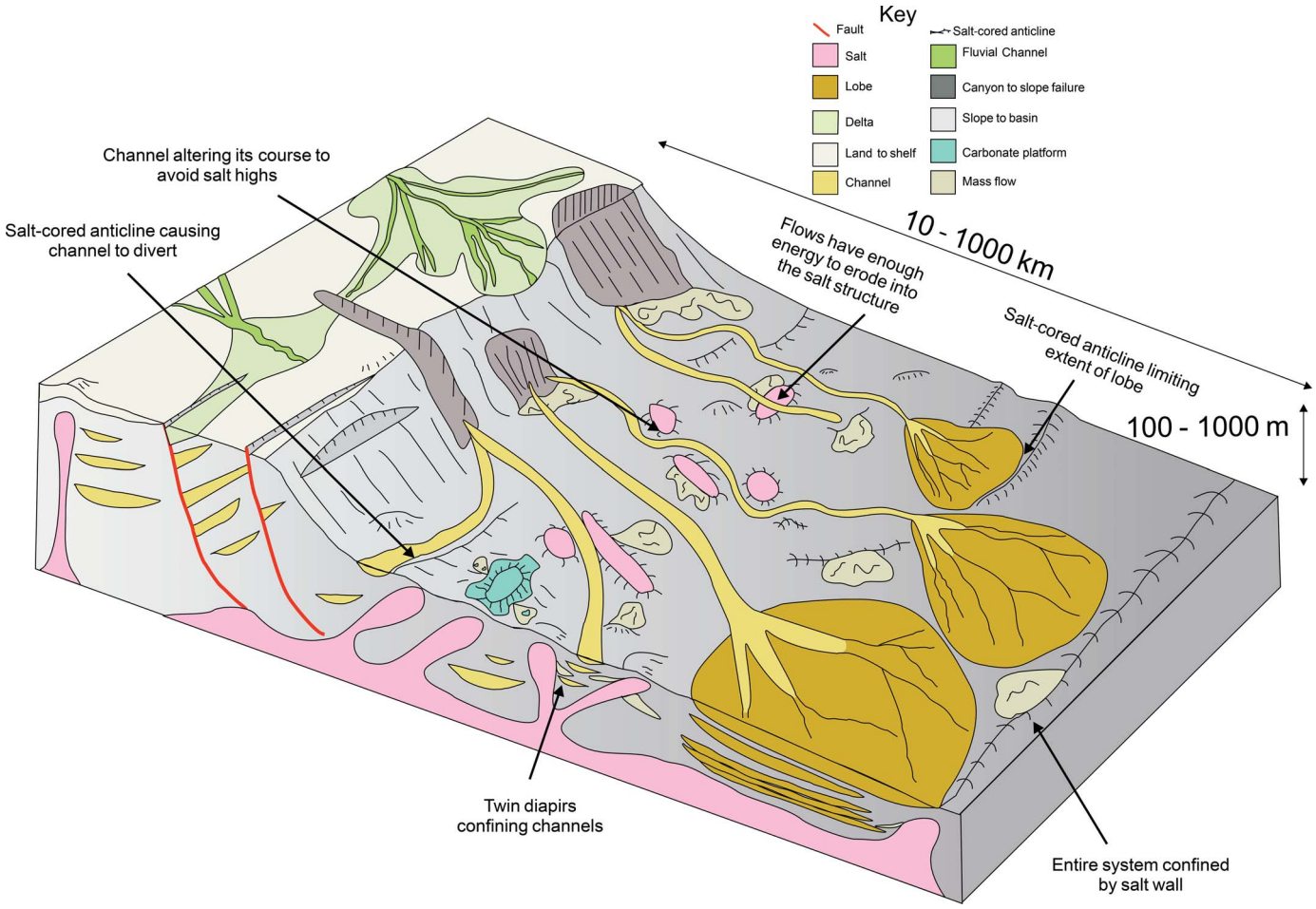

FIG. 1.—Sketch summarizing the structural controls, with respect to gravity-driven processes, on depositional systems from the shelf to basin floor. Note the complex and sinuous paths taken by slope channels around salt structures (Modified from Mayall et al. 2010).

Mediterranean (e.g., Clark and Cartwright 2009, 2011), offshore Angola (e.g., Gee and Gawthorpe 2006, 2007), the Gulf of Mexico (e.g., Booth et al. 2003) offshore Brazil (e.g., Rodriguez et al. 2018, in press), the North Sea (e.g., Mannie et al. 2014), and the Precaspian Basin (e.g., Pichel and Jackson 2020). Successions of genetically related growth strata influenced by near-surface diapiric or extrusive salt form unconformity-bounded packages of thinned and folded strata termed halokinetic sequences, which become composite when stacked (Giles and Rowan 2012; Rowan and Giles 2021). The geometry and stacking of composite sequences are dependent on the interplay between sediment accumulation rate and diapir rise rate. Giles and Rowan (2012) recognize two end-member stacking patterns; tapered (stacked wedge) or tabular (stacked hook).

Typically, salt-influenced successions are poorly imaged in seismic reflection data due to ray path distortion at the salt–sediment interface, steep stratigraphic dips, and deformation associated with salt rise (Davison et al. 2000; Jones and Davison 2014). Due to these complications, our understanding of subsurface salt-influenced systems benefits from their calibration to outcrop analogues (Lerche and Petersen 1995). Exposed examples are rare, largely due to dissolution of associated halites (Jackson and Hudec 2017). Exhumed systems typically contain shallow-marine (e.g., Laudon 1975; Giles and Lawton 2002; Giles and Rowan 2012) or nonmarine (e.g., Banham and Mountney 2013a, 2013b, 2014; Ribes et al. 2015) strata. The Bakio diapir in the Basque–Cantabrian Basin (BCB), northern Spain, provides a rare exhumed example of deep-water strata deposited in a syn-halokinetic setting (Figs. 2, 3; Lotze 1953; Robles et al. 1988; Rowan et al. 2012; Ferrer et al. 2014). The overburden displays well-exposed, unconformity-bounded sedimentary wedges that thin towards and upturn against the diapir, supporting the interpretation of syn-halokinetic growth strata (Poprawski et al. 2014, 2016).

Previous studies in the area have focused on carbonate halokinetic sequences in the middle Albian overburden (Poprawski et al. 2014, 2016), hence the salt-influenced deep-water succession remains poorly understood. This study aims to use large-scale outcrops exposed along the Bakio–Guernica coastline to study the bed-scale flow-topography interactions, deep-water facies distribution, and depositional architecture in salt-controlled minibasins. The objectives of this study are to: 1) reappraise the stratigraphy of the study area using specific deep-water sub-environments, 2) document lateral and vertical changes in deep-water facies and architecture with variable amounts of salt-induced confinement, 3) document the evolution of coeval deep-water axial and debrite-rich lateral depositional systems, and 4) distinguish criteria for the recognition of halokinetically influenced deep-water systems.

GEOLOGICAL SETTING

Evolution of the Basque–Cantabrian Basin (BCB)

The BCB is a peri-cratonic rift basin in northern Spain, inverted during the Campanian–Eocene western Pyrenean Orogeny (Fig. 2; Gómez et al. 2002; Ferrer et al. 2008). The basin is located between the Iberian and

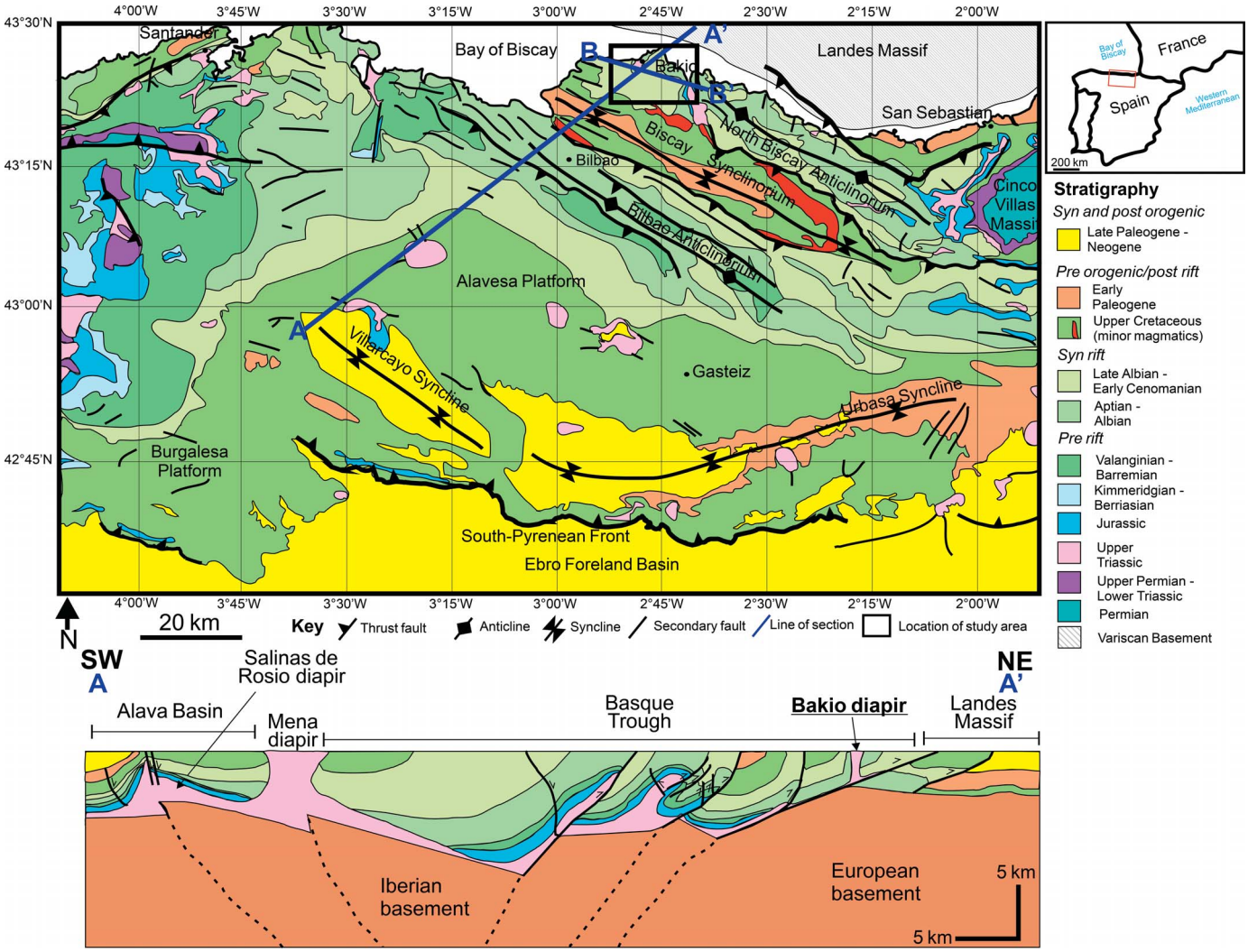

FIG. 2.—Simplified geological map, stratigraphy, and cross-section of the Basque–Cantabrian Basin (BCB), highlighting numerous present-day surface exposures of NE–SW-oriented diapirs (including the Bakio diapir, the focus of this study), commonly flanked by Cretaceous strata. The inset map shows the location of the BCB in northern Spain. Line A–A′ locates cross section and line B–B′ locates Figure 4. Black box locates Figure 3. Stratigraphy indicates mega sequences that can be used to group basin fill (after Ábalos 2016). Cross section is modified from Poprawski et al. (2016).

Eurasian plates and is associated with hyper-extensive rifting and mantle exhumation during the opening of the North Atlantic and the Bay of Biscay (Van der Voo 1969; Brunet 1994; Jammes et al. 2009; DeFelipe et al. 2017; Teixell et al. 2018). The stratigraphy of the BCB is mainly of Mesozoic to Cenozoic age, sourced from a punctuated rift system that existed from Permian–Triassic to Late Cretaceous times (Cámara 2017).

The Mesozoic evolution of the BCB began with the development of a rift system in the Permian–Triassic. During the Carnian–Norian, a thick sequence of mudstones, sabkha evaporites and carbonates accumulated (Keuper Group: Geluk et al. 2018). The Jurassic to Early Cretaceous was characterized by limited subsidence and shallow-water deposition (Martín-Chivelet et al. 2002; García-Mondéjar et al. 2004). Extensional thin-skinned tectonics, controlled by basement faulting, in the Early Cretaceous initiated reactive diapirism across the basin (Bodego and Agirrezabala 2013; Agirrezabala and Dinarés-Turell 2013; Teixell et al. 2018). As rifting continued, the Lower Cretaceous succession preferentially accumulated over downthrown blocks, forming a differential load that triggered a transition into passive diapirism (Agirrezabala and García-Mondéjar 1989; Agirrezabala and López-Horgue 2017). During the Barremian–Albian the flanking minibasins were filled with c. 500 m of mixed carbonates and siliciclastics (García-Mondéjar 1990, 1996). Aptian–middle Albian shallow-water carbonate platforms of Urgonian limestone (García-Mondéjar et al. 2004) formed on the footwalls of tilted normal-fault blocks; these limestones pass abruptly into deeper-water marlstones and mudstones deposited in hanging-wall depocenters (Rosales and Pérez-García 2010). From the late Albian to the early Cenomanian, subsidence combined with early Albian global sea-level rise (Vail et al. 1977; Haq et al. 1987; Robles et al. 1988; Haq 2014) was concurrent with the development of siliciclastic turbidites and redeposited carbonates of the Black Flysch Group (BFG), which are the focus of this study.

As rifting waned, passive diapirs continued to grow at the paleo-seafloor due to minibasin subsidence (Zamora et al. 2017). During the Late Cretaceous to the early Paleogene, subsidence continued and calci-turbidites were deposited (Mathey 1987; Pujalte et al. 1994). Lower Paleocene to Eocene stratigraphy records a gradual transition from mainly calcareous to siliciclastic deposition, with an increase in deposition of siliciclastic turbidites. This change is associated with erosion of the emerging Pyrenean mountain belt (Crimes 1973; Pujalte et al. 1998).

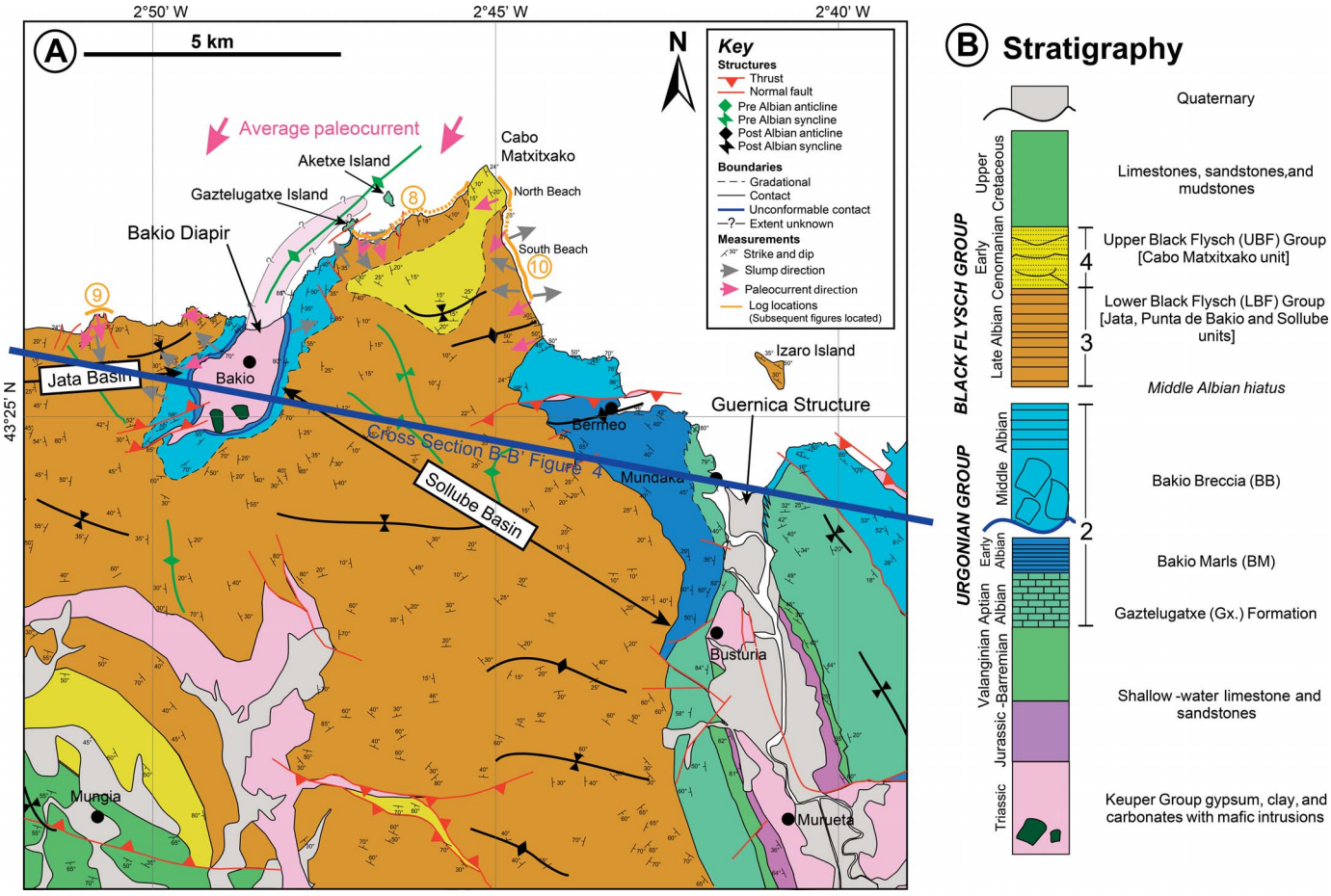

FIG. 3.—A) Geological map located in Figure 2 and B) stratigraphic column for the study area. **A)** Compiled from Espejo and Pastor (1973), Espejo (1973), Garrote-Ruiz et al. (1991, 1992, 1993a, 1993b), Pujalte et al. (1986), García-Mondéjar and Robador (1987), Robles et al. (1988, 1989), Vicente Bravo and Robles (1991a,1991b), Poprawski et al. (2014, 2016), Ábalos (2016), and fieldwork observations. Lateral facies changes in carbonates around the salt outcrops at Guernica are modified from García-Mondéjar and Robador (1987). The Guernica structure has been weathered away and forms a present-day estuary. Orange lines show locations of stratigraphic logs shown in succeeding figures, dashed lines indicate missing section, and numbers refer to subsequent figures where logs are presented. **B)** Abbreviations for stratigraphic units are shown in ( ) and formation names of Poprawski et al. (2014, 2016), where they differ from those used in this study, are shown in [ ]. Numbers adjacent to the stratigraphy refer to regional sequences of Agirrezabala and López-Horgue (2017), based on biostratigraphy. Line of section is shown for Figure 4; for full extent see Figure 2.

Pyrenean NE–SW-oriented compression in Eocene to Oligocene times reactivated Mesozoic–Cenozoic normal faults (Ábalos 2016) and squeezed pre-existing diapirs (Pujalte et al. 1998).

The Bakio and Guernica Salt Bodies

The Bakio diapir is a NE–SW-trending (c. 1 km by 4 km) salt wall of Keuper Group evaporites. Partial exposure of the salt wall occurs at Bakio beach; in other locations the evaporites are easily eroded, typically marked by topographic depressions and/or coastal embayments (e.g., Fig. 3A; the Guernica structure, located c. 9 km to the east). At Bakio beach, the Keuper Group consists of red clays, gypsum, and carbonate, with Triassic-age tholeiitic ophitic inclusions (see Robles et al. 1988; Poprawski et al. 2014). From the middle Albian, the Bakio diapir grew rapidly and reactively in response to regional hyper-extension (Teixell et al. 2018). The diapir then grew passively during the late Albian due to sediment loading, at around 500 m Myr^{-1} (Poprawski et al. 2014).

The Guernica structure is poorly understood due to limited exposure, and hence is referred to as a "salt structure" rather than a salt diapir like Bakio. The Guernica structure has previously been interpreted as a salt-cored anticline (Poprawski and Basile 2018). Vintage onshore seismic reflection data suggest that the basal salt layer is present at depth connecting the Bakio and the Guernica structures (Fig. 4; Robles et al. 1988; Poprawski and Basile 2018). The structures were close to the seafloor during the middle Albian creating highs that were capped by isolated carbonate platforms and influenced the deposition of the BFG (Vicente Bravo and Robles 1991a, 1991b; Pujalte et al. 1986; Cámara 2017; Roca et al. 2020). Slope apron facies, deposited at the platform edge, and subsequent stratigraphy formed tapered halokinetic sequences against the west of the Bakio diapir (Fig. 4; García-Mondéjar and Robador 1987; Soto et al. 2017; Roca et al. 2020).

Bakio Stratigraphy

Studies of magnetic anisotropy in the Bakio–Guernica area demonstrate a minimal Pyrenean compressional overprint to the stratigraphy (Soto et al. 2017), as the tholeiitic ophitic inclusions in the diapir acted as buttresses forming shadow areas protected from the compression. Hence the area is used to study syn-halokinetic deposition without a regional tectonic-deformation overprint.

The Aptian–middle Albian Urgonian stratigraphy (middle Albian Sequence 2: *H. dentatus* Zone of Agirrezabala and López-Horgue 2017)

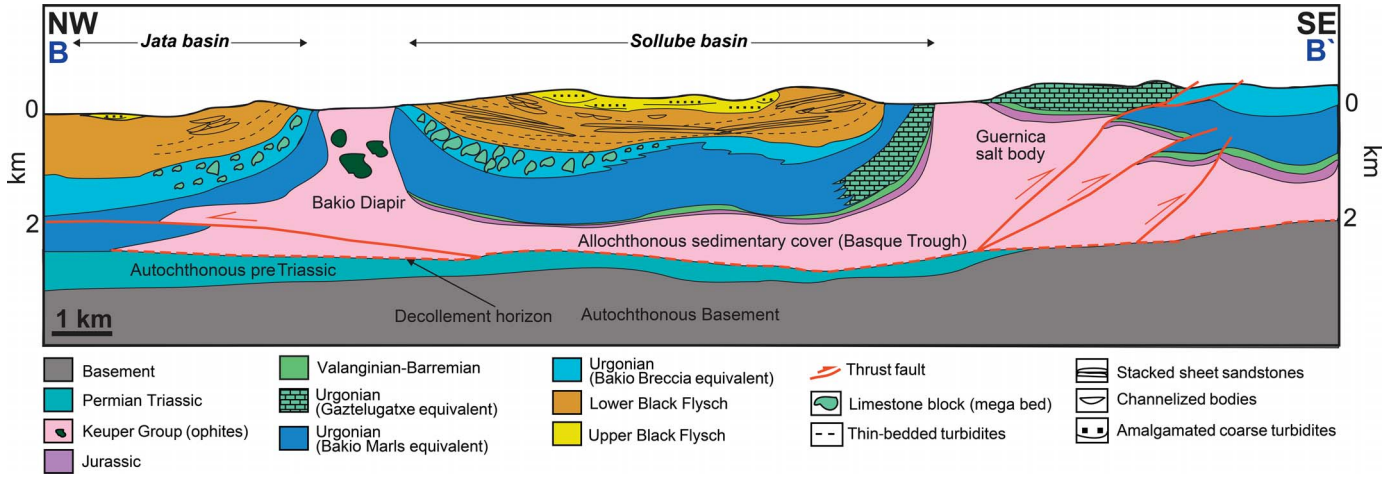

FIG. 4.—Schematic structural–stratigraphic cross section through the Bakio and Guernica diapirs. Full extent is located using B–B′ in Figure 2, partial extent is also shown in Figure 3. The section combines Poprawski and Basile (2018), Robles et al. (1988), field observations, and publicly available vintage onshore seismic lines from IGME. Facies are indicated where known or inferred from the literature but are left blank where they cannot be inferred. Two times vertical exaggeration for clarity.

comprises the Gaztelugatxe, Bakio Marls, and Bakio Breccias formations (Fig. 3B). The Gaztelugatxe Formation (GZF) is a massive-brecciated limestone, interpreted as a karstified platform carbonate (García-Mondéjar and Robador 1987; Robles et al. 1988). The Bakio Marls Formation (BMF) (minimum 60 m thick: Poprawski et al. 2016) comprises thin-bedded calcidebrites deposited in a low-energy mud-dominated environment intermittently punctuated by catastrophic debris flows sourced from local, carbonate-capped highs (García-Mondéjar and Robador 1987; Poprawski et al. 2014). The Bakio Breccias Formation (BBF) is up to 550 m thick and unconformably overlies the BMF (Figs. 3B, 4, Table 1). The BBF is primarily composed of poorly sorted, carbonate breccia beds tens of meters thick (Table 1; García-Mondéjar and Robador 1987; Poprawski et al. 2014, 2016) that are interpreted as earliest middle Albian mass failures from carbonate platforms developed on top of salt structures (Poprawski et al. 2014). The abrupt change from carbonate-dominated to siliciclastic-dominated stratigraphy is associated with a middle Albian hiatus (López-Horgue et al. 2009).

The Urgonian section is overlain by the upper Albian–early Cenomanian BFG, which has been subdivided into a lower and upper unit (Fig. 3B). The Lower Black Flysch Group (LBF) corresponds to the upper Albian Sequence 3 (*D. cristatum–M. inflatum* zones; Agirrezabala and López-Horgue 2017), including the Sollube, Punta de Bakio, and Jata units (Poprawski et al. 2014). This group consists of thin-bedded siliciclastic turbidites, marls, and debrites, and is interpreted to represent a submarine fan system (Robles et al. 1988; Vincente Bravo and Robles 1991, 1995; Poprawski et al. 2014; Roca et al. 2020). The Upper Black Flysch Group (UBF) corresponds to the upper Albian–Cenomanian Sequence 4 (*M. fallax* zone; Agirrezabala and López-Horgue 2017), and the Cabo Matxitxako unit of Poprawski et al. (2014), which consists of thick-bedded, coarse-grained, siliciclastic turbidites deposited in a submarine fan system (Robles et al. 1988, 1989). Provenance studies indicate that BFG sediment was sourced from the northerly Landes Massif, a c. 100 km × 40 km granitic basement block, presently located c. 10 km offshore in the Bay of Biscay (Fig. 2; García-Mondéjar 1996; Puelles et al. 2014).

METHODS AND DATA

The dataset comprises 28 sedimentary logs (totaling 821 m of stratigraphy) collected along the Bakio–Guernica coastline. The logs were collected at a 1:25 scale, with 1:10 scale used locally to capture additional detail. Halokinesis during BFG deposition (García-Mondéjar 1996; Poprawski et al. 2014, 2016; Roca et al. 2020) generated syndepositional basin-floor relief and led to the development of multiple discrete depocenters (Vicente Bravo and Robles 1991a, 1991b, 1995; Agirrezabala 1996). As such, correlating stratal surfaces in and between depocenters is difficult and un-crewed-aerial-vehicle (UAV) photography was used to aid stratigraphic correlations (Hodgetts 2013). Paleocurrent, bedding, and structural data were collected to determine the influence of syndepositional basin-floor relief and to quality-control the pre-existing geological map of Poprawski et al. (2014, 2016). Paleocurrent readings were taken where sedimentary structures were clear enough to permit unambiguous data collection. Sparse biostratigraphic data (Agirrezabala and López-Horgue 2017) hinders correlation across the structures; hence we refer to the Lower (LBF) and Upper (UBF) Black Flysch group only, to avoid further subdivisions based on geographic location (e.g., Robles et al. 1988; Vincente-Bravo and Robles 1991a, 1991b, 1995; Poprawski et al. 2014).

Basin Subdivision

To aid comparison, the study area has been divided into two depocenters: the Jata and Sollube basins (Figs. 3, 4). These are analogous to subsurface minibasins, defined as relatively small (5–30 km) synkinematic depocenters subsiding into thick salt (Hudec and Jackson 2007; Jackson and Hudec 2017). The Jata basin is confined to the east by the Bakio diapir. The Sollube basin is confined on both its western and eastern sides by the Bakio and Guernica structures, respectively (Fig. 3), and hence is more confined than the Jata basin.

LITHOFACIES

This study focuses primarily on the facies variability in the siliciclastic BFG. A description and discussion of the carbonate facies of the BMF and BBF is provided in Poprawski et al. (2016). Here, the carbonate facies are tabulated for reference in Table 1 (and Supplemental Fig. 1) and their depositional process interpreted. The BFG lithofacies presented in Table 2 and in Figure 5 represent "event beds" and are classified based on outcrop observations. "Mud" is used here as a general term, for mixtures of clay, silt, and organic fragments. Where individual facies are heterogeneous, multiple photographs are shown to illustrate this lithological and sedimentological variability (Fig. 5).

TABLE 1.—*Table of carbonate facies detailing the major observations of the six facies which constitute the early Albian Bakio Marls and early middle Albian Bakio Breccias formations. For further discussion see Poprawski et al. (2014, 2016). Supporting facies photographs are provided in supplementary material.*

Facies Name	Description	Interpretation
Thin-bedded calcareous sandstone	0.01–0.1-m-thick beds of bioclastic (corals and shell fragments) very fine-fine grained sandstones. Commonly normally graded with flat tops and flat bases. Weak planar, ripple, and convolute lamination.	**Low-density calci-turbidites:** Thin-bedded structured sandstones deposited from dilute turbidity currents.
Medium-bedded calcareous sandstone	0.1–0.3-m-thick very fine to medium- grained normally graded sandstones, with flat bases and flat tops. Planar, ripple, and convolute lamination observed. Mud clasts and intense dewatering also present.	**Medium to high-density turbidites:** Presence of tractional structures suggests deposition from a dilute turbidity current. High mud-clast percentage could suggest imminent flow transformation (Barker et al. 2008).
Limestone breccia	10+-m-thick beds of matrix- or clast- supported limestone breccia, with erosional bases and undulating tops. Poorly sorted beds consisting of subangular to angular limestone megaclasts, which can be normally, inversely or non-graded. Megaclasts commonly contain entire rudists and fragmented corals.	**Mass-transport deposit:** Poorly sorted clasts suggest deposition from "flow freezing" of a flow with yield strength (Iverson et al. 2010). Limestone clasts are similar in composition to the Gaztelugatxe Limestone, suggesting that it is their source (Poprawski et al. 2014; 2016).
Fossiliferous poorly sorted carbonate mudstone	0.03–0.2-m-thick poorly sorted, non-graded carbonate mudstone with fossil fragments. Beds are laterally discontinuous, with undulose, gradational bases and tops. Cm- to dm-size bioclasts of urchins, brachiopods, bryozoans, bivalves, corals, crinoid stems, and rarer mollusk shell fragments.	**Debris flow:** Fragmented bioclasts, poor sorting, and undulose contacts suggest deposition from a laminar flow (Nardin et al. 1979). Fossils are fragmented, indicating reworking, but are not lithified, indicating direct reworking from an active platform or reef.
Remobilized carbonates	5+-m-thick packages consisting of a combination of the above facies that have been slightly remobilized but maintain bedding planes. Contacts are erosional, scalloped, or smooth, and underlying mudstone units often appear sheared. Convolute lamination and soft-sediment deformation are present.	**Slide deposits:** The remobilization but maintenance of individual bedding planes and sheared basal contacts indicates that these are slide deposits. Lack of internal deformation suggest these deposits have been remobilized post lithification, conceivably due to halokinetic movements (Ferrer et al. 2014; Poprawski et al. 2016).
Clast-rich poorly sorted carbonate mudstone	0.1–1+ m thick poorly sorted beds with angular limestone clasts in a mud-silt matrix. Clasts can be cm to m scale, generally 1–12 cm, and are rich in mollusk fragments. Rare lithics and organics are observed. Undulose tops reflect clast topography and, bases are flat, weakly-erosional or undulose. Weak normal grading and rarer reverse grading are observed.	**Carbonate-clast-rich debrites:** Poor-sorting and large clast size indicates en-masse deposition from a laminar flow (Nardin et al. 1979; Iverson 1997; Sohn 2000) Weak normal grading suggests that some turbulence was influencing the flow. Clast angularity suggests proximity to source area. Lack of unconsolidated fossil debris suggests that lithification has occurred before reworking into the flow.

INTERPRETATION OF DEPOSITIONAL ELEMENTS

Facies associations (Table 3, Fig. 6) and architectures (Table 4, Fig. 7) are integrated to support interpretation of depositional environment. Facies associations are interpreted based on dominant lithofacies (Table 2, Fig. 5) and use lobe (Prélat et al. 2009; Spychala et al. 2017) and channel–levee (Kane and Hodgson 2011; Hubbard et al. 2014) nomenclature that best fit field observations. Facies associations and geometries are described separately, because architecture alone is not diagnostic of the depositional sub-environment, and multiple facies associations can form a similar architecture.

STRATIGRAPHIC EVOLUTION

Extensive exposures permit detailed lithostratigraphic analysis (Figs. 3, 8, 9, 10), allowing investigation of the role of salt-induced relief on depositional patterns (Figs. 11, 12, 13). The following sections describe the exposures from oldest to youngest, first focusing on the flanks of the Sollube and Jata basins (Gaztelugatxe Island and Bakio West Bay, respectively) and then the axis of the Sollube basin (Cabo Matxitxako).

Gaztelugatxe Island

The cliff sections to the south of Gaztelugatxe Island (located in Fig. 3) provide a semi-continuous section through 120 meters of the BFG, 2 km northeast of the exposed Bakio diapir, and c. 9 km northwest of the Guernica structure. The stratigraphy is subdivided into five lithostratigraphic units (GX1–5).

Description.—GX1 is 8 m thick and consists of bioturbated mudstones, calci-debrites, calci-turbidites, thin-bedded turbidites, and mud-rich debrites. It shows an overall coarsening- and thickening-upwards from centimeter- to meter-scale interbeds of each facies. GX2 is 10 m thick and dominated by carbonate–clastic debrites, with angular clasts of the Gaztelugatxe Limestone, up to 1 m in diameter. GX2 pinches out downslope, forming a triangular geometry (Table 4, Fig. 7E). GX3, has a minimum thickness of 42 m, onlaps GX2 and is recognized as the first purely siliciclastic succession; comprising thin- to medium- bedded turbidites, debrites, hybrid beds, and bioturbated mudstones. GX4 has a minimum thickness of 9 m, and its base is marked by a meter-thick slump,

TABLE 2.—*Table of siliciclastic facies detailing the ten facies that comprise the Black Flysch Group.*

Facies Name	Description	Interpretation
Granular-cobbly sandstones	0.1–1.5+-m thick beds of granular-cobble sandstones (Fig. 5A, B), with subangular (Fig. 5B) to well-rounded, moderately sorted clasts. Weak cross-stratification (Fig. 5A), pebble imbrication, amalgamation, mud clasts and erosional surfaces (Fig. 5A, B) are observed. Dish structuration is pervasive (Fig. 5A).	**High-density turbidites:** The coarse grain size, thick beds, and amalgamation surfaces suggest deposition from a highly concentrated turbulent flow, indicating that these beds are turbidites. Weak stratification indicates traction-carpet deposition (Lowe 1982), suggesting high-density turbidites.
Thick-bedded sandstones	0.5–1+-m-thick beds of very-fine-to coarse-grained normally graded sandstones, which lack primary depositional structures and are commonly dewatered (Fig. 5C). Bases can be sharp, erosional, stepped, or amalgamated, commonly along a mudstone amalgamation surface with a subtle grain-size break (Fig. 5C), and tops are often flat. Plane-parallel lamination, mud clasts, and soft-sediment deformation are occasionally observed.	**High-density turbidites:** The general massive structuration of these deposits suggests that they represent rapid aggradation beneath a highly concentrated flow (Lowe 1982).
Medium-bedded sandstones	0.1–0.5-m-thick beds of very fine-medium grained, normally graded sandstones. Beds are rich in tractional structures, particularly plane parallel laminations (Fig. 5D). Ripple laminations is observed in bed tops, and beds are more frequently structureless towards bases. Bed bases are flat with tool marks or loaded, and tops are flat or convolute and often rich in mud clasts (Fig. 5D). Occasionally amalgamated.	**Medium-density turbidites:** Based on their tractional structures and normal grading, beds of this lithofacies are interpreted as deposition from a dilute turbidity current. These beds are interpreted as medium-density turbidites due to their bed thickness and common lack of structures in the lower part of the bed.
Thin-bedded sandstones	0.01–0.1-m-thick beds of very fine-fine, normally graded sandstones. Rich in tractional structures, particularly plane- parallel lamination (Fig. 5E, F). Banding on a sub-cm scale (Fig. 5E, F) and convolute lamination are common. Bases are flat (Fig. 5F), undulose, loaded (Fig. 5E, F), or weakly erosional and tops are flat to undulose and rich in mud clasts. Starved, climbing, and opposing paleoflow ripples are observed (Fig. 5E).	**Low-density turbidites:** Tractional structures and normal grading indicate deposition from a dilute turbidity current and are therefore interpreted as low-density turbidites. Common banding may reflect some periodic suppression of turbulence associated with flow deceleration or increased concentration (Lowe and Guy 2000; Barker et al. 2008). Ripples with opposing paleoflow suggests topographic interference.
Siltstone and very thin-bedded sandstones	Packages of 0.1 m composed of individual fine siltstone to fine sandstone events less than 0.01 m. Beds form discontinuous drapes within mudstone (Fig. 5G), with flat bases and flat tops. Parallel and ripple lamination and diagenetic phosphate nodules are observed (Fig. 5G).	**Low-density turbidites:** Fine grain size and thin bed thickness suggest that this unit represents deposition from dilute turbidity currents (Boulesteix et al. 2019), representing lower-energy conditions than thin-bedded sandstones.
Mudstone	0.01–5-m-thick mudstone to fine siltstone beds of carbonate or siliciclastic mudstone (Fig. 5H). Weakly planar-laminated, friable packages (Fig. 5H) with drapes and discontinuous lenses of siltstone (Fig. 5H). *Nereites* bioturbation and diagenetic spherical cm-scale phosphate nodules present.	**Background sedimentation:** Fine grain size indicates low-energy conditions, representative of background sedimentation via suspension fallout. Discontinuous siltstones suggest that lamination may be present below the scale visible in outcrop, representing deposition from a dilute turbidity current (Boulesteix et al. 2019).
Poorly-sorted mudstone	0.1–1+-m-thick siltstone to fine-sandstone rich mudstones (Fig. 5I). Poorly sorted, matrix-supported, clast-rich deposit with starry-night texture. Granules, organic fragments, mud clasts and rare shelly fragments present, often with subtle alignment. Bases are flat or undulose, tops flat or loaded (Fig. 5I).	**Mud-rich debrites:** The poorly sorted matrix and clast-rich nature indicates en-masse deposition from a laminar flow (Nardin et al. 1979).
Poorly-sorted muddy sandstone	0.1–1+-m-thick, mud-rich poorly sorted matrix-supported, fine to medium grained sandstones with starry-night texture (Fig. 5J). Organized mudstone clasts and sporadic granules to pebbles are observed. Flat-undulose tops and flat-graded base are common (Fig. 5J). Rare normal grading and grain-size segregation and infrequent sheared layers present.	**Sand-rich debrites:** En-masse deposition from a laminar flow (Nardin et al. 1979; Iverson 1997; Sohn 2000). Weak normal-grading suggests that some turbulence was influencing the flow and therefore deposition from a transitional flow regime is interpreted (Baas et al. 2009, 2013; Sumner et al. 2013).
Chaotic clast-rich matrix supported deposit	0.5–3-m-thick, poorly sorted deposit with a poorly sorted matrix of mudstone to fine sandstone. Clasts include: cm- to m-scale sandstone balls (Fig. 5K), showing internal lamination and soft-sediment deformation, dm–m scale sandstone and heterolithic subangular rafts, deformed siderite nodules, limestone clasts, gastropod and sponge fragments, mud clasts, and phosphate nodules. Beds are flat-topped, and bases are weakly loaded (Fig. 5K).	**Mega-debrites:** The poorly sorted matrix and large clast size are suggestive of "flow freezing" indicating deposition in a debris-flow regime (Iverson et al. 2010). These deposits are interpreted as mega-debrites due to their large clast size (rafts), suggesting they are derived from localized mass failure.
Bipartite or tripartite beds	0.1–1.5-m-thick beds that contain multiple parts (Fig. 5L, M). Typically consisting of a lower fine-medium sandstone (division 1) overlain by a poorly sorted, muddy siltstone–sandstone (division 2) with a flat to slightly undulose base (Fig. 5L, M). Division 3 is sometimes present, consisting of cleaner siltstone or fine-grained sandstone loaded into division 2 (Fig. 5L). Division 1 can contain planar lamination and weak cross-stratification (Fig. 5L) but is often massive with sporadic-slightly organized mud clasts (Fig. 5M). Division 2 is organic-rich, highly deformed, and can contain sporadic granules or pebbles (Fig. 5L, M). Starry-night texture is observed in this division. Division 3 is more frequently planar laminated than division 1 but can be highly chaotic (Fig. 5L).	**Hybrid beds:** Tractional structures in division 1 and 3 suggest that these deposits formed under turbulent flows. Starry-night texture, poor sorting, and mud content suggest that division 2 was deposited under a transitional-laminar flow regime (Haughton et al. 2009). Flow transformation from turbulent to laminar can occur through flow decelerations (Barker et al. 2008; Patacci et al. 2014) or by an increase in concentration of fines during flow run-out (Kane et al. 2017).

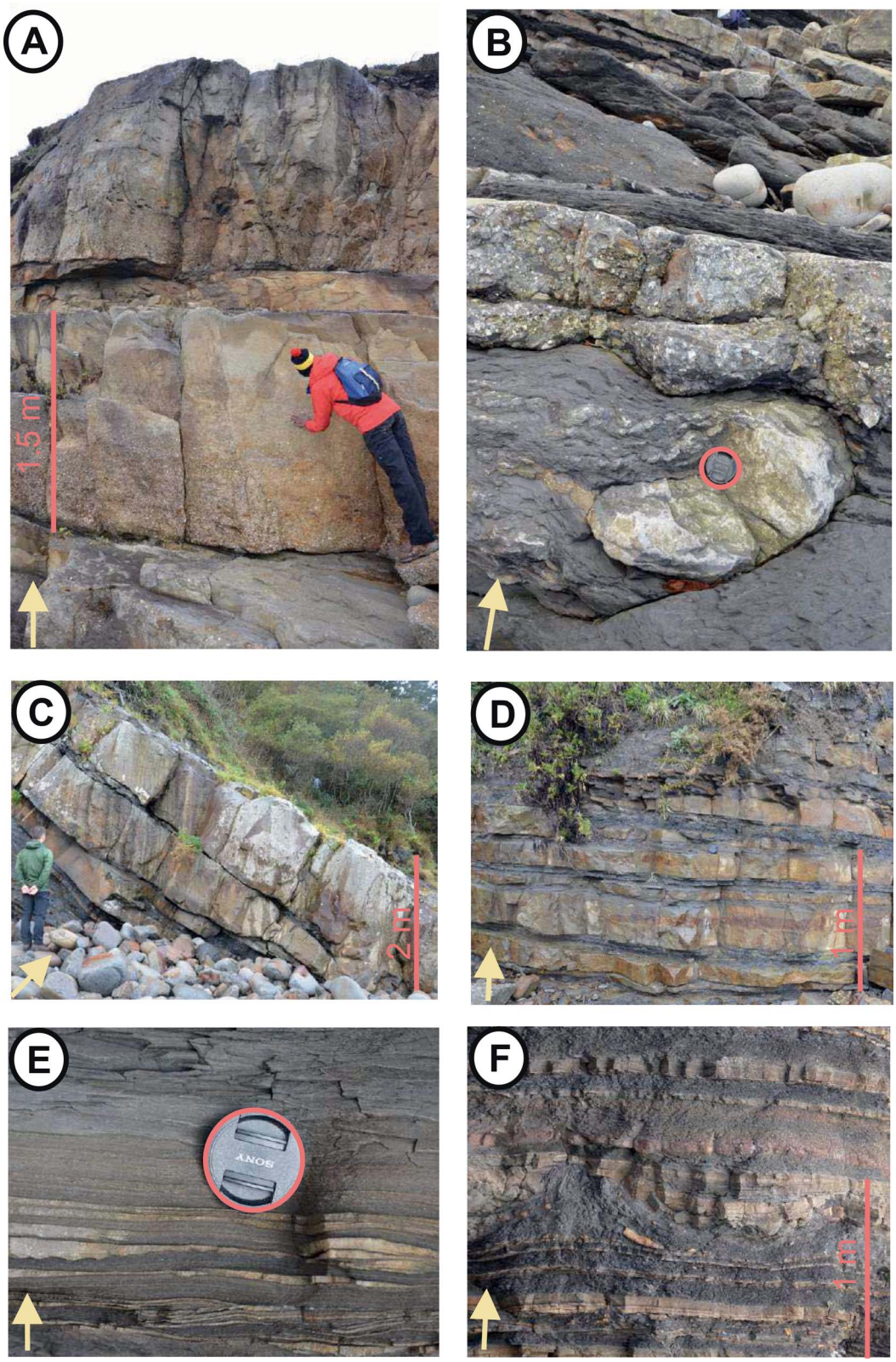

FIG. 5.—Siliciclastic facies photographs. Yellow arrow indicates way up. Peach outline highlights scale, either lens cap (52 mm), or indicated. **A)** Granular-cobbly laterally extensive thick sandstone beds. **B)** Granular-cobbly sandstone with medium-thickness beds exhibiting lateral facies variations. **C)** Stacked, amalgamated thick-bedded sandstones. **D)** Medium-bedded sandstones interspersed with mudstones and poorly sorted mudstones and sandstones. **E)** Thin-bedded sandstone showing ripples, planar lamination, and loading. **F)** Succession of stacked thin-bedded sandstones. **G)** Siltstone and very-thin-bedded sandstones; phosphate nodules are common in this facies. **H)** Mudstone with occasional, rare drapes of siltstone. **I)** Poorly sorted mudstone, foundered into by a thick-bedded sandstone. **J)** Poorly sorted muddy sandstone, containing sporadic granules and raft blocks. **K)** Chaotic clast-rich matrix-supported deposit encased between units of thin-to-medium-bedded sandstones. **L)** Tripartite bed consisting of lower medium-bedded sandstone with weak cross-lamination, middle poorly sorted mudstone and upper poorly sorted sandstone. **M)** Bipartite bed consisting of lower thick-bedded sandstone which becomes mud-clast rich upwards overlain by a poorly sorted mudstone above.

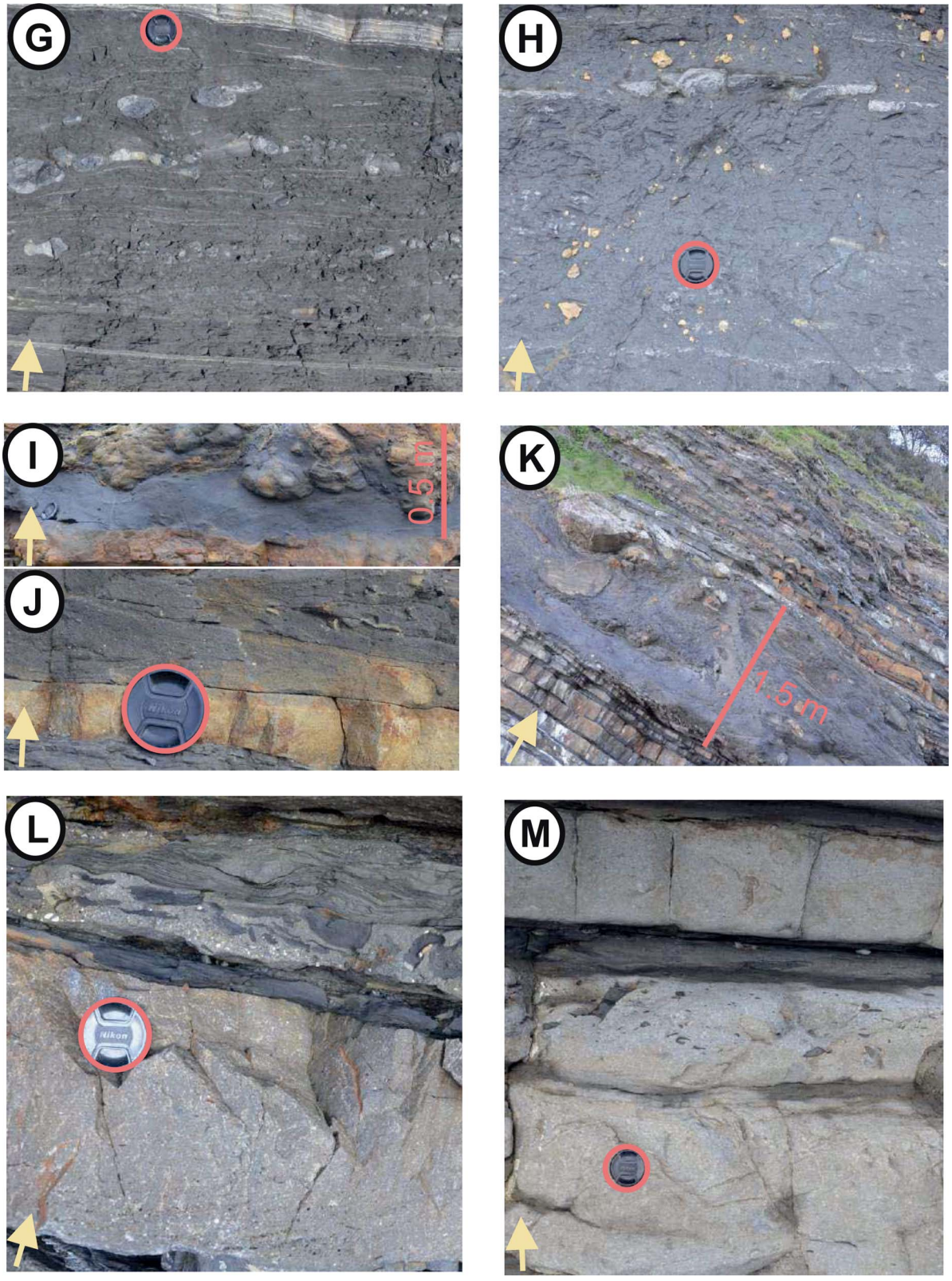

FIG. 5.—Continued.

TABLE 3.—*Table of facies association detailing the assemblages that constitute the Black Flysch Group.*

Facies Association Name	Description	Interpretation	Architecture (Table 4; Fig. 7)
Lobe axis	Dominantly thick-bedded sandstones (Fig. 6, 7C) with subordinate medium-bedded (Fig. 5D), thin-bedded (Fig. 5E, F), and granular-cobbly sandstones (Fig. 6). Beds are often massive and amalgamated (Fig. 6) with pervasive dewatering, frequent mud clasts, and subtle normal grading (Fig. 5C). Thin-bedded granular-cobbly sandstones can underlie thick-bedded sandstones or form isolated lenticular geometries (Fig. 5B).	Thick-bedded nature suggests deposition from high concentration turbidity currents with relatively high rates of aggradation preventing the development of tractional sedimentary structures (Kneller and Bramney 1995; Talling et al. 2012). Common amalgamation and entrainment of mudstones clasts in thick-bedded sandstones indicate that the parent flows were highly energetic and capable of eroding, entraining, and bypassing sediment during the passage of flow (Lowe 1982; Mutti 1992; Stevenson et al. 2015). Similar deposits elsewhere have been interpreted as lobe-axis deposition (Walker 1978; Prélat et al. 2009; Kane et al. 2017). Thin-bedded granular-cobbly sandstones are associated with overlying and adjacent amalgamated thick-bedded sandstones and are thought to represent a mostly bypassing equivalent of the depositional thick-bedded sandstones within the lobe axes (Kane et al. 2009).	Pinching out upslope (Fig. 7C) or convex up (Fig. 6)
Lobe off-axis	Composed principally of normally graded structured to structureless medium-bedded sandstones (Fig. 5D) with less common thin-bedded (Fig. 5F) and thick-bedded sandstones (Fig. 5C). Ripples at the tops of beds commonly show paleoflow directions opposite to those that are measured from flutes and grooves on bed bases. Mudstones, poorly sorted mudstones, sand-rich mudstones, and rarer chaotic clast-rich matrix-supported deposits are periodically or randomly interspersed in this facies association (Fig. 6).	A medium-density turbidite interpretation is given for these units based on the preservation of both structured and structureless sandstones. Similar preservation of both deposit types has been interpreted as off-axis lobe environments, deposited by decelerating turbidity currents (Prélat et al. 2009; Spychala et al. 2017; Soutter et al. 2019). Opposing paleocurrent directions in event beds is characteristic of topographically influenced flows (Kneller et al. 1991; Bakke et al. 2013). Periodic deposition of mudstones suggests episodic system shutdown. Poorly sorted mudstones, sand-rich mudstones, and chaotic clast-rich matrix supported deposit occurrence indicate periodic laminar flows which could indicate nearby active topography (Kneller et al. 1991; Mayall et al. 2010).	Pinching out upslope (Fig. 7C) or convex up (Fig. 6)
Proximal fringe	Consists principally of thin-bedded sandstones (Fig. 5E, F) and bipartite or tripartite event beds (Fig. 5L, M). Siltstone and very-thin-bedded sandstones and medium-bedded-sandstones (Fig. 6) are infrequently observed. Poorly sorted mudstones, sand-rich mudstones, and rarer chaotic clast-rich matrix-supported deposits are periodically or randomly interspersed in the otherwise organized thin-bedded sandstones and bipartite or tripartite beds (Fig. 6).	Thin-bedded, structured sandstones are interpreted to be deposited from low-concentration turbidity currents (Mutti 1992; Jobe et al. 2012; Talling et al. 2012). Bipartite and tripartite event beds are interpreted as hybrid beds (Haughton et al. 2009). The transformation of flows in hybrid beds observed here document a change in flow process from high-medium-concentration turbulent to laminar or transitional, to low-concentration turbulent (Remacha et al. 2005; Baas et al. 2011). Thin-bedded sandstones and hybrid beds underlie lobe and lobe-axis facies associations and are therefore interpreted to be deposited adjacent to such deposits. Abundant hybrid beds and thin beds indicate lobe-fringe deposition elsewhere (Hodgson 2009; Jackson and Johnson 2009; Kane et al. 2017; Soutter et al. 2019), specifically in the proximal fringe (Sypchala et al. 2017). In tectonically confined settings, flow types are highly variable and the frontal and lateral fringe can be difficult to decipher because flow transformation is influenced by topography so hybrid beds can be common in the lateral and frontal fringe (Barker et al. 2008; Soutter et al. 2019) termed "proximal fringe."	Tabular (Fig. 7A) or pinching out up slope (Fig.7C).
Distal fringe	Dominated by siltstone and very-thin-bedded sandstones (Fig. 5G) and mudstones (Fig. 5H) with secondary thin-bedded sandstones, bipartite and tripartite beds, and thin-bedded poorly sorted mudstones (Fig. 6). Mudstones separating individual events are often slightly deformed or sheared and show drapes of discontinuous siltstone (Fig. 6).	The fine grain size, thin-bedded character, and low stratigraphic position of these beds is consistent with lobe-fringe deposition. The relative lack of hybrid beds in this facies association support a distal-lobe-fringe interpretation (Hodgson 2009; Jackson et al. 2009; Kane et al. 2017; Soutter et al. 2019), specifically in the proximal fringe (Sypchala et al. 2017).	Tabular (Fig. 7A)

overlain by interbeds (centimeter to decimeter scale) of turbidites, debrites, slumps, slides, hybrid beds, and mudstones.

GX5 is identified on the western side of Cabo Matxitxako (Fig. 8), having a minimum thickness of 30 m. There is approximately 400 meters of missing stratigraphy between GX4 and 5 (Robles et al. 1988), but GX5 is projected to lie stratigraphically above GX4. GX5 comprises predominantly amalgamated medium- to high-density turbidites showing evidence of soft-sediment deformation.

TABLE 3.—*Continued.*

Facies Association Name	Description	Interpretation	Architecture (Table 4; Fig. 7)
Channel–lobe transition zone	Consists of granular-cobbly sandstones (Fig. 5A) and intensely dewatered thick-bedded sandstones up to 5 m thick (Fig. 5C). Erosional bases, mega-flutes, stepped amalgamation surfaces, and mud-clast abundance are common (Fig. 6). Granular-cobbly sandstone lenses infilling lensoid, spoon-shaped depressions are observed (Fig. 6). Weakly stratified cross-lamination of gravels in sandstone matrix and pebble imbrication is also observed (Fig. 5A, 8). Low-wavelength hummock-like structures are observed (Fig. 6) (Vincente Bravo and Robles 1991).	Erosionally based geobodies infilled with coarser clasts indicate active erosion and deposition. Common amalgamation and entrainment of mudstones clasts in thick-bedded sandstones indicate that the parent flows were highly energetic and capable of eroding, entraining, and bypassing sediment during the passage of flow (Lowe 1982; Mutti 1992; Stevenson et al. 2015), while weak cross-stratification, slight grading, and pebble imbrication are more typical of depositional conditions (Mutti and Normark 1987). This juxtaposition of depositional and erosional elements has been observed elsewhere in channel–lobe transition zones (Mutti and Normark 1987; Wynn et al. 2002; Pemberton et al. 2016; Brooks et al. 2018). The presence of cross-stratified gravels supports the facies association proposed by previous work (Vincente Bravo and Robles 1991a; 1991b; 1995).	Tabular amalgamated beds (Fig. 7G)
Channel-axis	Thick-bedded sandstones (Fig. 5C), granular-cobbly sandstones (Fig. 5A), poorly sorted muddy sandstones (Fig. 5I), and chaotic clast-rich matrix-supported deposits (Fig. 5K). Thick-bedded sandstones typically gradationally overlie granular-cobbly sandstones, which are commonly grooved on the base, showing normal grading (Fig. 6). These successions are erosional into the underlying poorly sorted muddy sandstones or chaotic clast-rich matrix supported deposits, which exhibit some deformation and shearing (Fig. 6). Sandstone beds either erode into each other, are amalgamated, or less commonly are separated by thin beds of mudstone (Fig. 6). Low-angle cross-stratification is observed (Fig. 5A). The sandy mudstones and chaotic units contain subangular to angular poorly sorted clasts of up to boulder size. The composition of these clasts includes limestone fragments, organics, siliciclastic fragments, slumped and reworked thin-bedded heterolithics, clasts of granite, deformed and reworked siderite, mud clasts, and fossil fragments (Fig. 6).	Common amalgamation, erosion, and entrainment of clasts in the sandstones indicate that the parent flows were highly energetic and capable of eroding, entraining, and bypassing sediment (Mutti 1992; Stevenson et al. 2015; Soutter et al. 2019). The coarse grain size and basal location of granular-cobbly sandstones suggests that these beds were deposited as a coarse-grained lag in a bypass-dominated regime (Hubbard et al. 2014). Erosionally based lenticular sandstones and their grading from cobbly–fine sandstone is consistent with deposition in a submarine channel described elsewhere (Hubbard et al. 2008; Romans et al. 2011; McArthur et al. 2020). Weak low-angle lamination in sandstone beds could indicate lateral accretion (Kane et al. 2010; Jobe et al. 2016). Poorly sorted muddy sandstones and chaotic units could represent channel collapse and margin failure (Flint and Hodgson 2005; Pringle et al. 2010; Jobe et al. 2017). The wide variation in clast composition, more diverse than that observed in any other facies association, indicates broader catchment area for these debris flows, which may indicate an extrabasinal provenance (Stevenson et al. 2015).	Concave upward (Figs. 6, 7B)
Channel-margin	Thin-bedded sandstones (Fig. 5E, F) and poorly sorted mudstones with secondary medium-bedded sandstones and chaotic clast-rich matrix-supported deposits (Fig. 6). Thin- and medium-bedded sandstones are planar and ripple laminated (Fig. 5E). Poorly sorted mudstones and chaotic clast-rich matrix-supported deposits include angular to rounded clasts of limestone, siliciclastic fragments, and mud clasts. Medium-bedded sandstones erode into the tops of chaotic clast-rich matrix-supported deposits, and thin-bedded sandstones show loaded, flat and weakly erosional bases. This facies association appears beneath the channel-axis facies associations (Fig. 6).	The supercritical bedforms and thin-bedded nature of these deposits is similar to those described as channel-margin facies by others (Kane and Hogdson 2011; Hodgson et al. 2011; Hubbard et al. 2014; Jobe et al. 2017; McArthur et al. 2020). The location of this facies association beneath channel-axis deposits suggests that they were deposited adjacent to them, and this indicates they represent channel-margin facies association.	Tabular (Figs. 6, 7A)

Interpretation.—The presence of siliciclastic and calci-turbidite deposits and debrites in GX1 (Fig. 8) suggests a transition from the upper BBF to the LBF (Fig. 12C: Poprawski et al. 2014, 2016). The carbonate deposits could have been remobilized from previous BBF deposits or remnant carbonate highs (Poprawski et al. 2014, 2016). GX2 represents a period of increased mass failure, which is interpreted to be halokinetically driven due to the lentil-shape and diapir-centric distribution of these limestone breccias (Table 4: Fig. 7E; e.g., McBride et al. 1974; Hunnicutt 1998; Giles and Lawton 2002). The thin-bedded nature and presence of hybrid beds in GX3 suggests early BFG deposition in a proximal lobe-fringe environment (Spychala et al. 2017; Soutter et al. 2019). Thin-bedded debrites are interpreted to be delivered axially, based on their association with thin-bedded turbidites that show regional paleocurrents. Thick-bedded, chaotic, clast-rich units are interpreted to be halokinetically driven based on variable slump-axis paleocurrent readings (Poprawski et al. 2014).

At the base of GX4, a meter-scale debrite overlies 30 m of missing section (Fig. 8), which given the low-lying geomorphology is likely mud-rich. The overlying turbidites and debrites suggest deposition in a lobe off-axis setting (Prélat et al. 2009; Spychala et al. 2017) where the seafloor was, at least periodically, unstable (Fig. 12E). Meter-thick beds that stack into 30-meter-thick packages suggest that GX5 represents deposition in the

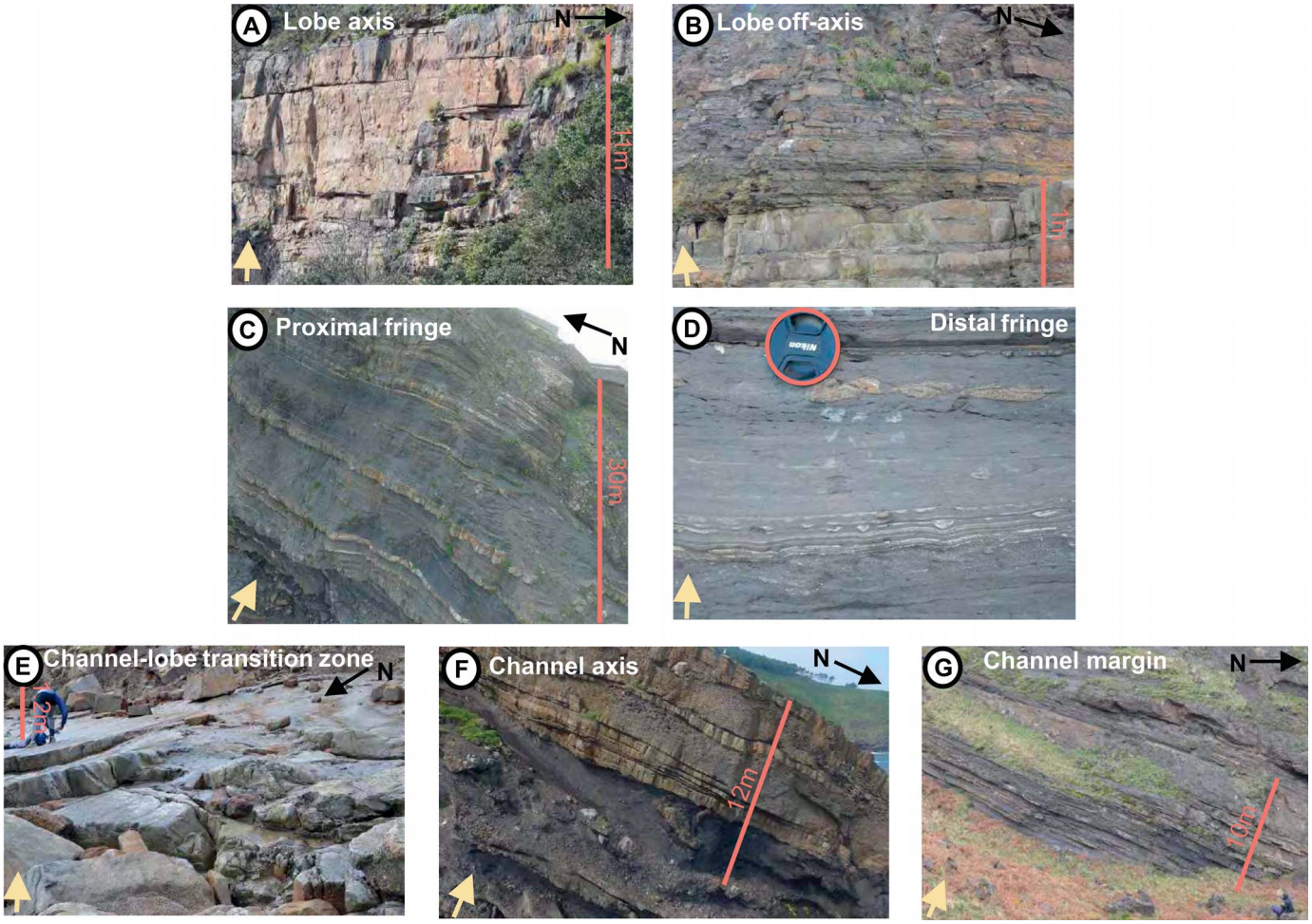

FIG. 6.—Type examples of the seven documented facies associations in this study (Table 3). Peach highlights scale, either lens cap (52 mm), or indicated. Black arrow points to the north, and yellow shows the way up. **A)** Thick-bedded sandstones of the lobe axis. **B)** Interbedded sandstones and mudstones of the lobe off-axis. **C)** Thin-bedded sandstones interbedded with mudstones of the proximal fringe. **D)** Mudstones and very thin-bedded sandstones and siltstones of the distal fringe. **E)** Thick-bedded granular sandstones of the channel–lobe transition zone. **F)** Sandstones and poorly sorted mudstones of the channel axis. **G)** Thin-bedded sandstones interbedded with mudstones of the channel margin.

axis of a lobe complex (Fig. 12F: Prélat et al. 2009; Soutter et al. 2019). The absence of debrites or slumps in GX5 (Fig. 8) suggests minimal halokinetic influence, either due to diapir inactivity or sediment accumulation, due to uplift and erosion from the Landes Massif (Agirrezabala 1996), outpacing the rate of seafloor deformation. The presence of amalgamated, laterally extensive medium- and high-density turbidites in GX5 supports deposition in a channel–lobe transition zone (Vincente Bravo and Robles 1991a, 1991b, 1995) or lobe-axis setting.

Bakio West Bay

The coastal cliff section at Bakio West Bay (Fig. 9) exposes c. 150 m of the BFG above its basal contact with the BBF (Robles et al. 1988), c. 1 km west of the Bakio diapir. This section is divided lithostratigraphically into three units (BW1–3), and is further divided by halokinetically driven unconformities into sub-units (Fig. 9; Poprawski et al. 2014).

Description.—BW1 is 6-meter-thick, consists of calciturbidites and siliciclastic turbidites, debrites, and mudstones, and is overlain by BW2 across an angular unconformity (U2; Fig. 9A; Poprawski et al. 2014). BW2 is principally siliciclastic, comprising predominantly turbidites, with minor debrites and mudstones. A 10-meter-thick package of fine sand- to pebble-grade turbidites with lenticular geometries and scoured-amalgamated bases is observed to overlie a 2-meter-thick debrite (Fig. 9A). BW3 consists of interbedded meter-scale siliciclastic turbidites and debrites (Fig. 9B). Unconformities 5 and 6 are intra-BW3, and thus BW3 is subdivided into three sub-units (BW3a, b, and c).

At the bases of BW3a, BW3b, and BW3c, 1–12-meter-thick debrites with variable thickness across the exposure overlie the angular unconformity (Fig. 9). Grain size varies from medium sand to boulders and clasts vary from rounded to angular. A more diverse range of clast rock types than elsewhere in the study area are observed, including limestone, sandstone, mudstone, organics, heterolithics, siderite, mafic material, granite, and siderite (Table 3). An undulose contact exists between the debrites and the 2–4-meter-thick amalgamated turbidites which overlie them (Fig. 9). These medium sand- to pebble-grade turbidites are lenticular in geometry, can be divided into meter-scale fining-upwards successions, and contain inclined stratification (Fig. 9).

Interpretation.—The angular unconformities are interpreted to be related to salt-diapir movements, and are interpreted as part of a tapered halokinetic sequence (Giles and Rowan 2012; Poprawski et al. 2014). Unit

TABLE 4.—Table describing geometrical configurations observed in the Black Flysch Group.

Architecture Name	Description	Interpretation	Facies Association (Table 3; Fig. 6)
Tabular bedded	A package of stacked beds which show a continuous thickness laterally for 10s to 100s m, occasionally with some subtle thickness changes (Fig. 7A). Postdepositional faulting and tectonic and halokinetic tilt prevent these geometries from being traced on a 100s m-km-scale. Common in thin-bedded (Fig. 7A) and medium-bedded sandstones (Fig. 5D). Tabular geometries are observed > 500 m away from diapiric influence.	This continuous, stacked geometry suggests constant depositional energy. Tabular architectures appear to be uninfluenced by topography, and are similar to unconfined settings (Prélat et al. 2009). Low-density turbidites are less affected by topography than more cohesive flow (Al-Ja'aidi 2000; Bakke et al. 2013) and therefore can run up topography for greater distances, without becoming ponded.	Distal fringe (Fig. 6), proximal fringe (Fig. 7A), channel margin (Fig. 6).
Concave upward (erosionally based)	Curvilinear geobodies with variable thickness that are concave upward, consisting of a centroid and two margins, toward which the centroid thins, sometimes by up to 80%. (Fig. 7B). Erosionally based granular sandstones are present in the centroid of the geobody, often overlain by high-density turbidites, which become thinner-bedded towards the margins. The thickness of these geobodies is typically decimeter to meter scale, and thickness to width ratios can range between 1:10 and 1:50. The geobodies commonly erode and amalgamate with each other, and stack above the previous deposit.	Each geobody represents at least one event; the coarse-grained basal lag could represent a bypass event before the high-density turbulent flow which filled the geometry. These multipart geobodies, which are attributed to deep-water channels based on their geometries, stack on top of and erode into each other, suggesting increasing confinement (Mayall et al. 2010).	Channel axis (Figs. 6, 7B)
Pinching out upslope	Elements that change in thickness, but only in one direction (Fig. 7C). Commonly these geometries are amalgamated, with individual events displaying a convex-up geometry. Thinning rate is approximately 10cm/m in Figure 7C.	Thinning of deposits indicates flow deceleration related to topography, which ultimately lowers flow concentration (Baas et al. 2011; Teles et al. 2016). The eventual pinch-out of the sandstone is due to the inability of the flow to run up the entirety of the topography.	Proximal fringe (Figs. 6, 7C), lobe off-axis, lobe axis (Fig. 7C).
Convex up	Packages are generally continuous in thicknesses on the scale of the outcrop, with beds thinning slightly to either side (Fig. 7E). The centroid is typically decimeters to meters thick. The upper surface of each deposit is commonly undulose with an overall, often subtle, convex-upward geometry (Fig. 7E). High-density turbidites dominate these architectures and are commonly stacked or amalgamated.	The upwards curvature and slight thinning of this geometry lead to their interpretation as lobate geometries (Prélat et al. 2009; Hodgson 2009; Sypchala et al. 2017). Shifting of the centroid of the lobe axis indicates that compensational stacking is influencing these deposits similar to that observed in unconfined settings (Prélat et al. 2009; Spychala et al. 2017).	Lobe off-axis (Fig. 6), Lobe axis (Figs. 5C, 6).
Pinching out downslope	Packages are triangular in geometry and pinch out gradually. These architectures are very common at Gaztelugatxe Island (Fig. 3), where they consist of limestone breccia (Table 1) and have thinning rates of 6.7–10 cm/m downslope (Fig. 7E). Towards the top of Gaztelugatxe Island (closer to the contact with Gaztelugatxe Limestone) these architectures are amalgamated, whilst farther away from the limestone they are interspersed within tabular architectures. Successive thin-bedded, tabular deposits appear to onlap onto the topography formed by these downslope-thinning geobodies (Fig. 7E).	These deposits are interpreted as talus deposits, common around diapiric highs (Giles and Lawton 2002; Giles and Rowan 2012) and on fault scarps (Poprawski et al. 2014, 2016). The similarity in facies and geometry to "carbonate lentils" described elsewhere (McBride et al. 1974; Hunnicutt 1998; Kernen et al. 2012, 2018) and the likely close to the offshore Bakio diapir (Poprawski et al. 2016) suggest that these geometries are halokinetically driven. The source of this talus is interpreted to be the Gaztelugatxe Limestone due to its proximity and geometrical relationships. Onlap of successive deposits suggest that diapiric collapse was coeval with deep-marine deposition.	Limestone breccia (Table 1).
Undulose	Packages have an undulose, heterogeneous geometry (Fig. 7F). Individual beds vary in thickness and facies, and include thin beds, chaotic mud-rich debrites, and limestone breccias (Fig. 7F), but overall architecture maintains a broadly consistent thickness. The base of these architectures can be composed of limestone breccias (Fig. 7F, Table 1).	These remobilized units represent slump deposits. Ranging paleoflow directions, and both carbonate and siliciclastic inclusions, suggest they are derived from the diapir roof and flanks (Poprawski et al. 2014). The undulose geometries could overlie carbonate "lentils" or may reflect the reworking of "lentils" in these deposits (Fig. 7F).	Mass-failure deposits; limestone breccia (Table 1), chaotic debrites (Fig. 5J, K), remobilized proximal-distal fringe (Fig. 7F).
Tabular amalgamated beds	Packages appear tabular and consist of beds which remain relatively consistent in thickness, with minor deviations related to previous topography (Fig. 7G). This architecture is principally composed of the channel–lobe transition zone facies association (Fig. 6). Concave depressions, which are spoon-shaped and meter scale in width, can be seen on bed tops and bed bases and are associated with undulations at bed scale (Fig. 7G). Overall the geometry is slightly concave up, with the center of each deposit thinning slightly on either side at the scale of the outcrop (Fig. 7G).	The dominance of channel–lobe-transition zone facies associations leads to an interpretation of a stacked, scoured, broad channel–lobe transition zone where erosional and depositional processes were active (Vicente Bravo and Robles 1991; Robles et al. 1995; Brooks et al. 2018). Spoon-shaped depressions are representative of megaflutes and scours (Robles et al. 1995). These cause a variable depositional topography which influenced subsequent flows, resulting in slight compensational stacking.	Channel–lobe transition zone (Figs. 5A, 6)

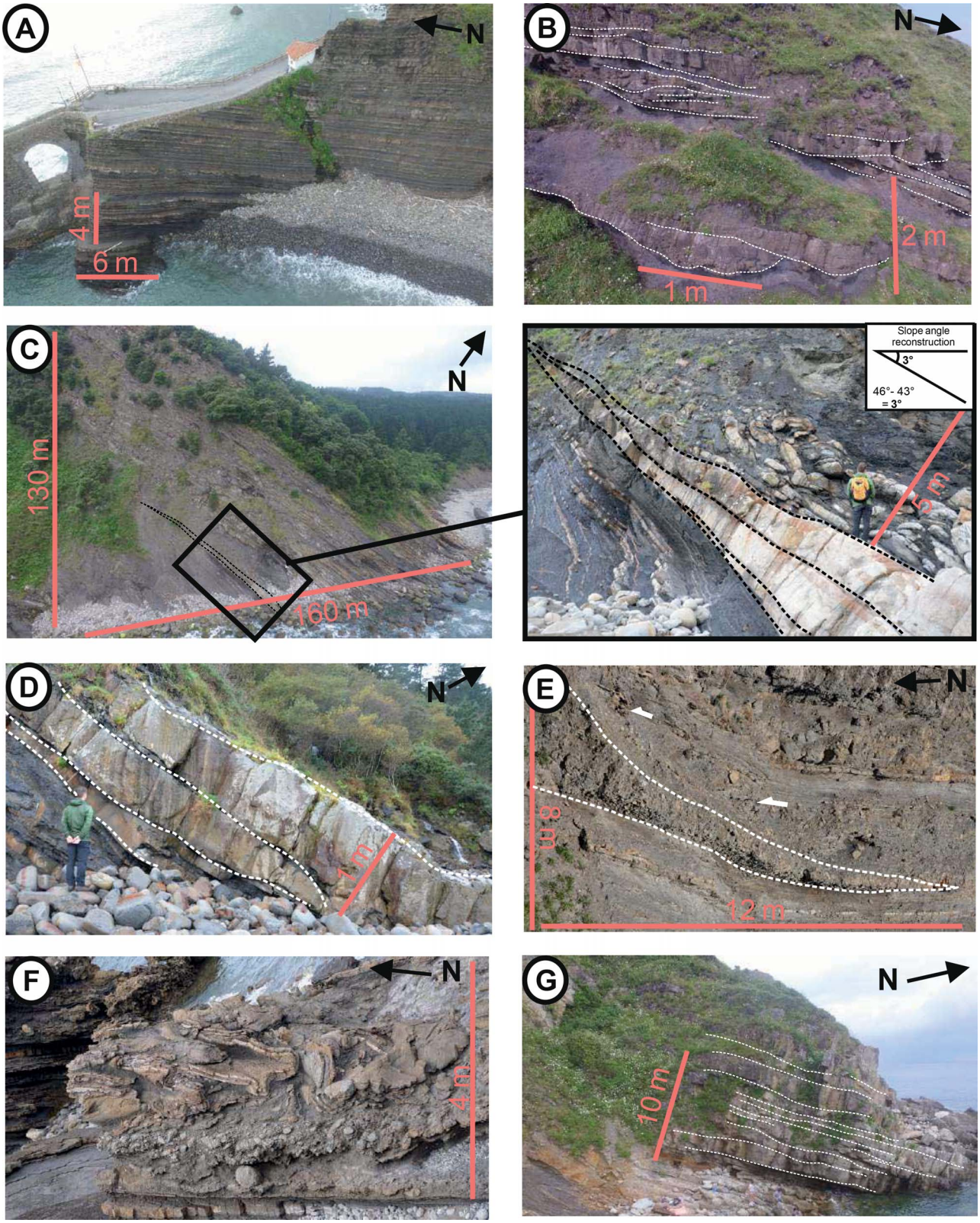

FIG. 7.—Photographs showcasing the variety of geometries observed in the study area. North is indicated. Peach highlights scale. **A)** Tabular bedded. **B)** Concave upward; white lines highlight individual architectural elements. **C)** Pinching out upslope; black lines highlight pinch-out geometry, black box locates zoom in which was used for reconstruction of the slope angle. **D)** Convex upwards; white lines highlight each element. **E)** Pinching out downslope; white lines outline triangular geometries, and white arrows indicate onlap (also in Fig. 5C). **F)** Undulose. **G)** Tabular amalgamated beds; white lines outline individual beds.

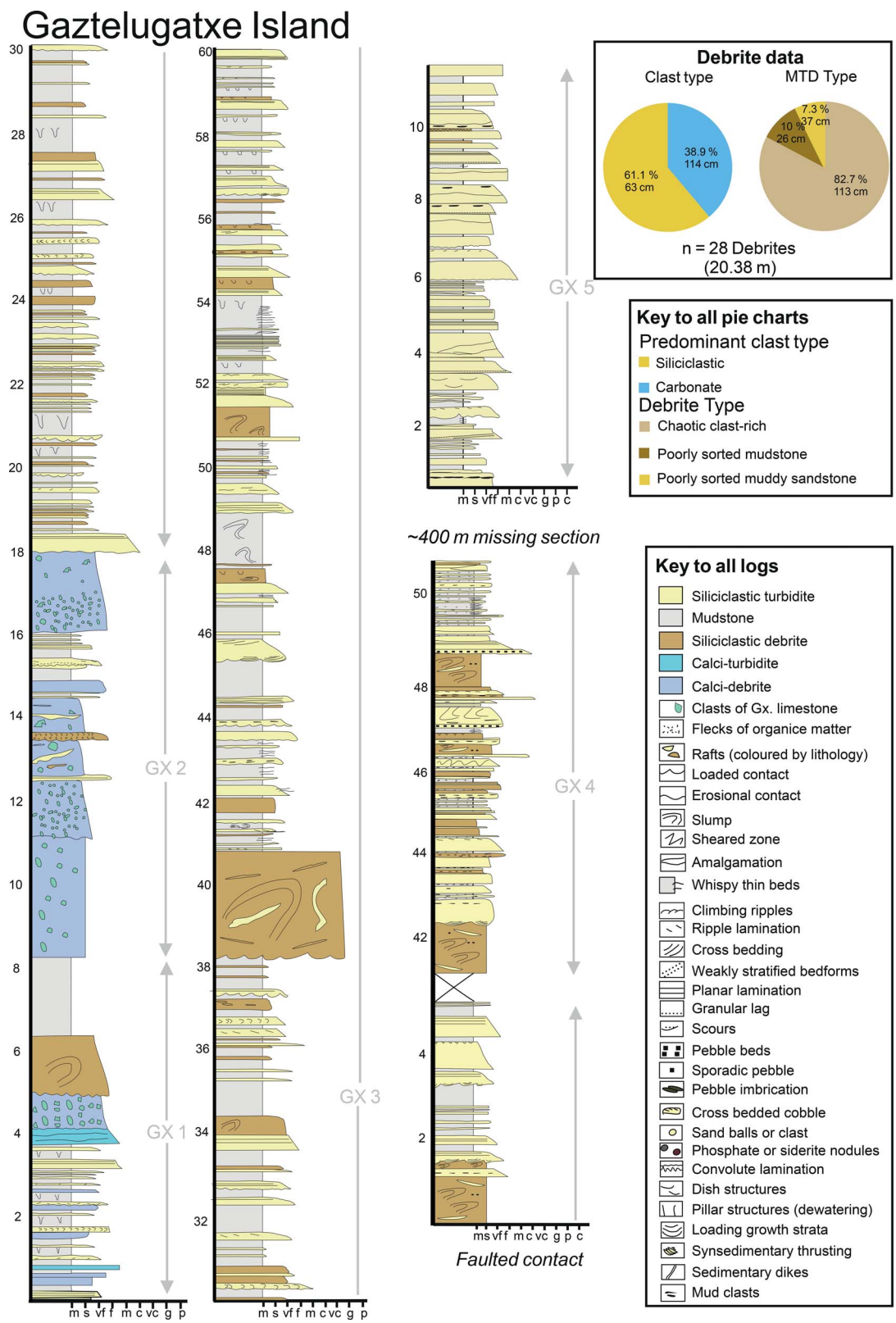

FIG. 8.—Sedimentological log through the Black Flysch Group at Gaztelugatxe Island. Location is on Figure 3. Transects of individual logs are separated by missing sections as highlighted, and are therefore not continuous. Similar sedimentary facies on either side of the fault suggest that GX3 continues on both sides of the structure, and therefore the impact of the structure is minor. Key for all the logs and pie charts shown. Thicknesses are in meters. GX# relate to stratigraphic units discussed in the text. Pie chart shows debrite data divided by predominant clast type and debrite type (Table 2), and relative proportions of all debrites at this section, and average thickness of each type is shown.

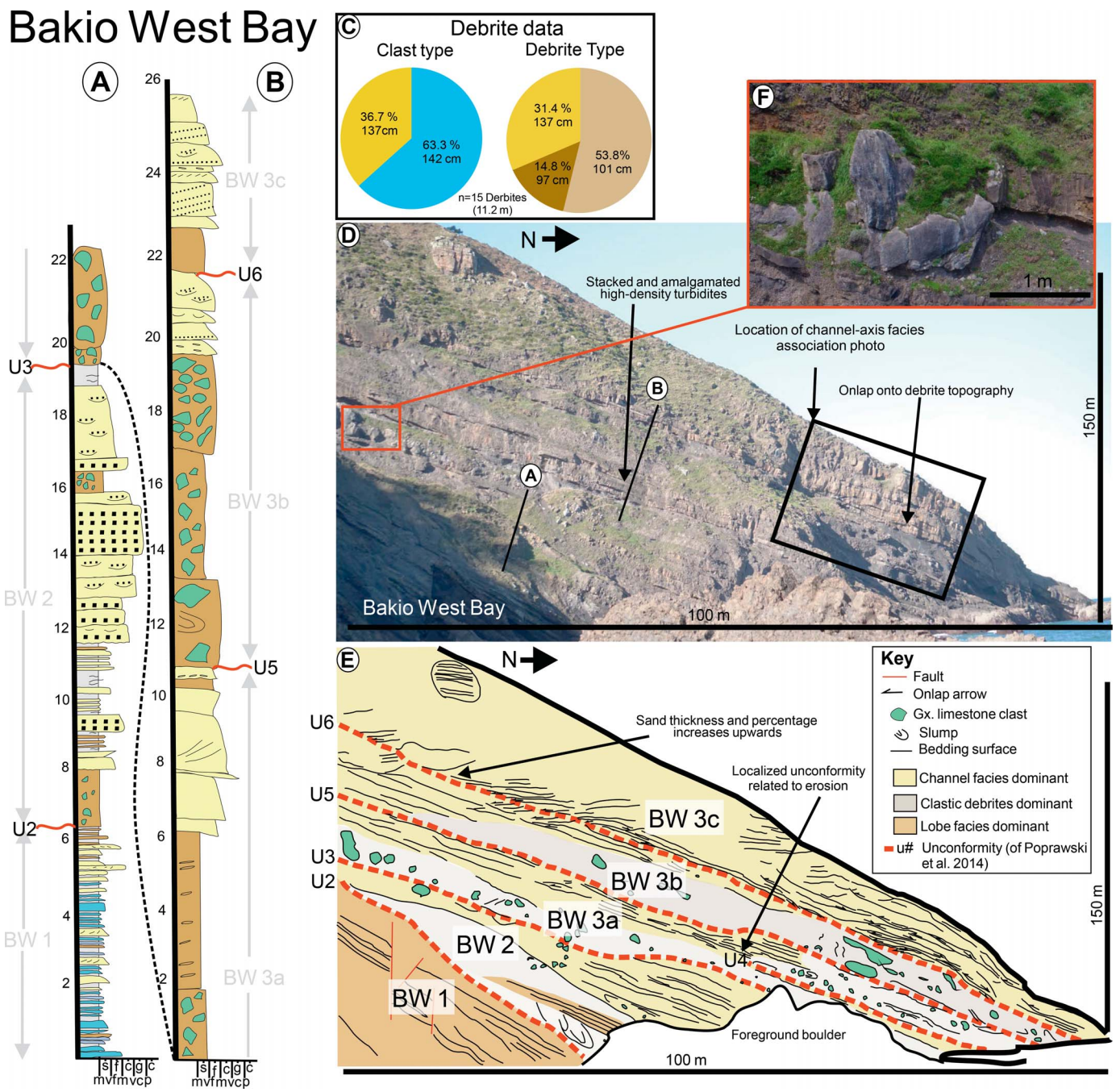

FIG. 9.—Variability of facies and architectures within large-scale depositional elements at Bakio West Bay, located in Figure 3. **A**, **B)** Stratigraphic logs, which are located in Part D and blown up for clarity. Thickness is in meters. Key is in Figure 8. BW# refers to stratigraphic unit discussed in the text. Dashed lines between logs highlight correlation. **C)** Pie chart showing debrite data divided by predominant clast type and debrite type (Table 2), and relative proportions of all debrites at this section, and average thickness of each type is shown. **D)** Uninterpreted and **E)** Interpreted large-scale architectures and facies details at Bakio West Bay. Unconformities are from Poprawski et al. (2014), and are highlighted in red where they divide packages of stratigraphy. U4 of Poprawski et al. (2014) is not laterally extensive and appears to represent an isolated, erosionally based depositional element (Fig. 9E). Based on these observations and the presence of channel-axis facies associations we suggest that U4 represents the base of a channel cut and not a halokinetic angular unconformity (*sensu* Giles and Rowan 2012). Black box in photograph locates the channel-axis facies association (Fig. 5F). **F)** Clasts of Gaztelugatxe Limestone which form out-runner blocks forming sea-floor topography.

BW1 marks the transition from BBF to BFG, and is interpreted as representing deposition at the base of slope of the carbonate platform, which was growing on the Bakio diapir (Fig. 12D: Poprawski et al. 2014). Coarse-grained sandstones with lenticular geometries, scoured bases, and normal grading, such as those observed in BW2, indicate deposition in a channelized or scoured setting (Figs. 6F, 9, 12E; e.g., Hubbard et al. 2014; Hofstra et al. 2015). The debrites capping unconformities could be halokinetically-derived or related to channel-margin collapse induced by diapir movement (Rodriguez et al. in press). The wide range of clast rock types in these debrites suggests that they are dissimilar to other

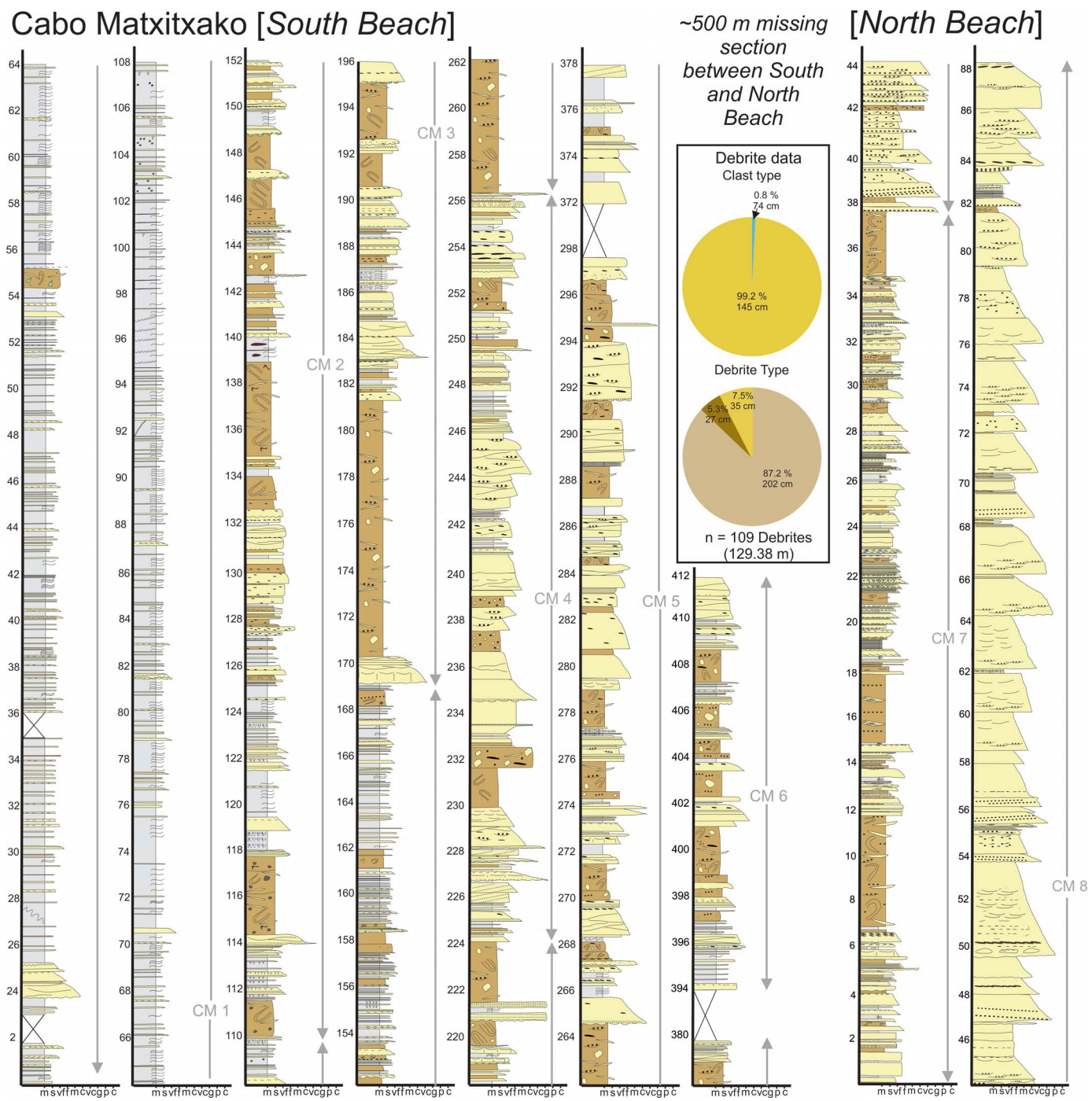

FIG. 10.—Sedimentary log through Cabo Matxitxako Beach. Location in Figure 3. Missing sections are indicated; thickness is in meters. Key for all logs is provided in Figure 8. CM# indicate stratigraphic units discussed in the text. Roughly 500 m of missing section separates South and North Cabo Matxitxako. The pie chart shows debrite data divided by predominant clast type and debrite type (Table 2), and relative proportions of all debrites at this section, and average thickness of each type is shown.

halokinetically derived debrites and could indicate a different set of mass flows sourced up-dip of the depositional system (Fig. 9C; e.g., Doughty-Jones et al. 2019; Wu et al. 2020).

The deepest point of each lenticular geometry in BW3 appears to step eastward towards the Bakio diapir (Figs. 6F, 7A); this could indicate lateral-accretion deposits from a meandering submarine channel (e.g., Peakall et al. 2007; Kane et al. 2010; Janocko et al. 2013). The concave-upward geometry of the turbidites and the undulose contact with the debrite below (Figs. 6F, 7B, 9) could represent channel fills or scour fills influenced by previous debrite topography (e.g., Cronin et al. 1998; Jackson and Johnson 2009; Kneller et al. 2016). The thick beds, concave-upward geometry, erosional bases, and coarse grain size suggests that these deposits are channel fills rather than scour fills (Hubbard et al. 2008; Romans et al. 2011; McArthur et al. 2020).

The repeated facies change between pebbly chaotic debrites and channelized turbidites is interpreted to represent periods of rapid diapir

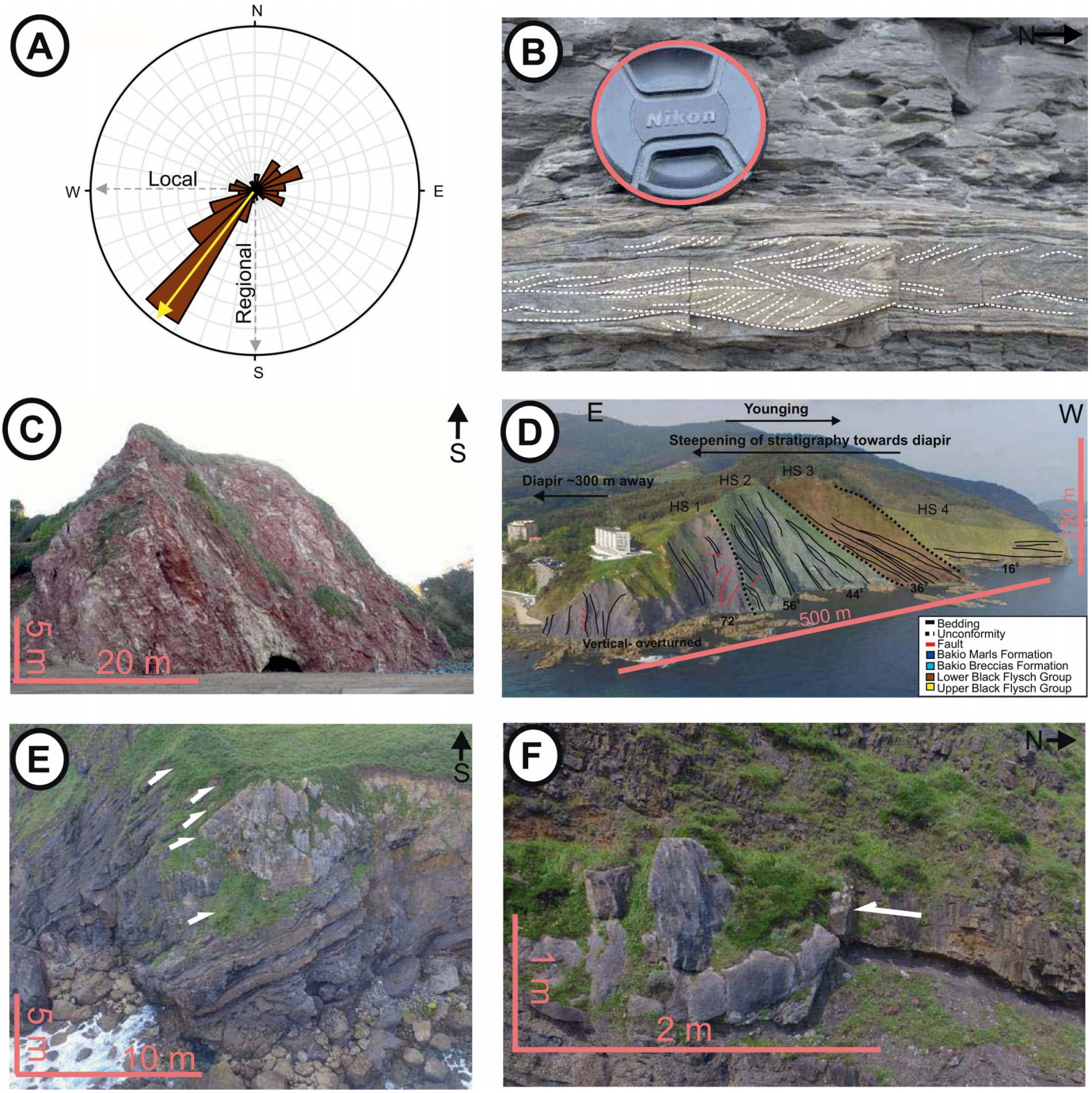

FIG. 11.—Evidence for topography and paleoflow direction. Black arrow shows orientation and peach indicates scale, and lens cap is 52 mm. **A)** Rose diagram for 284 paleocurrent indicators (ripples, sole marks, cross-stratification) from the Black Flysch Group. Readings have been corrected for tectonic tilt yellow arrow indicates dominant paleoflow direction some radial spread is due to ripple reflection. Gray arrows indicate regional (to the south) and local (to the west) paleoflow directions, discussed in the text. **B)** Evidence for opposing-direction ripples suggesting ripple reflection. **C)** Triassic-age Keuper Group outcrop of clays, carbonate, and gypsum at Bakio Beach, thought to be part of the Bakio diapir. **D)** Composite halokinetic sequence associated with the western flank of the Bakio diapir; HS, halokinetic sequence. **E)** Pinch-out and onlap of lowermost Black Flysch Group thin-bedded turbidites onto a Gaztelugatxe Limestone clast on the eastern flank of the diapir. **F)** High-density turbidite abruptly terminating against a block of Gaztelugatxe Limestone in HS3 (BW3).

growth, evidenced by debrites overlying halokinetic unconformities (Giles and Rowan 2012). This is suggested to have been followed by periods of relative diapir quiescence, which permitted submarine channels to infill debrite topography and migrate around the diapir due to reduced seafloor topography (Kane et al. 2012).

Cabo Matxitxako

Cabo Matxitxako provides an extensive section (c. 600 m) through the BFG. In this locality, we subdivide the group into eight lithostratigraphic units (CM1–8; Fig. 10). There is c. 500 m of missing section between Cabo

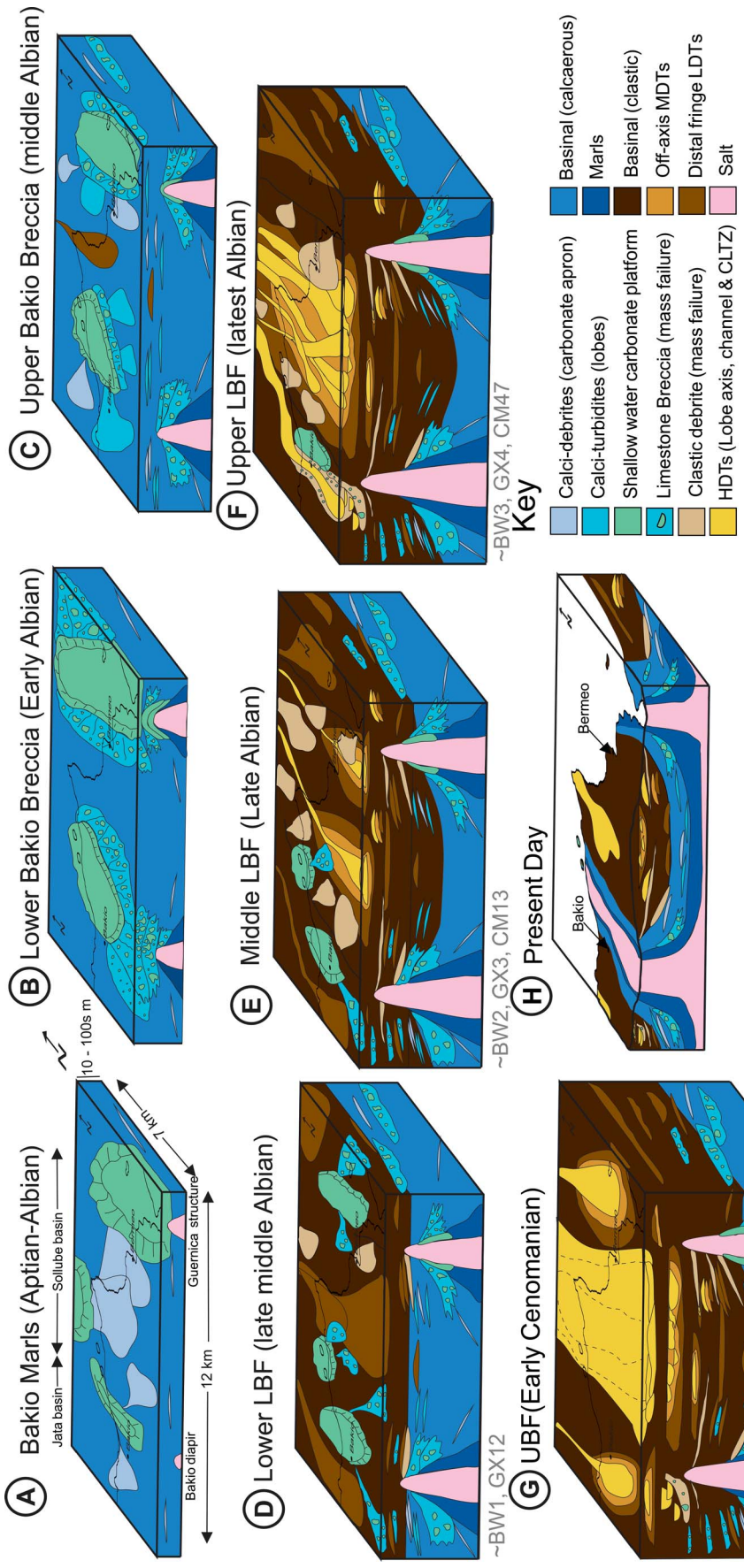

FIG. 12.—Schematic depositional models showing the geological evolution of the system through time, specifically detailing deep-water sub-environments and their interactions with salt-induced topography. Black lines on top of each model outlines present-day coastline. Bakio and Guernica structures are indicated. Geometry of the Guernica salt body is hypothetical. Extrapolations between localities are based on topography, outcrop pattern, and UAV imagery. Parts A–C are after Poprawski et al. 2014, Parts D–G are based on this study. Locations of stratigraphic units discussed in the text (e.g., GX1, CM1) are shown. **A–G)** Schematic with dimensions indicated in Part A. **H)** Present day and to scale based on Figures 3 and 5, with two times vertical exaggeration, representing post-Cretaceous inversion, uplift and erosion. LDT, low-density turbidite; MDT, medium-density turbidite; HDT, high-density turbidite; CLTZ, Channel lobe transition zone.

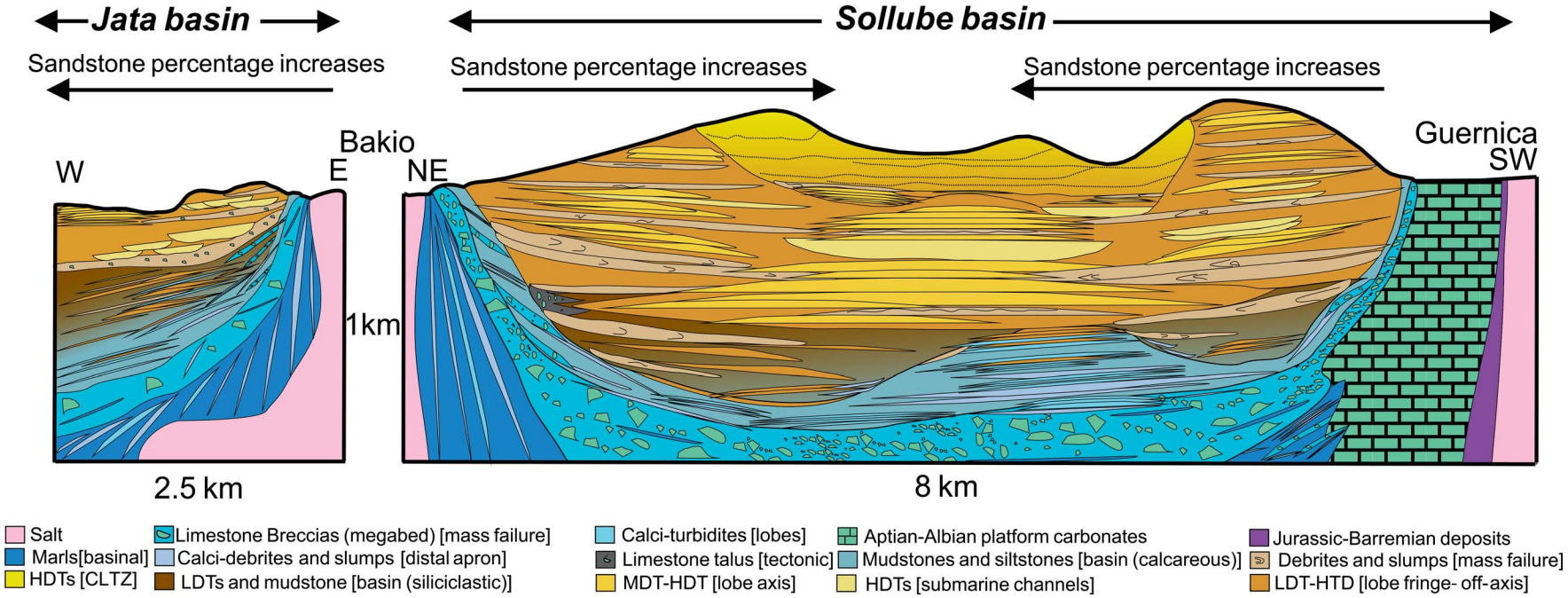

FIG. 13.—Schematic deep-water facies and architectural elements observed on both flanks of the Bakio diapir showing the sub-seismic-scale heterogeneity that can be associated with these systems and diapir flank plays. Section is two times vertically exaggerated. Sollube and Jata Basins are indicated. Note change in orientation at the Bakio diapir.

Matxitxako North and South Beach (Fig. 3). Cabo Matxitxako is located in the Sollube basin, c. 4.5 km northeast and c. 5 km northwest of the Bakio and Guernica salt structures, respectively.

Description.—CM1 is a 110-meter-thick package of mudstones, with minor thin- to medium-bedded siliciclastic turbidites and debrites. CM2 is 60 m thick and is dominated by meter-scale debrites with subordinate thin- to medium-bedded turbidites, hybrid beds, and mudstones (Fig. 10). Slump axes, where present, indicate a range of paleoflow directions (forming two clusters: 80–160° and 280–320°; Fig. 3). CM3 is 50 m thick and contains meter-thick packages of stacked medium to thick bedded, dewatered turbidites and slumps, meter to tens of meters thick containing rafts of thin-bedded turbidites. Two beds of granular sandstone (27 and 19 cm thick) with lenticular geometries are observed at the top of CM3. CM4 is 32 m thick, is distinguished from CM3 as it is debrite-poor and mostly comprises thick-bedded, amalgamated high-density turbidites that stack into 3 to 6-meter packages. CM5 is 124 m thick and consists of roughly equal proportions of 1 to 3-meters-thick amalgamated turbidites, which are normally graded on a bed scale, and meter-scale slumps and debrites, which occur every 2–10 m and contain rafts of thin-bedded turbidites. CM6 has a minimum thickness of 18 m, is observed at the northern part of South Beach, and is composed of 1 to 3 m debrites and 1 to 80 cm turbidites and mudstones (Fig. 3, 10). CM7 has a minimum thickness of 38 m, similar to CM6; however, the units are separated by c. 500 m of missing stratigraphy, much of which is assumed to have been removed due to Pyrenean deformation and recent landslides (Vicente Bravo and Robles 1995), so have been separated. CM8 is 40 m thick and consists of predominantly meter-scale, normally graded thick-bedded turbidites with erosional bases, cross-stratification, amalgamation, mud-clasts, and dewatering structures common throughout (Fig. 10).

Interpretation.—The Cabo Matxitxako succession (Fig. 10) suggests a broadly basinward-shifting (i.e., progradational) system from CM1 to CM4, followed by a slight back-step (i.e., retrogradational) or lateral shift in CM5 to CM7, and a further basinward shift in CM8 (Fig. 12).

Debrites and slumps with clasts of thin- and medium-bedded stratigraphy are present throughout CM2, 3, 5, 6, and 7 suggesting that the seafloor was periodically unstable, possibly due to relatively high rates of diapir rise and related seafloor deformation. CM1 is dominated by background suspension fallout and dilute low-density turbidites in a lobe-complex distal fringe setting (Fig. 12D). CM2 represents higher-energy, more proximal lobe conditions compared to CM1, based on facies, hybrid beds, geometry, stacking patterns, and thickness and is interpreted as proximal lobe fringe deposition (Spychala at al. 2017). The depositional sub-environment of CM3 is interpreted as an off-axis lobe complex, based on facies and bed thicknesses, with small distributive channel fills, evidenced by lenticular granular sandstones (Normark et al. 1979; Deptuck and Sylvester 2017). CM4 is dominated by stacked, amalgamated, high-density turbidites (Fig. 10) and is interpreted to represent deposition in the axis of a lobe complex (Fig. 12F; Prélat et al. 2009; Spychala et al. 2017). CM5 contains distributions of facies similar to those of CM3, so is interpreted to represent lobe-complex off-axis deposition with some distributive channel fills (Normark et al. 1979; Deptuck and Sylvester 2017). Debrite dominance in CM6 and CM7 suggests remobilization due to diapir growth throughout deposition (Fig. 12F). These deposits are interpreted to represent proximal-fringe to lobe-off-axis deposition (Spychala et al. 2017), which is highly modulated by halokinetic debrites. The coarse grain size, cross-stratification, thick beds, and lack of debrites and mudstones (Figs. 6E, 10), suggests that CM8 was deposited in either a lobe-axis or channel–lobe transition zone. This unit has previously been interpreted as a channel–lobe transition zone (Vincente Bravo and Robles 1995) and shares characteristics similar to channel–lobe transition zones reported elsewhere (e.g., Brooks et al. 2018). This unit shows little evidence for active topography, suggesting that the sedimentation rate had increased with respect to the diapir rise rate, possibly associated with uplift of the Landes Massif (Rat 1988; Martín-Chivelet et al. 2002), or welding of the salt source layer. Any remaining seafloor topography was filled by CM8 (Fig. 12G).

Stratigraphic Correlation

The BW, GX, and CM lithostratigraphic units represent different depositional systems despite their close proximity. Poor biostratigraphic calibration renders stratigraphic correlations between the areas challenging (Agirrezabala and López-Horgue 2017). Using lithostratigraphy, BW1 is correlated to GX1–2, BW2–3 are correlated to GX3–4 and CM1–7, and GX5 is correlated to CM8 (Figs. 8, 9, 10).

EVIDENCE FOR SEAFLOOR TOPOGRAPHY

There is widespread sedimentological evidence for seafloor topography during deposition of the BFG, which as we discuss below reflects the interplay between active salt growth and depositional processes controlling the available accommodation.

Ripple cross-lamination, cross-stratification, and sole marks indicate a regional southwestward paleoflow direction (Fig. 11). This direction is consistent with a northward source for the BFG, supporting the Landes Massif as a potential regional source area (Rat 1988; Robles et al. 1988; Ferrer et al. 2008; Puelles et al. 2014). At Cabo Matxiatxako, a secondary westward paleoflow orientation (Fig. 11A) is comparable to findings by Robles et al. (1988), who suggest that this reflects the passage of gravity flows that spilled across the Guernica structure into the Sollube basin. Therefore, paleocurrent data (Fig. 11A) suggest modulation of a regional (primarily south-trending) paleoflow by salt-induced topography (west-trending flows off east-facing slopes) (Fig. 12). Analogously, a west–south-westward paleoflow observed at Bakio West Bay (Fig. 3) may reflect the passage of gravity flows that spilled from the Sollube basin, across the Bakio structure into the Jata basin. This west–south-westward paleoflow could alternatively represent the westward deflection of regional paleoflow around the Bakio diapir.

Ripple lamination in opposing directions is common in individual thin-bedded turbidites (Fig. 11B). Such features have been attributed to flow reflection or deflection from seafloor topography (e.g., Kneller et al. 1991; McCaffrey and Kneller 2001; Barr et al. 2004; Hodgson and Haughton 2004). Moreover, hybrid beds seen throughout the distal fringe (Figs. 5L, M, 8, 9, 10) indicate that topography had influenced a transformation of flow from turbulent to laminar (Fig. 14; e.g., Barker et al. 2008; Soutter et al. 2019).

Turbidites that pinch out up depositional slope (Fig. 7C) reflect the thinning towards topography (e.g., Ericson et al. 1952; Gorsline and Emery 1959) as the low-density part of the turbidity current ran up the topography farther than the high-density component (e.g., Al-Ja'aidi 2000; Bakke et al. 2013). Hence, thicker sandstones are more likely to be confined to localized salt-withdrawal minibasins (Figs. 12, 13, 14), whereas thinner sandstones may drape halokinetically influenced slopes (Figs. 12, 13, 14; Straub et al. 2008; Soutter et al. 2019). Based on a bed-scale thinning rate of 10 cm/m at Cabo Matxitxako (Figs. 3, 10), we calculate the slope angle to be 2–3° (Fig. 7C). Due to the distance (c. 5 km) from the present-day Bakio diapir, it is unlikely that this slope is solely related to diapir growth, but rather caused by a combination of salt withdrawal or welding from the salt source layer at depth, and salt-structure growth, as observed in similar-sized subsurface examples (e.g., Doughty-Jones et al. 2017).

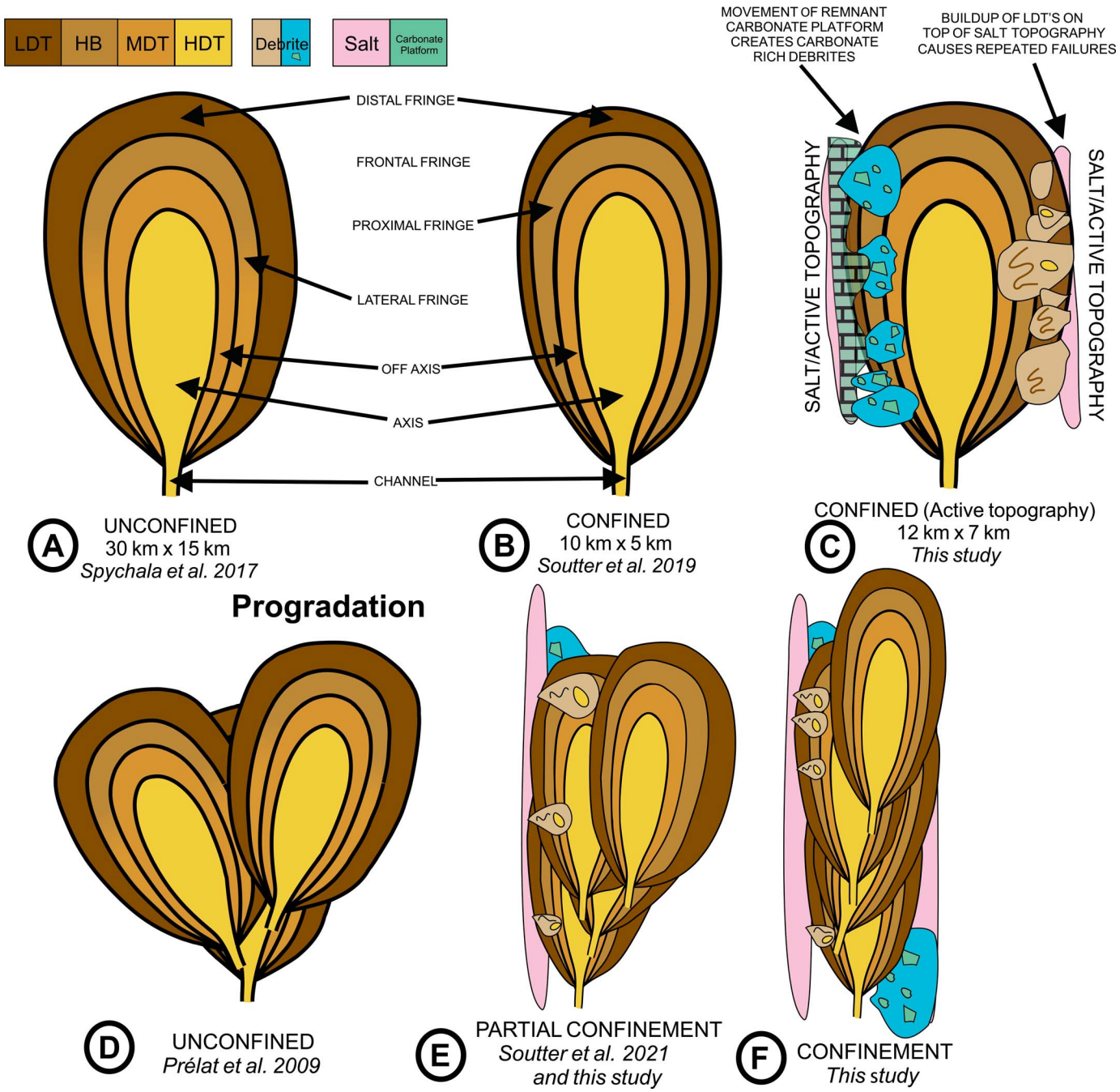

FIG. 14.—Simplified comparison between lobes in unconfined and **A–C)** confined settings and **D–F)** progradation style in these settings. Parts A and B compare the nomenclature of sub-environments of Spychala et al. (2017) and Soutter et al. (2019) from the Karoo and Annot basins, respectively. Confined systems are smaller and more elongate and have more frequent hybrid beds. Part C shows how active topography would modify the model proposed by Soutter et al. (2019). One salt body has a carbonate roof and one a siliciclastic roof purely for clarity. Part D shows compensational stacking occurring during system progradation. Part E shows how progradation may be accelerated by parallel topography, based on flume tank experiments by Soutter et al. (2021) and Bakio West Bay. Part F shows how progradation is further accelerated as gravity-flow deposits are funneled through dual-confinement. Both siliciclastic and carbonate failures are shown in Parts E and F to indicate diapiric influence on axial deposition, as the depositional system shifts away from the salt structure to avoid the debrite topography. LDT, low-density turbidite; HB, hybrid bed; MDT, medium-density turbidite; HDT, high-density turbidite.

Multiple paleoflow directions, hybrid beds, and abrupt pinch-out of beds can suggest the presence of (static) topography. However, the number of debrites intercalated with lobes, and the tapered composite halokinetic sequence observed at Bakio West Bay (Fig. 11D) suggest that this topography and salt growth was active at the time of deposition.

Debrites

Description.—Debrites, slumps, and slides (the vast majority being debrites) account for 23% of stratigraphy across all measured sections, with an average thickness of 111 cm. Assuming that all the debrites (Table 1, Figs. 5K, 7D) are derived from diapir slopes and all turbidites are

derived from far field, a 1:4 ratio of halokinetically to axially derived deposition exists. While this is clearly an oversimplification, and we provide evidence for local, diapirically derived debrites and regional, slope-derived debrites, it does suggest that locally, extra stratigraphy may be present in salt-confined basins compared to unconfined settings. Therefore interpreting stacking patterns and correlating between basins may be challenging.

Debrites on the flank of the Jata basin have an average thickness of 140 cm, compared to 119 cm and 73 cm in the axis and flank of the Sollube basin, respectively. 31% of measured stratigraphy on the flank of the Jata basin comprises debrites, compared to 22% and 18% in the flank and axis of the Sollube basin, respectively. Debrite composition shows siliciclastic dominance in the axis of the Sollube basin; debrites with carbonate clasts or matrix become more common on the flank of the Sollube basin and are dominant on the flank of the Jata basin (Figs. 8, 9, 10), in agreement with models of halokinetic sequences (Giles and Rowan 2012). Limestone clasts of similar composition in debrites on both the Jata and Sollube flanks support the presence of a carbonate platform growing on top of the Bakio diapir (García-Mondéjar and Robador 1987; Poprawski et al. 2014, 2016), indicating that these debrites are related to local diapir failures. The proportion of carbonate clasts decreases from the Sollube basin flank to axis (39% in Fig. 8 and $<$ 1% in Fig. 10) due to distance from the carbonate platform growing on top of the Bakio diapir. Isolated limestone megaclasts (Figs. 9F, 11E, F) derived from the Gaztelugatxe Limestone could be out-runner blocks (e.g., De Blasio et al. 2006; Soutter et al. 2018) or fractured blocks of platform limestone that have toppled off during diapiric growth (e.g., Alves et al. 2002, 2003; Martín-Martín et al. 2016). Younger deposits progressively onlap these limestone clasts (Fig. 11E, F), showing that subsequent turbidity currents later interacted with this additional seafloor topography (e.g., Kilhams et al. 2012, 2015; Olafiranye et al. 2013).

Interpretation.—Debrites can be sourced from either collapse on top of the diapir or its flanks, or from failures of the shelf-edge and/or slope (Doughty-Jones et al. 2019; Rodriguez et al. in press; Wu et al. 2020). However, the source is difficult to decipher without a dataset covering the coeval shelf and slope succession. The presence of more debrites in the basal active part of the Sollube basin fill (Fig. 8, 9, 10, 13) compared to the upper passive part of the basin fill (Fig. 10) suggests that mass failures are more common during initial development of salt-confined depocenters (Wu et al. 2020). The Sollube basin is more confined than the Jata basin, and therefore can be expected to receive a larger proportion of material derived from diapir growth. In fact, the Jata basin received more and thicker debrites. This could suggest asymmetric growth of the Bakio diapir, or the carbonate platform above it, creating a steeper slope on the boundary of the Jata basin. However, the apparent difference in the number and thickness of debrites could also be due to limitations of the outcrop, in that the Sollube basin flank location (Gaztelugatxe Island) is more axial than the Jata basin flank outcrop (Fig. 3). The absence of carbonate clasts in the axis of the Sollube basin, compared to the Sollube and Jata basin flanks, could suggest that diapirically derived mass failures did not extend into the axis of the basin. However, the exposed minibasin stratigraphy is younger than the flanking stratigraphy, and therefore carbonate clasts are expected to be rarer due to a decrease in exposure and availability to be remobilized through time.

The presence of complicated variations in thickness, clast type, and debrite style across the study area suggests that mass flows are likely to be both locally derived (from the salt structures) and regionally derived (from the shelf), and therefore debrites were likely both allogenic and halokinetic in origin (Moscardelli and Wood 2008; Doughty-Jones et al. 2019; Wu et al. 2020). The proximity to salt structures, reduction in mass- failure deposits away from salt structures, and the remobilized intrabasinal clasts within them suggests that the majority of debrites in the study area are locally derived from the Bakio diapirs. The wide variety of clasts types in Jata basin debrites (Table 3: Fig. 9) and the association of these deposits with channelized turbidites above could suggest that some of the Jata basin debrites were regionally derived, and deposited as part of channel-axis depositional elements. The absence of these possible regionally derived debrites in the Sollube basin could be due to confinement by the offshore part of the Bakio diapir, or different up-dip sediment routing. The difference in thicknesses and numbers of debrites between the Jata and Sollube basins suggests that they developed, at least partially, as separate depocenters influenced by different controls (Figs. 8, 9, 10).

DISCUSSION

The discussion initially focuses on the Sollube basin, then compares the Sollube and Jata basins, before comparing our observations to similar depocenters developed in other salt-influenced basins.

Architecture of the Sollube Basin

The Sollube basin is of a similar size and geometry to previously reported subsurface minibasins (Fig. 13; e.g., Pratson and Ryan 1994; Booth et al. 2003; Madof et al. 2009; Doughty-Jones et al. 2017). Therefore, this rare, exhumed example of a halokinetically influenced deep-water succession provides an excellent exposure of fine-scale minibasin depositional architecture, providing an analogue for subsurface minibasins.

Distribution of Facies and Architecture

The Sollube basin is 8 km wide and confined to the east and west by the Guernica and Bakio structures, respectively (Fig. 4; Robles et al. 1998; Poprawski and Basile 2018). Repeated stratigraphy and facies distribution on either side of Cabo Matxitxako, the change in bedding angle between the LBF and UBF, and sedimentological evidence for syndepositional topography support the presence of a broadly symmetrical basin confined by the Bakio and Guernica structures.

Early stratigraphy in the siliciclastic fill of the Sollube basin is dominated by thin-bedded sandstones, with localized debrites on the flanks (Figs. 8, 10, 13). As the basin developed, thicker-bedded sandstones representing channel fills and lobes were deposited in topographic lows (basin axis), consistent with subsurface analogues (e.g., Booth et al. 2003; Madof et al. 2009; Mayall et al. 2010; Doughty-Jones et al. 2017) and numerical models (e.g., Sylvester et al. 2015; Wang et al. 2017). Towards the flanks, the lower-density parts of the flows responsible for the thick-bedded sandstones may run up topography, depositing thin-bedded sandstones. Therefore, allocyclically controlled, axially derived, and often the thickest stratigraphy is observed in the axis of the minibasin. Halokinetically controlled (e.g., debrites) or -influenced (e.g., thickness variations) stratigraphy occurs towards the basin margins. These interpretations are consistent with subsurface studies (e.g., Doughty-Jones et al. 2017; Rodriguez et al. in press; Wu et al. 2020).

Oluboyo et al. (2014) suggest that a fundamental control on the type of confinement developed is the incidence angle between the strike of the salt structure and the paleoflow direction. "Fill-and-spill" architecture is observed in deep-water environments where topographic highs strike perpendicular to the gravity-flow direction (i.e., at a high incidence angle) (e.g., Piper and Normark 1983; Hay 2012; Prather et al. 2012; Soutter et al. 2019). This study documents a rare example of an exhumed halokinetically influenced deep-water succession where paleoflow is at a low incidence angle to structural strike (i.e., oblique-parallel). In such scenarios, spill between basins is rare, and sedimentary systems are deflected to run broadly parallel to salt walls in minibasins for several kilometers (Figs. 13, 14, 15; e.g., Oluboyo et al. 2014). The four-fold model of the fill of a

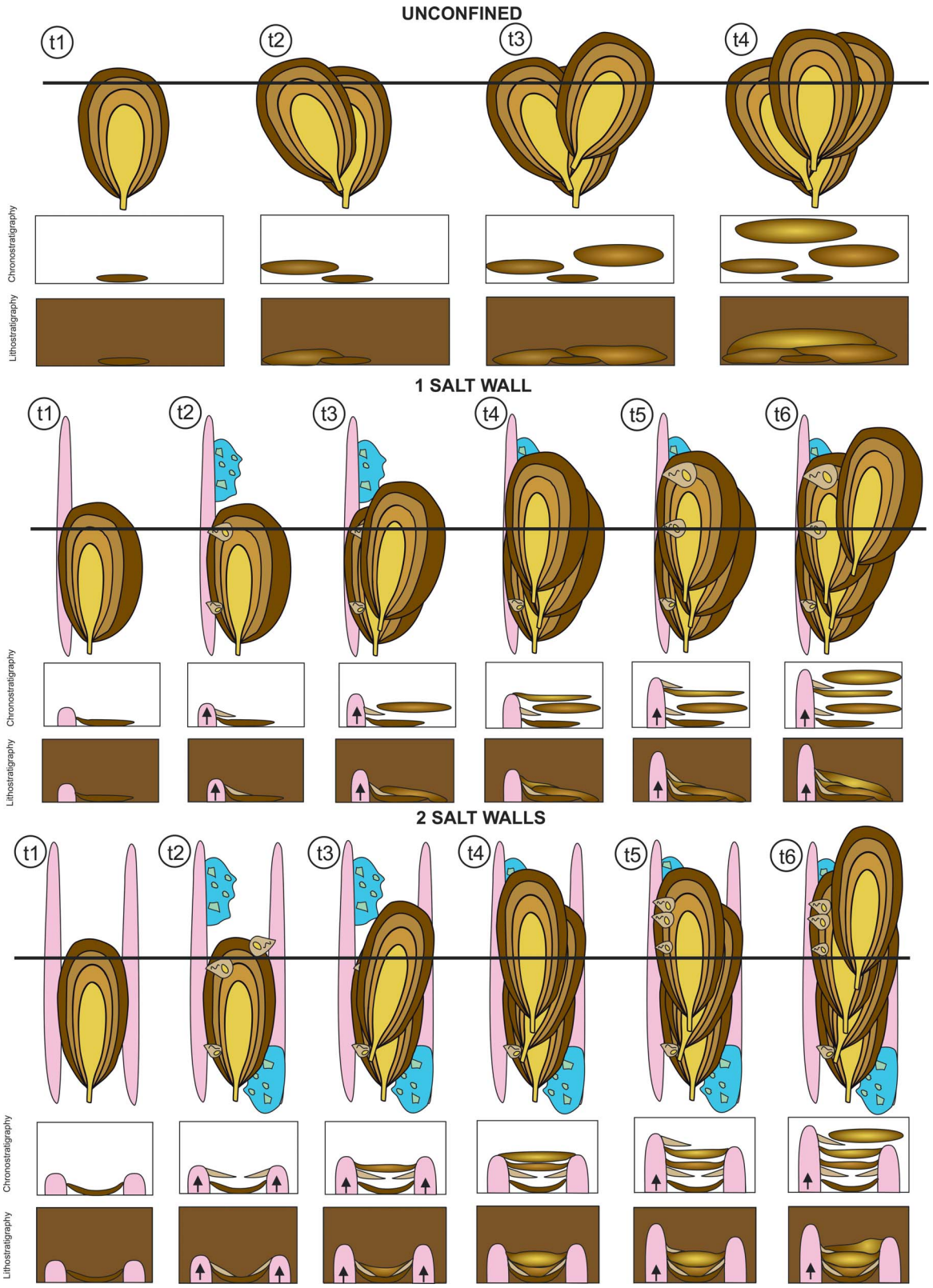

FIG. 15.—Thought experiment comparing the effects of variable topography in the evolution of deep-water systems. Unconfined settings, partially confined systems, and confined systems are compared. Unconfined settings are based on Prélat et al. (2009) and Sphycala et al. (2017). One salt wall is based on the Jata basin and flume-tank experiments (Soutter et al. 2021). Two salt walls are based on Sollube basin. Upper image indicates schematic map section. Black line shows line of section shown in chronostratigraphy and lithostratigraphy, and represents a fixed point for comparing extent of progradation across the models. Chronostratigraphy shows deposition during time steps (t1–6). Lithostratigraphy shows how deposits relate to topography and previous deposits. Key is the same as Figure 14. Arrows on salt structures indicate periods of salt rise; lack of arrows suggests relative quiescence. No scale is implied.

confined basin (Sinclair and Tomasso 2002) is not appropriate where paleoflow is oblique or parallel to salt structures, and there is a down-dip exit (i.e., not confined in all directions). Our study indicates that the dominant style of interaction between gravity flows and topography is lateral confinement, with channels and lobes in the Sollube basin being thickest in the axis and elongated parallel to the margins of the salt-controlled basin. The presence of MTDs is somewhat overlooked in both the confinement model proposed by Oluboyo et al. (2014), and the earlier "fill-and-spill" model (Winker 1996; Prather et al. 1998; Sinclair and Tomasso 2002). MTDs sourced from either up-dip (i.e., extrabasinal; detached) or from local mass failures (i.e., intrabasinal; attached) related to growing salt structures, can generate additional syndepositional relief and flow confinement (Fig. 14; Moscardelli and Wood 2008; Rodriguez et al. in press).

The hierarchical scheme for classifying deep-water systems developed in the Karoo basin (Prélat et al. 2009) is widely accepted, but must be used with caution, or be adapted for confined systems (Prélat et al. 2010; Etienne et al. 2012; Marini et al. 2015). Prélat et al. (2010) recognized that width-to-thickness ratios and areal extent-to-thickness ratios are different for confined and unconfined systems, with width-to-thickness ratios of 100:1 measured in selected subsurface confined settings, compared to 1000:1 in unconfined settings, and areal extent-to-maximum-thickness ratios 30 times greater in unconfined systems compared to confined systems (Prélat et al. 2010). All examples used in Prélat et al. (2010) are from settings where paleoflow is perpendicular (high angle) to topographic strike.

In terms of areal extent, stratigraphy in the Sollube basin (c. 8 km wide) would be best classified as a lobe element (c. 5 km wide) using the Prélat et al. (2009) framework. However, in terms of thickness each lithostratigraphic unit observed at Cabo Matxitxako (18–124 m thick, Fig. 10) would be classified as a lobe complex (c. 50 m thick). The width:thickness ratio of lobes in the Sollube basin is c. 160:1 (taking a midpoint thickness of 53 m), in agreement with confined examples reported by Prélat et al. (2010). This suggests similar basic geometries for confined lobes regardless of incidence angle between paleoflow and topographic strike. The dimensions observed in the salt-influenced minibasins in the study area are comparable to those of intraslope lobes complexes documented in the Karoo (6–10 km wide, 10–15 m thick; Spychala et al. 2015), which are an order of magnitude smaller than their basin-floor counterparts (Prélat et al. 2009).

Confined-lobe complexes are predicted to have smaller areal extents because radial spreading is minimal due to topographic confinement (e.g., Marini et al. 2015; Soutter et al. 2019). The ratio of axis to fringe deposition is likely to be increased in confined settings where flows stay turbulent for longer, flow deceleration is limited, and development of a wide fringe is hindered due to presence of topography (Etienne et al. 2012; Soutter et al. 2019). The presence of thicker axial deposits due to confinement by topography, and less space for lateral lobe switching to occur, may make axis definition easier in a confined setting; however, this may change through time if topography is healed and depositional systems become less confined (Marini et al. 2015).

This study supports recent work (Oluboyo et al. 2014; Rodriguez et al. in press) which suggests that elongate systems are common adjacent to topography, on all scales. This is in contrast with the roughly equant geometries predicted in unconfined systems (Prélat et al. 2009). Multi-scale analysis suggests that all confined hierarchical elements would have greater lengths than widths, and lesser areal extents and greater thicknesses (lower aspect ratios) than unconfined settings when deposited adjacent to oblique-parallel topography (Booth et al. 2003; Oluboyo et al. 2014; Rodriguez et al. in press).

Development of Axial Systems

The overall upward thickening of beds and coarsening of grain size from south to north at Cabo Matxitxako is associated with a transition in depositional environment from lobe distal fringe to channel–lobe transition zone (Figs. 10, 12). Coarsening and thickening upwards elsewhere is widely interpreted to represent progradation (e.g., Mutti 1974; Macdonald et al. 2011; Kane and Pontén 2012); however, this could also represent (a component of) lateral stacking of lobes (e.g., Prélat and Hodgson 2013).

Throughout the Pyrenean, the BFG is interpreted to have been controlled by allocyclic progradation (Robles et al. 1988; Agirrezabala and Bodego 2005), driven by increases in sediment supply following the uplift of the Landes Massif (García-Mondéjar et al. 1996; Martín-Chivelet et al. 2002; Puelles et al. 2014) and/or increased flow efficiency from confinement (Hodgson et al. 2016). This regional progradation, along with our field observations, provides compelling evidence that, on a lobe to lobe-complex scale, the stratigraphic architecture of the study area is controlled primarily by system progradation. Lateral switching may be reduced due to confining topography decreasing the amount of space available for switching to take place (e.g., Mayall et al. 2010; Oluboyo et al. 2014).

By definition, only two lobe elements would be able to fit laterally within the Sollube basin during LBF deposition (Prélat et al. 2009), suggesting that due to confinement lateral stacking in our study area is feasible only at the bed scale (Marini et al. 2015). The apparent retrogradation observed between CM5–7 could be a result of bed to lobe-scale lateral shifting and compensational stacking modulating an otherwise progradational lobe complex (e.g., Gervais et al. 2006; Pickering and Bayliss 2009; Etienne et al. 2012; Morris et al. 2014).

The lack of space for lateral stacking to occur suggests that lateral topography reduces flow loss to overspill and deceleration, and therefore the system remains turbulent for longer. This causes a basinward shift in deposition effectively acting to magnify the effects of progradation (e.g., Kneller and McCaffrey 1999; Talling et al. 2012; Patacci et al. 2014). This concept accounts for numerous, thick, high-density turbidites (UBF) along the axis of the Sollube basin formed by gravity flows that were funneled between the two structures (Figs. 13, 14C, F, 15; e.g., Scott et al. 2010; Oluboyo et al. 2014; Counts and Amos 2016; Howlett et al., in press).

Using observations from Bakio, a range of stacking patterns may form during progradation of a deep-water system in an unconfined, partially confined, and dual-confined setting (Fig. 15). Unconfined fans have a higher aspect ratio, surface area, and avulsion angle than confined systems as the ability of the flows to spread radially was not restricted by topography (Prélat et al. 2009; Spychala et al. 2017). Where only one lateral confinement is present, deposits may be asymmetrical, as flows are confined by diapir topography in one direction but are able to spread radially away from it, as is seen in the deposits of the Jata basin (Fig. 9; Soutter et al. 2021).

In settings with lateral confinement, deep-water systems are elongated axially, subparallel with bounding relief (Figs. 13, 14, 15; Oluboyo et al. 2014; Soutter et al. 2021). Funneling of axial gravity flows, and therefore bed amalgamation, is interpreted to be more enhanced where two salt structures are present, resulting in thicker deposits but areally smaller depositional architectures than unconfined settings (Kneller and McCaffrey 1999; Patacci et al. 2014; Soutter et al. 2021).

Diapir growth is not continuous through time, and phases of rapid growth (e.g., Fig. 5; t2–t3, t5–t6) and quiescence (e.g., Fig. 15; t1, t4) cause destabilization and remobilization of the diapir roof, overburden or flank deposits (Figs. 8, 9, 10). This can drive rerouting of subsequent systems to avoid failure topography, potentially resulting in lateral or compensational stacking (Figs. 9, 12F, 14E, 15; Kane et al. 2012; Doughty-Jones et al. 2017, 2019; Rodriguez et al. 2018, in press). In fully confined settings, there is no space for rerouting and lateral MTDs could be amalgamated with, or eroded away by, flows depositing axial turbidity currents (Figs. 7C, 10, 12, 13, 14, 15).

Active or Passive Topography

The geometry and number of the debrites, and thin-bedded sandstones that pinch-out, is controlled by the presence of actively growing topography during LBF deposition. The absence of debrites in the UBF suggest that diapir growth ceased following uplift of the Landes Massif (García-Mondéjar et al. 1996; Puelles et al. 2014).

We infer that, following the cessation of diapir growth, an underfilled synclinal basin remained due to remnant topography of the buried Bakio and Guernica structures, which appears to have constrained UBF deposition until it was filled (Figs. 3, 12G, 13). The LBF represents early-stage "active" deposition, perhaps comparable to synkinematic megasequences observed in the subsurface, whereas the UBF represents late-stage "passive" deposition, infilling antecedent topography, comparable to postkinematic megasequences observed in the subsurface (e.g., Pratson and Ryan 1994; Warren 1999, 2006; Jackson and Hudec 2017). UBF deposits are less confined due to the lesser influence of salt-influenced topography during deposition, and therefore through time may evolve to represent semiconfined or unconfined deep-water systems, more capable of lateral stacking (Marini et al. 2015).

Comparison of Sollube and Jata Basins

Different facies distributions on either side of the Bakio diapir varied during BFG times according to the degree of confinement and distance from diapir crest (Figs. 12, 13). In the BBF, clast- and matrix-supported breccias are common in the Sollube and Jata basins, respectively (Poprawski et al. 2016), suggesting that minibasin individualization is long-lived. The lack of confining topography to the west of the Jata basin may have caused flows to dilute, resulting in muddier, more-matrix-rich breccias (e.g., Hampton 1972; Sohn et al. 2002; Baas et al. 2009).

LBF stratigraphy in the Jata basin thins towards the Bakio diapir (Fig. 11D), showing more evidence for topography than comparable strata in the Sollube basin, supporting the idea that halokinetic deformation is greatest closest to salt structures (Giles and Lawton 2002; Giles and Rowan 2012). Richness in limestone clasts in LBF MTDs in the Jata basin (Fig. 9C, Table 3) could indicate asymmetric buildup and failure of the carbonate platform above the Bakio diapir, preferentially filling the Jata basin (Rosales and Pérez-García 2010; Li et al. 2016). Asymmetric growth and failure of either the carbonate platform or the diapir itself is further supported by thicker, more prevalent debrites observed in the Jata basin compared to the Sollube basin (discussed above: Figs. 8, 9, 10). The diverse range of clast types in the Jata basin (Table 3; Fig. 9) could suggest different depositional routing relative to the Sollube basin, possibly due to the presence of salt topography causing different source areas to be tapped (e.g., Mayall et al. 2010; Oluboyo et al. 2014).

Another key difference is the architecture of thick-bedded sandstones. In the Jata basin, individual depositional elements are often erosionally based, concave-upwards, and thinner, and show more tractional structures (e.g., ripple lamination and planar lamination) than those in the Sollube basin. Where lateral confinement occurs along one margin, sandstones could represent sinuous low-relief channel fills that ran subparallel to topography (e.g., Mayall et al. 2010; Oluboyo et al. 2014). These channels were able to spread laterally and migrate because they were only partially confined (e.g., Mayall et al. 2010; Oluboyo et al. 2014). Such systems are less modulated by halokinetic controls than those that develop under dual-lateral confinement (e.g., Oluboyo et al. 2014; Rodriguez et al., in press). Subsurface observations indicate that channels migrate away from growing structures (Mayall et al. 2010; Kane et al. 2012); however, those at Bakio West Bay appear to step towards the diapir in 2D (Figs. 6F, 7B). This could suggest a periodic reduction in diapir growth, due to the episodic nature of halokinesis (Kane et al. 2012), which may be unresolvable in subsurface data. Alternatively, the debrites underlying the thick-bedded sandstones could form pathways that controlled sandstone deposition, and therefore the apparent movement towards the diapir was in fact controlled by the deep-water systems infilling debrite-related paleotopography (Armitage et al. 2009). However, deciphering detailed interpretations of 3D sinuous channels from 2D exposure remains challenging (Li et al. 2016).

The Jata and Sollube basins had unique tectonostratigraphic histories throughout the deposition of the BBF and LBF due to the interplay of halokinetic, allocyclic, and autocyclic controls. Inaccessible UBF stratigraphy to the west of Bakio (Fig. 11D), from UAV photographs, appears to exhibit facies and geometries similar to UBF stratigraphy at northern Cabo Matxitxako (Fig. 10: Vincente Bravo and Robles 1991a, 1991b, 1995) suggesting that influence of halokinesis decreased through time. This supports the idea that sediment accumulation rate ultimately outpaced diapir growth rate, possibly due to the increase in sediment supply associated with the uplift and erosion of the Landes Massif (Martín-Chivelet et al. 2002; Puelles et al. 2014). Partial or complete welding of salt bodies could also be, at least partially, responsible for the reduction of influence of halokinesis through time (Jackson and Hudec 2017).

Comparison to Other Depositional Settings

Here, for ease of comparison with subsurface examples, we use mass-transport deposit (MTD), instead of debrite, to describe deposits from varied subaqueous mass flows, including a mixture of slides, slumps, and debris flows in agreement with previous subsurface studies (e.g., Nardin et al. 1979; Posamentier and Kola 2003; Pickering and Hiscott 2015; Doughty-Jones et al. 2019; Wu et al. 2020).

Recognition of Halokinetically Influenced Stratigraphy in the Field

Before this study, most understanding of halokinetically-influenced deep-water systems came from subsurface datasets (e.g., Booth et al. 2003; Madof et al. 2009; Carruthers et al. 2013; Doughty-Jones et al. 2017). Features that are common across several depositional settings where halokinetic movements are observed include multi-scalar thinning and onlap, growth faulting, pebble conglomerates, mixed siliciclastic–carbonate lithologies, MTDs, variable paleocurrents, angular unconformities, and abrupt facies variability (Dalgarno and Johnson 1968; Dyson 1999; Kernen et al. 2012, 2018; Carruthers et al. 2013; Counts and Amos 2016; Counts et al. 2019).

Deposition of thick-bedded sandstones along the axis of the Sollube basin, and thinner beds and mudstones on the flanks of the Sollube and Jata basins, is comparable to fluvial facies distribution (Banham and Mountney 2013a, 2013b, 2014; Ribes et al. 2015) where channel-fill sandstones dominate axial settings and floodplain mudstones are observed closer to the diapir.

Individual beds in the BBF are comparable in size (tens- to hundreds-of-meters packages) and composition to stacked MTDs reported overlying bounding unconformities in halokinetic sequences in the La Popa Basin (10–120 m in thickness) associated with remobilization of diapir roof or cap rock (Giles and Lawton 2002; Poprawski et al. 2014, 2016). Smaller carbonate breccias with wedge-shaped geometries (meter-scale packages; Fig. 7E) are similar in geometry and composition to "lentils" (1 meter to 100s of meters thick) described by McBride et al. (1974), but differ in thickness and areal extent. Lentils, MTDs, and breccias represent talus-like failure from diapir roof stratigraphy (Giles and Lawton 2002; Poprawski et al. 2014, 2016).

Presence of evaporite clasts in fluvial successions (Banham and Mountney 2013b; Ribes et al. 2015), suggest that the nearby diapir was exposed during deposition. Such clasts are not observed in our study area, suggesting that the Bakio and Guernica structures may have only episodically been exposed at the seabed, if at all. This fits the interpretation of carbonate-platform growth above the structures, preventing salt

exposure (García-Mondéjar 1990; Rosales and Pérez-García 2010; Poprawski et al. 2014, 2016).

The consistency of our observations and previously described halokinetically influenced settings suggests that the criteria for recognizing halokinetically influenced systems is similar regardless of depositional environment, suggesting that halokinetic controls are dominant over allocyclic ones. Multiple directions of ripple lamination, presence of hybrid beds, range of MTD types, and abrupt juxtaposition of deep-water depositional facies can be used to identify halokinetically influenced deep-water systems in core and outcrop.

Comparison between Quickly and Slowly Deforming Basins

The gravity flows responsible for the Eocene to Oligocene Annot Sandstone, SE France, were confined during deposition by Alpine fold-and-thrust belt topography (Apps 1987; Sinclair 1994). When compared with the rate of topographic deformation associated with diapir growth, the rate of orogenic deformation is more minor.

Like the BFG, the stratigraphy of the Grès d'Annot is broadly progradational, and rapid facies changes occur over tens of meters towards pinch-outs (Soutter et al. 2019). Unlike Bakio, where paleoflow was consistently at a low angle to structural trend, sub-basins in the Annot area were eventually filled and bypassed sediment into down-dip basins (Sinclair and Tomasso 2002; Salles et al. 2014), indicating that paleoflow was perpendicular to at least one of the complex structural trends (Oluboyo et al. 2014).

Debrites in the Grès d'Annot were slope-derived and infrequent compared with our study area, which were sourced laterally from failures of stratigraphy above salt structures that are intercalated with axially derived deep-water deposits (Figs. 12, 13, 14, 15). This is a reflection of a more active slope in diapiric settings.

The stratigraphy in this study is characterized by an axial deep-water depositional system and a series of lateral systems dominated by debrites fed from the growing salt structures. This interplay of two distinct depositional systems is common in deep-water environments influenced by active rift topography, such as the Gulf of Corinth, Greece (Leeder and Gawthorpe 1987; Pechlivanidou et al. 2018; Cullen et al. 2019) and the Gulf of Suez, Egypt (Sharp et al. 2002; Jackson et al. 2002, 2005; Leppard and Gawthorpe 2006). Here the continually evolving footwall scarps feed lateral MTD-rich systems coevally with axial, allocyclically controlled depositional systems. Deposits in synrift settings are often narrow and elongated parallel to the strike of normal-fault segments (Carr et al. 2003; Jackson et al. 2005; Cullen et al. 2019), indicating the control on stratigraphic architecture by footwall physiography. Analogous variability of depositional facies occurs due to salt-structure evolution in halokinetically influenced settings.

CONCLUSIONS

This study documents deep-water facies distributions, with variable amounts of topographic confinement, adjacent to growing salt structures from a rare exposed example. We compare observations from two minibasins, one confined (Sollube) and one partially confined (Jata), which are comparable in size and facies heterogeneity to subsurface minibasins in salt provinces globally.

Stratigraphic variability and juxtaposition of architectural elements in the Jata and Sollube basins is high and controlled by the interplay of halokinetic, autocyclic, and allocyclic processes. The low angle between the paleoflow and the strike direction of salt structures results in the depositional system being focused between two salt structures in the Sollube basin, and against one salt structure in the Jata basin, but with no evidence of downdip flow confinement. Confinement against topography increases the effects of allocyclic progradation. Failure of carbonate platforms developed above the crests of the active Bakio diapir and Guernica structure created lateral debrites in the flanking basins, and generated local topography to further constrain axial depositional systems. Debrites can also be sourced axially from up-dip failures on the shelf, and the compositional differences of debrites suggests that the Jata and Sollube basins were subject to different influences.

Indicators of active topography include hybrid beds, remobilized strata, lateral thickness changes over short distances, reversal in ripple cross-lamination in beds and intercalation of debrites throughout the stratigraphy. These indicators individually are not diagnostic of salt-influenced topography, but collectively they provide a set of features that support interpretation of halokinetic modulation of a deep-water setting. Following the cessation of diapir growth, topography does not heal instantly, and the "passive" paleotopography continues to confine subsequent depositional systems despite diapir inactivity.

Closely related depositional systems can be highly variable depending on their complete or partial confinement. Stacked, amalgamated sandstones are observed between the confining barriers in the Sollube basin, whereas more variable architectures are observed in the Jata basin, where only partial confinement is present. These observations are due to the modulation of a broadly progradational system by halokinetically influenced lateral barriers and the coeval development of axial allocyclic and lateral debrite-rich depositional systems.

Utilizing outcrop analogues combined with a good regional understanding of source area and salt movement and extracting insights from depositional analogues are advised when exploring in the salt–sediment interface for carbon storage or geothermal or hydrocarbon reservoir targets.

SUPPLEMENTAL MATERIAL

Supplemental Figure 1 us available from SEPM's Data Archive: https://www.sepm.org/supplemental-materials.

ACKNOWLEDGMENTS

This paper contains work conducted during ZCs' Ph.D. study undertaken as part of the Natural Environment Research Council (NERC) Centre for Doctoral Training (CDT) in Oil & Gas (grant number NEM00578X/1). ZC is a recipient of an American Association of Petroleum Geologists (AAPG) Foundation Grant-in-Aid "Gustavus E. Archie Memorial Grant" which supported this fieldwork. Stereonet 10 is acknowledged for data plotting. Dave Lee is acknowledged for building digital outcrop models. Ross Grant is thanked for his comments, figure beautifying, and proofreading. Gemma Doughty-Jones and Yvonne Spychala are thanked for clear and constructive reviews which greatly improved the manuscript, and for providing the foundations for which much of this work is based. Associate Editor Steve Hubbard and Editors Gary Hampson and John Southard are thanked for their handling of the manuscript.

REFERENCES

Ábalos, B., 2016, Geologic map of the Basque–Cantabrian Basin and a new tectonic interpretation of the Basque Arc: International Journal of Earth Sciences, v. 105, p. 2327–2354.

Agirrezabala, L.M., 1996, El Aptiense–Albiense del Anticlinorio Nor-Vizcaino entre Gernika y Azpeitia [Ph.D. Thesis]: Euskal Herriko Unibertsitatea, Bilbao, 429 p.

Agirrezabala, L.M., and Bodego, A., 2005, Interbedded mudstone slope and basin-floor sandy deposits in the Ondarroa turbidite system (Albian, Basque–Cantabrian Basin): Geogaceta, v. 38, p. 83–86.

Agirrezabala, L.M., and Dinarés-Turell, J., 2013, Albian syndepositional block rotation and its geological consequences, Basque–Cantabrian Basin (Western Pyrenees): Geological Magazine, v. 150, p. 986–1001.

Agirrezabala, L.M., and García-Mondéjar, J., 1989, Evolución tectosedimentaria de la plataforma urgoniana entre Cabo Ogoño e Itziar durante el Albiense inferior y medio (Región Vasco–Cantábrica nor-oriental): Del XII Congreso Español de Sedimentología Simposio, Leioa 11-20.

Agirrezabala, L.M., and López-Horgue, M., 2017, Environmental and ammonoid faunal changes related to Albian Bay of Biscay opening: insights from the northern margin of the Basque–Cantabrian Basin: Journal of Sea Research, v. 130, p. 36–48.

Al-Ja'aidi, 2000, The influence of topography and flow efficiency on the deposition of turbidites [Ph.D. Thesis]: University of Leeds, 162 p.

Alves, T.M., Gawthorpe, R.L., Hunt, D.W., and Monteiro, J.H., 2002, Jurassic tectono-sedimentary evolution of the Northern Lusitanian Basin (offshore Portugal): Marine and Petroleum Geology, v. 19, p. 727–754.

Alves, T.M., Manuppella, G., Gawthorpe, R.L., Hunt, D.W., and Monterio, J.H., 2003, The depositional evolution of diapir- and fault-bounded rift basins: examples from the Lusitanian Basin of West Iberia: Sedimentary Geology, v. 162, p. 273–303.

Amy, L.A., McCaffrey, W.D., and Kneller, B.C., 2004, The influence of a lateral basin-slope on the depositional patterns of natural and experimental turbidity currents, *in* Lomas, S.A., and Joseph, P., eds., Confined Turbidite Systems: Geological Society of London, Special Publication 222, p. 311–330.

Apps, G.M., 1987, Evolution of the Grès d'Annot Basin, South West Alps [Ph.D. Thesis]: University of Liverpool, 434 p.

Armitage, D.A., Romans, B.W., Covault, J.A., and Graham, S.A., 2009, The influence of mass-transport-deposit surface topography on the evolution of turbidite architecture: the Sierra Contreras, Tres Pasos Formation (Cretaceous), southern Chile: Journal of Sedimentary Research, v. 79, p. 287–301.

Baas, J.H., 2004, Conditions for formation of massive turbiditic sandstones by primary depositional processes: Sedimentary Geology, v. 166, p. 292–310.

Baas, J.H., Best, J.L., Peakall, J., and Wang, M., 2009, A phase diagram for turbulent, transitional, and laminar clay suspension flows: Journal of Sedimentary Research, v. 79, p. 162–183.

Baas, J.H., Best, J.L., and Peakall, J., 2011, Depositional processes, bedform development and hybrid bed formation in rapidly decelerated cohesive (mud–sand) sediment flows: Sedimentology, v. 58, p. 1953–1987.

Baas, J.H., Davies, A.G., and Malarkey, J., 2013, Bedform development in mixed sand–mud: the contrasting role of cohesive forces in flow and bed: Geomorphology, v. 182, p. 19–32.

Bakke, K., Kane, I.A., Martinsen, O.J., Petersen, S.A., Johansen, T.A., Hustoft, S., Hadler, J., and Groth, A., 2013, Seismic modeling in the analysis of deep-water sandstone termination styles: American Association of Petroleum Geologists, Bulletin, v. 97, p. 1395–1419.

Banham, S.G., and Mountney, N.P., 2013a, Evolution of fluvial systems in salt-walled mini-basins: a review and new insights: Sedimentary Geology, v. 296, p. 142–166.

Banham, S.G., and Mountney, N.P., 2013b, Controls on fluvial sedimentary architecture and sediment-fill state in salt-walled mini-basins: Triassic Moenkopi Formation, Salt Anticline Region, SE Utah, USA: Basin Research, v. 25, p. 709–737.

Banham, S.G., and Mountney, N.P., 2014, Climatic versus halokinetic control on sedimentation in a dryland fluvial succession: Sedimentology, v. 61, p. 570–608.

Barker, S.P., Haughton, P.D.W., McCaffrey, W.D., Archer, S.G., and Hakes, B., 2008, Development of rheological heterogeneity in clay-rich high-density turbidity currents: Aptian Britannia Sandstone Member, UK continental shelf: Journal of Sedimentary Research, v. 78, p. 45–68.

Barr, B.C., Slinn, D.N., Pierro, T., and Winters, K.B., 2004, Numerical simulation of turbulent, oscillatory flow over sand ripples: Journal of Geophysical Research, Oceans, v. 109, C9.

Bodego, A., and Agirrezabala, L.M., 2013, Syn-depositional thin- and thick-skinned extensional tectonics in the mid Cretaceous Lasarte sub-basin, western Pyrenees: Basin Research, v. 25, p. 594–612.

Booth, J.R., Dean, M.C., Duvernay, A.E., and Styzen, M.J., 2003, Paleo-bathymetric controls on the stratigraphic architecture and reservoir development of confined fans in the Auger Basin: Central Gulf of Mexico slope: Marine and Petroleum Geology, v. 20, p. 563–586.

Boulesteix, K., Poyatos-More, M., Flint, S.S., Taylor, K.G., Hodgson., D.M., and Hasiotis, S.T., 2019, Transport and deposition of mud in deep-water environments: processes and stratigraphic implications: Sedimentology, v. 66, p. 2894–2925.

Brooks, H.L., Hodgson, D.M., Brunt, R.L., Peakall, J., Hofstra, M., and Flint, S.S., 2018, Deep-water channel–lobe transition zone dynamics: processes and depositional architecture, an example from the Karoo Basin, South Africa: Geological Society of America, Bulletin, v. 130, p. 1–10.

Brunet, M.F., 1994, Subsidence in the Parentis Basin (Aquitaine, France): implications of the thermal evolution, *in* Mascle, A., ed., Hydrocarbon and Petroleum Geology of France: European Association of Petroleum Geoscientists, Special Publication 4, p. 187–198.

Cámara, P., 2017, Salt and strike-slip tectonics as main drivers in the structural evolution of the Basque–Cantabrian Basin, Spain, *in* Soto, J.I., Flinch, J.F., and Tari, G., eds., Permo-Triassic Salt Provinces of Europe, North Africa and the Atlantic Margins: Elsevier, p. 371–393.

Carr, I.D., Gawthorpe, R.L., Jackson, C.A-L., Sharp, I.R., and Sadek, A., 2003, Sedimentology and sequence stratigraphy of early syn-rift tidal sediments: the Nukhul Formation, Suez Rift, Egypt: Journal of Sedimentary Research, v. 73, p. 407–420.

Carruthers, D., Cartwright, J., Jackson, M.P.A., and Schutjens, P., 2013, Origin and timing of layer-bound radial faulting around North Sea salt stocks: new insights into the evolving stress state around rising diapirs: Marine and Petroleum Geology, v. 48, p. 130–48.

Charles, R., and Ryzhikov, K., 2015, Merganser Field: managing subsurface uncertainty during the development of a salt diapir field in the UK Central North Sea, *in* McKie, T., Rose, P.T.S., Hartley, A.J., Jones, D.W., and Armstrong, T.L., eds., Tertiary Deep-Marine Reservoirs of the North Sea Region: Geological Society of London, Special Publication 403, p. 261–298.

Clark, I.A., and Cartwright., J.A., 2009, Interactions between submarine channel systems and deformation in deepwater fold belts: examples from the Levant Basin, Eastern Mediterranean Sea: Marine and Petroleum Geology, v. 26, p. 1465–1482.

Clark, I.A., and Cartwright., J.A., 2011, Key controls on submarine channel development in structurally active settings: Marine and Petroleum Geology, v. 28, p. 1333–1349.

Counts, J.W., and Amos, K., 2016, Sedimentology, depositional environments and significance of an Ediacaran salt-withdrawal minibasin, Billy Springs Formation, Flinders Ranges, South Australia: Sedimentology, v. 63, p. 1084–1123.

Counts, J.W., Dalgarno, C.R., Amos, K.J., and Hasiotis, S.T., 2019, Lateral facies variability along the margin of an outcropping salt-withdrawal minibasin, South Australia: Journal of Sedimentary Research, v. 89, p. 28–45.

Cronin, B.T., Owen, D., Hartley, A.J., and Kneller, B., 1998, Slumps, debris flows and sandy deep-water channel systems: implications for the application of sequence stratigraphy to deep-water clastic sediments: Geological Society of London, Journal, v. 155, p. 429–432.

Crimes, T.P., 1973, From limestones to distal turbidites: a facies and trace fossil analysis in the Zumaya flysch (Paleocene–Eocene), North Spain: Sedimentology, v. 20, p. 105–131.

Cullen, T.M., Collier, R.E.L., Gawthorpe, R.L., Hodgson, D.M., and Barrett, B.J., 2019, Axial and transverse deep-water sediment supply to syn-rift fault terraces: insights from the West Xylokastro Fault Block, Gulf of Corinth, Greece: Basin Research, v. 32, p. 1115–1149.

Cumberpatch, Z.A., Soutter, E.L., Kane, I.A., and Casson, M.A., 2021, Evolution of a mixed siliciclastic–carbonate deep-marine system on an unstable margin: the Cretaceous of the Eastern Greater Caucasus, Azerbaijan: Basin Research, v. 33, p. 612–647.

Dalgarno, C.R., and Johnson, J.E., 1968, Diapiric structures and late Precambrian–early Cambrian sedimentation in Flinders Ranges, South Australia, *in* Braunstein, J., and O'Brien, G.D., eds., Diapirism and Diapirs: American Association Petroleum Geologist, Memoir 8, p. 301–314.

Davison, I., Alsop, G.I., Evans, N.G., and Safaricz, M., 2000, Overburden deformation patterns and mechanisms of salt diapir penetration in the Central Graben, North Sea: Marine and Petroleum Geology, v. 17, p. 601–618.

De Blasio, F.V., Engvik, L.E., and Elverhøi, A., 2006, Sliding of outrunner blocks from submarine landslides: Geophysical Research Letters, v. 30, doi:10.1029/2005GL025165.

DeFelipe, I., Pedreira, D., Pulgar, J.A., Iriarte, E., and Medina, M., 2017, Mantle exhumation and metamorphism in the Basque–Cantabrian Basin (N Spain): stable and clumped isotope analysis in carbonates and comparison with ophicalcites in the North-Pyrenean Zone (Urdach and Lherz): Geochemistry, Geophysics, Geosystems, v. 18, p. 631–652.

Deptuck, M., and Sylvester, Z., 2017, Submarine fans and their channels, levees and lobes, *in* Micallef, A., Krastel, S., and Savini, A., eds., Submarine Geomorphology: Springer, p. 273–299.

Doughty-Jones, G., Mayall, M., and Lonergan, L., 2017, Stratigraphy, facies, and evolution of deep-water lobe complexes within a salt controlled intraslope minibasin: American Association of Petroleum Geologists, Bulletin, v. 101, p. 1879–1904.

Doughty-Jones, G., Lonergan, L., Mayall, M., and Dee, S.J., 2019, The role of structural growth in controlling the facies and distribution of mass transport deposits in a deep-water salt minibasin: Marine and Petroleum Geology, v. 104, p. 106–124.

Dyson, I.A., 1999, The Beltana Diapir: a salt withdrawal mini-basin in the northern Flinders Ranges: Mines and Energy of South Australia, Journal, v. 15, p. 40–46.

Ericson, D.B., Ewing, M., and Heezen, B.C., 1952, Turbidity currents and sediments in North Atlantic: American Association of Petroleum Geologists, Bulletin, v. 36, p. 489–511.

Espejo, J., 1973, Mapa Geológico de España, Hoja 38 (Bermeo), Instituto Geológico y Minero de España, Segunda Serie, Primera Edición, scale 1:50,000.

Espejo, J., and Pastor, F., 1973, Mapa Geológico de España, Hoja 37 (Algorta), Instituto Geológico y Minero de España, Segunda Serie, Primera Edición, scale 1:50,000.

Etienne, S., Mulder, T., Bez, M., Desaubliaux, G., Kwasniewski, A., Parize, O., Dujoncquoy, E., and Salles, T., 2012, Multiple scale characterization of sand-rich distal lobe deposit variability: examples from the Annot Sandstones Formation, Eocene–Oligocene, SE France: Sedimentary Geology, v. 273–274, p. 1–18.

Ferrer, O., Roca, E., Benjumea, B., Muñoz, J., and Ellouz, N., 2008, The deep seismic reflection MARCONI-3 profile: role of extensional Mesozoic structure during the Pyrenean contractional deformation at the eastern part of the Bay of Biscay: Marine and Petroleum Geology, v. 25, p. 714–730.

Ferrer, O., Arbues, P., Roca, E., Giles, K., Rowan, M., Matties, M., and Muñoz, J., 2014, Effects of diapir growth on synkinimatic deepwater sedimentation: the Bakio diapir (Basque–Cantabrian Basin, northern Spain): American Association of Petroleum Geologist, Search and Discovery article 41385.

Flint, S.S., and Hodgson, D.M., 2005, Submarine slope systems: processes and products *in* Hodgson, D.M., and Flint, S.S., eds., Submarine Slope Systems: Processes and Products: Geological Society of London, Special Publication 244, p. 1–6.

García-Mondéjar, J., 1990, The Aptian–Albian carbonate episode of the Basque–Cantabrian basin (northern Spain) general characteristics controls and evolution, *in* Tucker, M.E., Wilson, J.L., Crevello, P.D., Sarg, J.F., and Read, J.F., eds., Carbonate Platforms: Facies, Sequences and Evolution: International Association of Sedimentologists, Special Publication 9, p. 257–290.

García-Mondéjar, J., 1996, Plate reconstruction of the Bay of Biscay: Geology, v. 24, p. 635–638.

García-Mondéjar, J., and Robador, A., 1987, Sedimentacion y paleogeografía la del Complejo Urgoniano (Aptiense–Albiense) en el area de Bermeo (region Vasco–Cantabrica septentrional): Acta Geologica Hispanica, v. 22, p. 411–418.

García-Mondéjar, J., Fernandez-Mendiola, P.A., Agirrezabala, L.M., Aranburu, A., Lôpez-Horgue, M.A., Iriarte, E., and Martinez de Rituerto, S., 2004, El Aptiense–Albiense de la Cuenca Vascao–Cantabrica: Geologica de España, p. 291–296.

Garrote-Ruiz, A., García-Potero, J.A., Eguiguren-Altuna, E., and García-Pascual, I., 1991, Mapa de la Hoja, no. 38-I (Bermeo) del Mapa Geológico del País Vasco: Bilbao, Ente Vasco de la Energía, scale 1:25,000.

Garrote-Ruiz, A., García-Potero, J.A., Eguiguren-Altuna, E., and García-Pascual, I., 1992, Mapa de la Hoja no. 38-III (Mungia) del Mapa Geológico del País Vasco: Bilbao, Ente Vasco de la Energía, scale 1:25,000.

Garrote-Ruiz, A., García-Potero, J.A., Eguiguren-Altuna, E., and García-Pascual, I., 1993a, Mapa de la Hoja no. 37-II (Armintza) del Mapa Geológico del País Vasco: Bilbao, Ente Vasco de la Energía, scale 1:25,000.

Garrote-Ruiz, A., García-Potero, J.A., Eguiguren-Altuna, E., and García-Pascual, I., 1993b, Mapa de la Hoja no. 37-IV (Getxo) del Mapa Geológico del País Vasco: Bilbao, Ente Vasco de la Energía, scale 1:25,000.

Gee, M.J.R., and Gawthorpe, R.L., 2006, Submarine channels controlled by salt tectonics: examples form 3D seismic data offshore Angola: Marine and Petroleum Geology, v. 22, p. 443–458.

Gee, M.J.R., and Gawthorpe, R.L., 2007, Seismic geomorphology and evolution of submarine channels from the Angolan continental margin: Journal of Sedimentary Research, v. 77, p. 433–446.

Geluk, M., McKie, T., and Kilhams, B., 2018, An introduction to the Triassic: current insights into the regional setting and energy resource potential of NW Europe, *in* Kilhams, B., Kukla, P.A., Mazur, S., McKie, T., Mijnlieff, H.F., and Van Ojik, K., eds., Mesozoic Resource Potential in the Southern Permian Basin: Geological Society of London, Special Publication 469, p. 139–147.

Gervais, A., Sayoye, B., Mulder, T., and Gonthier, E., 2006, Sandy modern turbidite lobes: a new insight from high resolution seismic data: Marine and Petroleum Geology, v. 23, p. 485–502.

Giles, K., and Lawton, T., 2002, Halokinetic sequence stratigraphy adjacent to the El Papalote diapir, northeastern Mexico: American Association of Petroleum Geologists, Bulletin, v. 86, p. 823–840.

Giles, K., and Rowan, M., 2012, Concepts in halokinetic-sequence deformation and stratigraphy, *in* Alsop, G.I., Archer, S.G., Hartley, A.J., Grant, N.T., and Hodgkinson, R., eds., Salt Tectonics, Sediments and Prospectivity: Geological Society of London, Special Publication 363, p. 7–31.

Gómez, M., Vergés, J., and Riaza, C., 2002, Inversion tectonics of the northern margin of the Basque–Cantabrian Basin: Société Géologique de France, Bulletin, v. 173, p. 449–459.

Gorsline, D.S., and Emery, K.O., 1959, Turbidity-current deposits in San Pedro and Santa Monica basins off southern California: Geological Society of America, Bulletin, v. 70, p. 279–290.

Grant, R., Underhill, J., Hernández-Casado, J., Barker, S., and Jamieson, R., 2019, Upper Permian Zechstein Supergroup carbonate–evaporite platform palaeomorphology in the UK Southern North Sea: Marine and Petroleum Geology, v. 100, p. 484–518.

Grant, R.J., Underhill, J.R., Hernández-Casado, J., Jamieson, R.J., and Williams, R.M., 2020a, The evolution of the Dowsing Graben System: implications for petroleum prospectivity in the UK Southern North Sea: Petroleum Geoscience, v. 27, p. 64–80.

Grant, R.J., Booth, M.G., Underhill, J.R., and Bell, A., 2020b, Structural evolution of the Breagh area: implications for the carboniferous prospectivity of the Mid North Sea High, Southern North Sea: Petroleum Geoscience, v. 26, p. 174–203.

Hampton, M.A., 1972, The Role of subaqueous debris flow in generating turbidity currents: Journal of Sedimentary Petrology, v. 42, p. 775–793.

Haq, B.U., 2014, Cretaceous eustasy revisited: Global and Planetary Change, v. 113, p. 44–58.

Haq, B.U., Hardenbol, J., and Vail, P.R., 1987, Chronology of fluctuating sea levels since the Triassic (250 million years ago to present): Science, v. 235, p. 1156–1167.

Haughton, P.D.W., 1994, Deposits of deflected and ponded turbidity currents, Sorbas basin, southeast Spain: Journal of Sedimentary Research, v. 64, p. 233–246.

Haughton, P.D.W., Davis, C., McCaffrey, W., and Barker, S., 2009, Hybrid sediment gravity flow deposits: classification, origin and significance: Marine and Petroleum Geology, v. 26, p. 1900–1918.

Hay, D.C., 2012, Stratigraphic evolution of a tortuous corridor from the stepped slope of Angola, *in* Prather, B.E., Deptuck, M.E., Mohrig, D., Hoorn, B.V., and Wynn, R.B., eds., Application of the Principles of Seismic Geomorphology to Continental Slope and Base-of-Slope Systems: Case Studies from Seafloor and Near-Seafloor Analogues: SEPM, Special Publication 99, p. 163–180.

Hodgetts, D., 2013, Laser scanning and digital outcrop geology in the petroleum industry: a review: Marine and Petroleum Geology, v. 46, p. 335–354.

Hodgson, D.M., 2009, Distribution and origin of hybrid beds in sand-rich submarine fans of the Tanqua depocenter, Karoo Basin, South Africa: Marine and Petroleum Geology, v. 26, p. 1940–1956.

Hodgson, D.M., and Haughton, P.D.W., 2004, Impact of syndepositional faulting on gravity current behaviour and deep-water stratigraphy: Tabernas–Sorbas Basin, SE Spain, *in* Lomas, S.A., and Joseph, P., eds., Confined Turbidite Systems: Geological Society of London, Special Publication 222, p. 135–158.

Hodgson, D.M., Di Celma, C.N., Brunt, R.L., and Flint, S.S., 2011, Submarine slope degradation and aggradation and the stratigraphic evolution of channel–levee systems: Geological Society of London, Journal, v. 168, p. 625–628.

Hodgson, D.M., Kane, I.A., Flint, S.S., Brunt, R.L., and Ortiz Karpf, A., 2016, Time-transgressive confinement on the slope and the progradation of basin-floor fans: implications for the sequence boundary of deep-water deposits: Journal of Sedimentary Research, v. 86, p. 73–86.

Hodgson, N.A., Farnsworth, J., and Fraser, A.J., 1992, Salt-related tectonics, sedimentation and hydrocarbon plays in the Central Graben, North Sea, UKCS, *in* Hardman, R.F.P., ed., Exploration Britain: Geological Insights for the Next Decade: Geological Society of London, Special Publication 67, p. 31–63.

Hofstra, M., Hodgson, D.M., Peakall, J., and Flint, S.S., 2015, Giant scour-fills in ancient channel–lobe transition zones: formative processes and depositional architecture: Sedimentary Geology, v. 329, p. 98–114.

Howlett, D.M., Gawthorpe, R.L., Ge, Z., Rotevatn, A., and Jackson, C.A-L., in press, Turbidites, topography and tectonics: evolution of submarine channel–lobe systems in the salt-influenced Kwanza Basin, offshore Angola: Basin Research, doi.org/10.1111/bre.12506.

Hubbard, S.M., Romans, B.W., and Graham, S.A., 2008, Deep-water foreland basin deposits of the Cerro Toro Formation, Magallanes basin, Chile: architectural elements of a sinuous basin axial channel belt: Sedimentology, v. 55, p. 1333–1359.

Hubbard, S.M., Covault, J.A., Fildani, A., and Romans, B.W., 2014, Sediment transfer and deposition in slope channels: deciphering the record of enigmatic deep-sea processes from outcrop: Geological Society of America, Bulletin, v. 126, p. 857–871.

Hudec, M., and Jackson, M., 2007, Terra infirma: understanding salt tectonics: Earth-Science Reviews, v. 82, p. 1–28.

Hunnicutt, L.A., 1998, Tectonostratigraphic interpretation of Upper Cretaceous to lower Tertiary limestone lentils within the Potrerillos Formation surrounding El Papalote diapir, La Popa basin, Nuevo Leon, Mexico [MS Thesis]: New Mexico State University, Las Cruces, 181 p.

Iverson, R.M., 1997, The physics of debris flows: Reviews of Geophysics, v. 35, p. 245–296.

Iverson, R.M., Logan, M., Lahusen, R.G., and Berti, M., 2010, The perfect debris flow? Aggregated results from 28 largescale experiments: Journal of Geophysical Research: Earth Surface, v. 115, p. 1–29.

Jackson, C.A-L., and Johnson, H.D., 2009, Sustained turbidity currents and their interaction with debrite-related topography; Labuan Island: Sedimentary Geology, v. 219, p. 77–96.

Jackson, C.A-L., Gawthorpe, R.L., and Sharp, I.R., 2002, Growth and linkage of the East Tanka fault zone, Suez rift: structural style and syn-rift stratigraphic response: Geological Society of London, Journal, v. 159, p. 175–187.

Jackson, C.A-L., Gawthorpe, R.L., Carr, I.D., and Sharp, I.R., 2005, Normal faulting as a control on the stratigraphic development of shallow marine syn-rift sequences: the Nukhul and Lower Rudeis formations, Hammam Faraun fault block, Suez Rift, Egypt: Sedimentology, v. 52, p. 313–338.

Jackson, M.P.A., and Hudec, M.R., 2017, Salt Tectonics: Principles and Practise: Cambridge University Press, 515 p.

Janocko, M., Nemec, W., Henriksen, S., and Warchol, M., 2013, The diversity of deep-water sinuous channel belts and slope valley-fill complexes: Marine and Petroleum Geology, v. 41, p. 7–34.

Jammes, S., Mannatschal, G., Lavier, L., and Masini, E., 2009, Tectonosedimentary evolution related to extreme crustal thinning ahead of a propagating ocean: an example of the western Pyrenees; Tectonophysics, v. 28, p. 1–24.

Jobe, Z.R., Lowe, D.R., and Morris, W.R., 2012, Climbing-ripple successions in turbidite systems: depositional environments, sedimentation and accumulation times: Sedimentology, v. 59, p. 867–898.

Jobe, Z.R., Howes, N.C., and Auchter, N.C., 2016, Comparing submarine and fluvial channel kinematics: implications for stratigraphic architecture: Geology, v. 44, p. 931–934.

Jobe, Z.R., Sylvester, Z., Howes, N., Pirmez, C., Parker, A., Cantelli, A., Smith, R., Wolinsky, M.A., O'Byrne, C., Slowey, N., and Prather, B., 2017, High-resolution, millennial-scale patterns of bed compensation on a sand-rich intraslope submarine fan, western Niger Delta slope: Geological Society of America, Bulletin, v. 129, p. 23–37.

Johnson, S.D., Flint, S., Hinds, D., and Wickens, H.D., 2001, Anatomy, geometry and sequence stratigraphy of basin floor to slope turbidite systems, Tanqua Karoo, South Africa: Sedimentology, v. 48, p. 987–1023.

Jones, G., Mayall, M., and Lonergan, L., 2012, Contrasting depositional styles on a slope system and their control by salt tectonics: through-going channels, ponded fans, and mass transport complexes, *in* Rosen, N.C., Weimer, P., Coutes Dos Anjos, S., Henrickson, E., Marques, E., Mayall, M., and Fillon, R., eds., New Understanding of the Petroleum Systems of Continental Margins of the World: SEPM, Gulf Coast Section, 32nd Annual Bob F. Perkins Research Conference, Houston, p. 503–533.

Jones, I.F., and Davison, I., 2014, Seismic imaging in and around salt bodies: Interpretation, v. 2, p. 1–20.

Kane, I.A., and Hodgson, D.M., 2011, Sedimentological criteria to differentiate submarine channel–levee subenvironments: exhumed examples from the Rosario Fm. (Upper

Cretaceous) of Baja California, Mexico, and the Fort Brown Fm. (Permian), Karoo Basin, S. Africa: Marine and Petroleum Geology, v. 28, p. 807–823.

Kane, I.A., and Pontén, A.S.M., 2012, Submarine transitional flow deposits in the Paleogene Gulf of Mexico: Geology, v. 40, p. 1119–1122.

Kane, I.A., McCaffrey, W.D., and Martinsen, O.J., 2009, Allogenic vs. autogenic controls on megaflute formation: Journal of Sedimentary Research, v. 79, p. 643–651.

Kane, I.A., Catterall, V., McCaffrey, W.D., and Martinsen, O.J., 2010, Submarine channel response to intrabasinal tectonics: the influence of lateral tilt: American Association of Petroleum Geologists, Bulletin, v. 94, p. 189–219.

Kane, I.A., McGee, D.T., and Jobe, Z.R., 2012, Halokinetic effects on submarine channel equilibrium profiles and implications for facies architecture: conceptual model illustrated with a case study from Magnolia Field, Gulf of Mexico *in* Alsop, G.I., Archer, S.G., Hartley, A.J., Grant, N.T., and Hodgkinson, R., eds., Salt Tectonics, Sediments and Prospectivity: Geological Society of London, Special Publication 363, p. 289–302.

Kane, I.A., Pontén, A.S., Vangdal, B., Eggenhuisen, J.T., Hodgson, D.M., and Spychala, Y.T., 2017, The stratigraphic record and processes of turbidity current transformation across deep-marine lobes: Sedimentology, v. 64, p. 1236–1273.

Kernen, R.A., Giles, K.A., Rowan, M.G., Lawton, T.F., and Hearon, T.E., 2012, Depositional and halokinetic-sequence stratigraphy of the Neoproterozoic Wonoka Formation adjacent to Patawarta allochthonous salt sheet, Central Flinders Ranges, South Australia, *in* Alsop, G.I., Archer, S.G., Hartley, A.J., Grant, N.T., and Hodgkinson, R., eds., Salt Tectonics, Sediments and Prospectivity: Geological Society of London, Special Publication 363, p. 81–105.

Kernen, R.A., Giles, K.A., Poe, P.L., Gannaway Dalton, C.E., Rowan, M.G., Fiduck, J.C., and Hearon, T.E., 2018, Origin of the Neoproterozoic rim dolomite as lateral carbonate caprock, Patawarta Salt Sheet, Flinders Ranges, South Australia: Australian Journal of Earth Sciences, v. 67, p. 815–832.

Kilhams, B.A., Hartley, A., Huuse, M., Davis, C., 2012, Characterizing the Paleocene turbidites of the North Sea: the Mey Sandstone Member, Lista Formation, UK Central Graben: Petroleum Geoscience, v. 18, p. 337–354.

Kilhams, B.A., Hartley, A., Huuse, M., and Davis, C., 2015, Characterizing the Paleocene turbidites of the North Sea: Maureen Formation, UK Central Graben, *in* McKie, T., Rose, P.T.S., Hartley, A.J., Jones, D.W., and Armstrong, T.L., eds., Tertiary Deep-Marine Reservoirs of the North Sea Region: Geological Society of London, Special Publication 403, p. 43–62.

Kneller, B.C., and Branney, M.J., 1995, Sustained high-density turbidity currents and the deposition of thick massive sands: Sedimentology, v. 42, p. 607–616.

Kneller, B.C., and McCaffrey, W.D., 1999, Depositional effects of flow non-uniformity and stratification within turbidity currents approaching a bounding slope: deflection, reflection, and facies variation: Journal of Sedimentary Research, v. 69, p. 980–991.

Kneller, B.C., Edwards, D., McCaffrey, W.D., and Moore, R., 1991, Oblique reflection of turbidity currents: Geology, v. 19, p. 250–252.

Kneller, B., Dykstra, M., Fairweather, L., and Milana, J.P., 2016, Mass-transport and slope accommodation: implications for turbidite sandstone reservoirs: American Association of Petroleum Geologists, Bulletin, v. 100, p. 213–235.

Laudon, R.C., 1975, Stratigraphy and petrology of the Difunta Group, La Popa and eastern Parras Basins, northeastern Mexico [Ph.D. Thesis]: The University of Texas, Austin.

Leeder, M.R., and Gawthorpe, R.L., 1987, Sedimentary models for extensional tilt-block/half-graben basins, *in* Coward, M.P., Dewey, J.F., and Hancock, P.L., eds., Continental Extensional Tectonics: Geological Society of London, Special Publication 28, p. 139–152.

Leppard, C.W., and Gawthorpe, R.L., 2006, Sedimentology of rift climax deep water systems: Lower Rudeis Formation, Hammam Faraun Fault Block, Suez Rift, Egypt: Sedimentary Geology, v. 191, p. 67–87.

Lerche, I., and Petersen, K., 1995, Salt and Sediment Dynamics: London, CRC Press, 336 p.

Li, P., Kneller, B.C., Hansen, L., and Kane, I.A., 2016, The classical turbidite outcrop at San Clemente, California revisited: an example of sandy submarine channels with asymmetric facies architecture: Sedimentary Geology, v. 346, p. 1–16.

López-Horgue, M.A., Owen, H.G., Aranburu, A., Fernández-Mendiola, P.A., and García-Mondéjar, J., 2009, Early late Albian (Cretaceous) of the central region of the Basque–Cantabrian Basin, northern Spain: biostratigraphy based on ammonites and orbitolinids: Cretaceous Research, v. 30, p. 385–400.

Lotze, F., 1953, Salzdiapirismus im nördlichen Spanien: Deutschen Geologische Gesellschaft, Zeitschrift, v. 105, p. 814–822.

Lowe, D.R., 1982, Sediment gravity flows II, depositional models with special reference to the deposits of high-density turbidity currents: Journal of Sedimentary Petrology, v. 52. p. 279–297.

Lowe, D.R., and Guy, M., 2000, Slurry-flow deposits in the Britannia Formation (Lower Cretaceous), North Sea: a new perspective on the turbidity current and debris flow problem: Sedimentology, v. 47, p. 31–70.

Macdonald, H.A., Peakall, J., Wignall, P.B., and Best, J., 2011, Sedimentation in deep-sea lobe-elements: implications for the origin of thickening-upward sequences: Geological Society of London, Journal, v. 168, p. 319–331.

Madof, A.S., Christie-Blick, N., and Anders, M.H., 2009, Stratigraphic controls on a salt-withdrawal intraslope minibasin, north-central Green Canyon, Gulf of Mexico: implications for misinterpreting sea-level change: American Association of Petroleum Geologists, Bulletin, v. 93, p. 636–561.

Mannie, A.S., Jackson, C.A-L., and Hampson, G.J., 2014, Shallow-marine reservoir development in extensional diapir-collapse minibasins: an integrated subsurface case study from the Upper Jurassic of the Cod terrace, Norwegian North Sea: American Association of Petroleum Geologists, Bulletin, v. 98, p. 2019–2055.

Mathey, B., 1987, Les Flyschs Crétacé supérieur des Pyrénées Basques: âge, anatomie, origine du matériel, milieu de dépôt et la relation avec l'ouverture du Golfe de Gascogne [Ph.D. Thesis]: Université de Bourgogne, Dijon, 403 p.

Marini, M., Milli, S., Ravnås, R., and Moscatelli, M., 2015, A comparative study of confined vs. semi-confined turbidite lobes from the Lower Messinian Laga Basin (Central Apennines, Italy): implications for assessment of reservoir architecture: Marine and Petroleum Geology, v. 63, p. 142–165.

Martín-Chivelet, J., Breastegui, X., and Rosales, I., et al., 2002, Cretaceous, *in* Gibbons, W., and Moreno, T., eds., The Geology of Spain: Geological Society of London, 668 p.

Martín-Martín, J.D., Vergés, J., Saura, E., Moragas, M., Messager, G., Baqués, V., Razin, P., Grélaud, C., Malaval, M., Joussiaume, R., Casciello, E., Cruz-Orasa, I., and Hunt, D.W., 2016, Diapiric growth within an Early Jurassic rift basin: the Tazoult salt wall (central High Atlas, Morocco): Tectonics, v. 36, p. 2–32.

Mayall, M., Jones, E., and Casey, M., 2006, Turbidite channel reservoirs: key elements in facies prediction and effective development: Marine and Petroleum Geology, v. 23, p. 821–841.

Mayall, M., Lonergan, L., Bowmn, A., James, S., Milles, K., Primmer, T., Pope, D., Rogers, L., and Skeene, R., 2010, The response of turbidite slope channels to growth-induced seabed topography: American Association of Petroleum Geologists, Bulletin, v. 94, p. 1011–1030.

McArthur, A., Kane, I.A., Bozetti, G., Hansen, L., and Kneller, B.C., 2020, Supercritical flows overspilling from bypass-dominated submarine channels and the development of overbank bedforms: The Depositional Record, v. 6, p. 21–40.

McBride, E.F., Weidie, A.E., Wolleben, J.A., and Laudon, R.C., 1974, Stratigraphy and structure of the Parras and La Popa basins, northeastern Mexico: Geological Society of America, Bulletin, v. 85, p. 1603–1622.

McCaffrey, W.D., and Kneller, B.C., 2001, Process controls on the development of stratigraphic trap potential on the margins of confined turbidite systems and aids to reservoir evaluation: American Association of Petroleum Geologists, Bulletin, v. 85, p. 971–988.

Morris, E.A., Hodgson, D.M., Flint, S.S., Brunt, R.L., Butterworth, P.J., and Verhaeghe, J., 2014, Sedimentology, stratigraphic architecture, and depositional context of submarine frontal-lobe complexes: Journal of Sedimentary Research, v. 84, p. 763–780.

Moscardelli, L., and Wood, L., 2008, New classification system for mass transport complexes in offshore Trinidad: Basin Research, v. 20, p. 73–98.

Mutti, E., 1974, Examples of ancient deep-sea fan deposits from circum Mediterranean geosynclines in modern and ancient geosynclinal sedimentation, *in* Dott, R.H., Jr., and Shaver, R.H., eds., Modern and Ancient Geosynclinal Sedimentation: Society of Economic Paleontologists and Mineralogists, Special Publication 19, p. 92–105.

Mutti, E., 1992, Turbidite Sandstones: Instituto di Geologia, Università di Parma, 275 p.

Mutti, E., and Normark, W.R., 1987, Comparing examples of modern and ancient turbidite systems: problems and concepts, *in* Leggett, J.K., and Zuffa, G.G., eds., Marine Clastic Sedimentology: concepts and case studies: London, Graham and Trotman, p. 1–38.

Nardin, T.R., Hein, F.J., Gorsline, D.S., and Edwards, B.D., 1979, A review of mass movement processes, sediment and acoustic characteristics, and contrasts in slope and base-of-slope systems versus canyon-fan-basin floor systems, *in* Doyle, L.J., and Pilkey, O.H., eds., Geology of Continental Slopes: SEPM, Special Publication 27, p. 61–73.

Normark, W.R., Piper, D.J.W., and Hess, G.R., 1979, Distributary channels, sand lobes, and mesotopography of navy submarine fan, California Borderland, with application to ancient fan sediments: Sedimentology, v. 26, p. 749–774.

Olafiranye, K., Jackson, C.A-L., and Hodgson, D.M., 2013, The role of tectonics and mass-transport complex emplacement on upper slope stratigraphic evolution: a 3D seismic case study from offshore Angola: Marine and Petroleum Geology, v. 44, p. 196–216.

Oluboyo, A.P., Gawthorpe, R.L., Bakke, K., and Hadler-Jacobsen, F., 2014, Salt tectonic controls on deep-water turbidite depositional systems: Miocene, southwestern Lower Congo Basin, offshore Angola: Basin Research, v. 26, p. 597–620.

Ortiz-Karpf, A., Hodgson, D.M., and McCaffrey, W.D., 2015, The role of mass-transport complexes in controlling channel avulsion and the subsequent sediment dispersal patterns on an active margin: the Magdalena Fan, offshore Colombia: Marine and Petroleum Geology, v. 64, p. 58–75.

Ortiz-Karpf, A., Hodgson, D.M., Jackson, C.A-L., and McCaffrey, W.D., 2016, Mass-transport complexes as markers of deep-water fold-and-thrust belt evolution: insights from the southern Magdalena Fan, offshore Colombia: Basin Research, v. 30, p. 65–88.

Patacci, M., Haughton, P.D., and McCaffrey, W.D., 2014, Rheological complexity in sediment gravity flows forced to decelerate against a confining slope, Braux, SE France: Journal of Sedimentary Research, v. 84, p. 270–277.

Peakall, J., Amos, K.J., Keevil, G.M., Bradbury, P.W., and Gupta, S., 2007, Flow processes and sedimentation in submarine channel bends: Marine and Petroleum Geology, v. 24, p. 470–486.

Pechlivanidou, S., Cowie, P.A., Hannisdal, B., Whittaker, A.C., Gawthorpe, R.L., Pennos, C., and Riiser, O.S., 2018, Source-to-sink analysis in an active extensional setting: Holocene erosion and deposition in the Sperchios rift, central Greece: Basin Research, v. 30, p. 522–543.

Pemberton, E.A.L., Hubbard, S.M., Fildani, A., Romans, B., and Stright, L., 2016, The stratigraphic expression of decreasing confinement along a deep-water sediment routing system: outcrop example from southern Chile: Geosphere, v. 12, p. 114–134.

Pichel, L.M., Jackson, C.A-L., Peel, F., and Dooley, T.P., 2020, Base-salt relief controls salt-tectonic structural style, São Paulo Plateau, Santos Basin, Brazil: Basin Research, v. 32, p. 453–484.

Pichel, L.M., and Jackson, C.A-L., 2020, Four-dimensional variability of composite halokinetic sequences: Basin Research, v. 32, p. 1277–1299.

Pickering, K.T., and Bayliss, N.J., 2009, Deconvolving tectono-climatic signals in deep-marine siliciclastics, Eocene Ainsa basin, Spanish Pyrenees: seesaw tectonics versus eustacy: Geology, v. 37, p. 203–206.

Pickering, K.T., and Hiscott, R.N., 2015, Deep Marine Systems: Processes, Deposits, Environments, Tectonics and Sedimentation: John Wiley & Sons, 672 p.

Piper, D.J.W., and Normark, W.R., 1983, Turbidite depositional patterns and flow characteristics, Navy Submarine Fan, California Borderland: Sedimentology, v. 30, p. 681–694.

Poprawski, Y., and Basile, C., 2018, Long-lasting diapir growth history in the Basque–Cantabrian Basin (northern Spain): a review: Advances in Salt Tectonics: Observations, Applications, and Perspective, doi:10.1002/essoar.10500041.1.

Poprawski, Y., Basile, C., Agrirrezabala, L.M., Jaillard, E., Gaudin, M., and Jacquin, T., 2014, Sedimentary and structural record of the Albian growth of the Bakio salt diapir (the Basque Country, northern Spain): Basin Research, v. 26, p. 746–766.

Poprawski, Y., Basile, C., Jaillard, E., Gaudin, M., and Lopez, M., 2016, Halokinetic sequences in carbonate systems: an example from the Middle Albian Bakio Breccias Formation (Basque Country, Spain): Sedimentary Geology, v. 334, p. 34–52.

Posamentier, H.W., and Kolla, V., 2003, Seismic geomorphology and stratigraphy of depositional elements in deep-water settings: Journal of Sedimentary Research, v. 73, p. 367–388.

Prather, B.E., Booth, J.R., Steffens, G.S., and Craig, P.A., 1998, Classification, lithologic calibration, and stratigraphic succession of seismic facies of intraslope basins, deep-water Gulf of Mexico: American Association of Petroleum Geologists, Bulletin, v. 82, p. 701–728.

Prather, B.E., Pirmez, C., and Winker, C.D., 2012, Stratigraphy of linked intraslope basins: Brazos–Trinity system western Gulf of Mexico, *in* Prather, B.E., Deptuck, M.E., Mohrig, D., Hoorn, B.V., and Wynn, R.B., eds., Application of the Principles of Seismic Geomorphology to Continental-Slope and Base-of-Slope Systems: Case Studies from Seafloor and Near-Seafloor Analogues: SEPM, Special Publication 99, p. 83–109.

Pratson, L.F., and Ryan, W.B.F., 1994, Pliocene to recent infilling and subsidence of intraslope basins offshore Louisiana: American Association of Petroleum Geologists, Bulletin, v. 78, p. 1483–1506.

Prélat, A., and Hodgson, D.M., 2013, The full range of turbidite bed thickness patterns in submarine lobes: controls and implications: Geological Society of London, Journal, v. 170, p. 209–214.

Prélat, A., Hodgson, D.M., and Flint, S.S., 2009, Evolution, architecture and hierarchy of distributary deep-water deposits: a high-resolution outcrop investigation from the Permian Karoo Basin, South Africa: Sedimentology, v. 56, p. 2132–2154.

Prélat, A., Covault, J.A., Hodgson, D.M., Fildani, A., and Flint, S.S., 2010, Intrinsic controls on the range of volumes, morphologies, and dimensions of submarine lobes: Sedimentary Geology, v. 232, p. 66–76.

Pringle, J.K., Brunt, R.L., Hodgson, D.M., and Flint, S.S., 2010, Capturing stratigraphic and sedimentological complexity from submarine channel complex outcrops to digital 3D models, Karoo Basin, South Africa: Petroleum Geoscience, v. 16, p. 307–330.

Puelles, P., Ábalos, B., García De Madinabeitia, S., Sánches-Lorda, M.E., Fernández-Armas, S., and Gil Ibarguchi, J.I., 2014, Provenance of quartz-rich metamorphic tectonite pebbles from the "Black Flysch" (W Pyrenees, N Spain): an EBSD and detrital zircon LA-ICP-MS study: Tectonophysics, v. 632, p. 123–137.

Pujalte, V., Robles, S., and García-Mondéjar, J., 1986, Caracteristicas sedimentológicas y paleogeográficas del fan-delta albiense de la Formación Monte Grande y sus relaciones con el Flysh Negro (Arminza-Górliz, Vizcaya): Acta Geologica Hispánica, v. 21, p. 141–150.

Pujalte, V., Baceta, J.I., Payros, A., Orue-Etxebarria, X., and Serra-Kiel, J., 1994, Late Cretaceous–Middle Eocene Sequence Stratigraphy and Biostratigraphy of the SW and W Pyrenees (Pamplona and Basque Basins): a Field Seminar of the Groupe de Etude du Paleogene, Council of the International Geoscience Programme, IGCP Project 286, Universidad del País Vasco/Euskal Herriko Univertsitatea, 118 p., doi:10.13140/2.1.3746.6407.

Pujalte, V., Baceta, J.I., Orue-Etxebarria, X., and Payros, A., 1998, Paleocene strata of the Basque Country, W Pyrenees, N Spain: facies and sequence development in a deep-water, starved basin, *in* De Graciansky, P.C., Hardenbol, J., Jacquin, T., and Vail, P.R., eds., Mesozoic and Cenozoic Sequence Stratigraphy of European Basins: SEPM, Special Publication 60, p. 311–325.

Rat, P., 1988, The Basque–Cantabrian Basin between the Iberian and the European Plates. Some facts but still many problems: Sociedad de Geológica de España, Revista, v. 1, p. 3–4.

Remacha, E., Fernandez, L.P., and Maestro, E., 2005, The transition between sheet-like lobe and basin-plain turbidites in the Hecho Basin (South-Central Pyrenees, Spain): Journal of Sedimentary Research, v. 75, p. 798–819.

Ribes, C., Kergaravat, C., Bonnel, C., Crumeyrolle, P., Callot, J.-P., Poisson, A., Temiz, H., and Ringenbach, J.-C., 2015, Fluvial sedimentation in a salt-controlled mini-basin: stratal patterns and facies assemblages, Sivas Basin, Turkey: Sedimentology, v. 62, p. 1513–1545.

Robles, S., Pujalte, V., and García-Mondéjar, J., 1988, Evolución de los sistemas sedimentarios del margen continental cantábrico durante el Albiense y Cenomaniense, en la transversal del litoral Vizcaino: Sociedad de Geológica de España, Revista, v. 1, p. 410–441.

Robles, S., Garrote, A., and García-Mondéjar, J., 1989, XII Congreso Español de Sedimentología: Simposios y conferencias, Universidad del País Vasco, Departamento de Estratigrafía, Geodinámica y Paleontología, Bilbao.

Roca, E., Ferrer, O., Rowan, M.G., Muñoz, J.A., Butillé, M., Giles, K.A., Arbués, P., and de Matties, M., 2020, Salt tectonics and controls on halokinetic-sequence development of an exposed deepwater diapir: the Bakio Diapir, Basque–Cantabrian Basin, Pyrenees: Marine and Petroleum Geology, v. 123, 104770.

Rodriguez, C.R., Jackson, C.A-L., Rotevatn, A., Bell, R.E., and Francis, M., 2018, Dual tectonic-climatic controls on salt giant deposition in the Santos Basin, offshore Brazil: Geosphere, v. 14, p. 215–242.

Rodriguez, C.R., Jackson, C.A-L., Bell, R.E., Rotevatn, A., and Francis, M., in press, Deep-water reservoir distribution on a salt-influenced slope, Santos Basin, offshore Brazil: American Association of Petroleum Geologists, Bulletin, doi:10.1306/11182017340.

Romans, B.W., Fildani, A., Hubbard, S.M., Covault, J.A., Fosdick, J.C., and Graham, S.A., 2011, Evolution of deep-water stratigraphic architecture, Magallanes Basin, Chile: Marine and Petroleum Geology, v. 28, p. 612–628.

Rosales, I., and Pérez-García, A., 2010, Porosity development, diagenesis and basin modelling of a Lower Cretaceous (Albian) carbonate platform from northern Spain, *in* van Buchem, F.S.P., Gerdes, K.D., and Esteban, M., eds., Mesozoic and Cenozoic Carbonate System of the Mediterranean and the Middle East: Stratigraphic and Diagenetic Reference Models: Geological Society of London, Special Publication 329, p. 317–342.

Rowan, M.G., and Giles, K.A., 2021, Passive versus active salt diapirism: American Association of Petroleum Geologists, Bulletin, v. 105, p. 53–63.

Rowan, M.G., Giles, K.A., Roca, E., Arbues, P., and Ferrer, O., 2012, Analysis of Growth Strata Adjacent to an Exposed Deepwater Salt Diapir, northern Spain [Abstract]: American Association of Petroleum Geologists, Annual Convention, Long Beach, USA.

Salles, L., Ford, M., and Joseph, P., 2014, Characteristics of axially-sourced turbidite sedimentation on an active wedge-top basin (Annot Sandstone, SE France): Marine and Petroleum Geology, v. 56, p. 305–323.

Scott, E.D., Gelin, F., Jolley, S.J., Leenaarts, E., Sadler, S.P., and Elsinger, R.J., 2010, Sedimentological control of fluid flow in deep marine turbidite reservoirs: Pierce Field, UK Central North Sea, *in* Jolley, S.J., Fisher, Q.J., Ainsworth, R.B., Vrolijk, P.J., and Delisle, S., eds., Reservoir Compartmentalization: Geological Society of London, Special Publication 347, p. 113–132.

Sharp, I.R., Gawthorpe, R.L., Underhill, J.R., and Gupta, S., 2002, Fault-propagation folding in extensional settings: examples of structural style and synrift sedimentary response from the Suez rift, Sinai, Egypt: Geological Society of America, Bulletin, v. 112, p. 1877–1899.

Sinclair, H.D., 1994, The influence of lateral basinal slopes on turbidite sedimentation in the Annot sandstones of SE France: Journal of Sedimentary Research, v. 64, p. 42–54.

Sinclair, H.D., and Tomasso, M., 2002, Depositional evolution of confined turbidite basins: Journal of Sedimentary Research, v. 72, p. 451–456.

Sohn, Y.K., 2000, Depositional processes of submarine debris flows in the Miocene fan deltas, Pohang Basin, SE Korea with special reference to flow transportation: Journal of Sedimentary Research, v. 70, p. 491–503.

Sohn, Y.K., Choe, M.Y., and Jo, H.R., 2002, Transition from debris flow to hyperconcentrated flow in a submarine channel (the Cretaceous Cerro Toro Formation, southern Chile): Terra Nova, v. 14, p. 405–415.

Soto, R., Beamud, E., Roca, E., Carola, E., and Almar, Y., 2017, Distinguishing the effect of diapir growth on the magnetic fabrics of syn-diapiric overburden rocks: Basque Cantabrian Basin, Northern Spain: Terra Nova, v. 29, p. 191–201.

Soutter, E.L., Kane, I.A., and Huuse, M., 2018, Giant submarine landslide triggered by Paleocene mantle plume activity in the North Atlantic: Geology, v. 46, p. 511–514.

Soutter, E.L., Kane, I.A., Fuhrmann, A., Cumberpatch, Z.A., and Huuse, M., 2019, The stratigraphic evolution of onlap in clastic deep-water systems: autogenic modulation of allogenic signals: Journal of Sedimentary Research, v. 89, p. 890–917.

Soutter, E.L., Bell, D., Cumberpatch, Z.A., Ferguson, R.A., Kane, I.A., Spychala, Y.T., and Eggenhuisen, J., 2021, The influence of confining topography orientation on experimental turbidity currents and geological implications: Frontiers in Earth Science, v. 8, no. 540633, doi:10.3389/feart.2020.540633.

Spychala, Y.T., Hodgson, D.M., Flint, S.S., and Mountney, N.P., 2015, Constraining the sedimentology and stratigraphy of submarine instraslope lobe deposits using exhumed examples from the Karoo Basin, South Africa: Sedimentary Geology, v. 322, p. 67–81.

Spychala, Y.T., Hodgson, D.M., Prélat, A., Kane, I.A., Flint, S.S., and Mountney, N.P., 2017, Frontal and lateral submarine lobe fringes: comparing sedimentary facies, architecture, and flow processes: Journal of Sedimentary Research, v. 87, p. 75–96.

Stevenson, C.J., Jackson, C.A-L., Hodgson, D.M., Hubbard, S.M., and Eggenhuisen, J.T., 2015, Deep-water sediment bypass: Journal of Sedimentary Research, v. 85, p. 1058–1081.

Straub, K.M., Mohrig, D., McElroy, B., Buttles, J., and Pirmez, C., 2008, Interactions between turbidity currents and topography in aggrading sinuous submarine channels: a laboratory study: Geological Society of America, Bulletin, v. 120, p. 368–385.

Sumner, E.J., Peakall, J., Parsons, D.R., Wynn, R.B., Darby, S.E., Dorrell, R.M., McPhail, S.D., Perrett, J., Webb, A., and White, D., 2013, First direct measurements of hydraulic jumps in an active submarine density current: Geophysical Research Letters, v. 40, p. 5904–5908.

Sylvester, Z., Cantelli, A., and Pirmez, C., 2015, Stratigraphic evolution of intraslope minibasins: insights from surface-based model: American Association of Petroleum Geologists, Bulletin, v. 99, p. 1099–1129.

Talling, P., Masson, D., Sumner, E., and Malgesini, G., 2012, Subaqueous sediment density flows: depositional processes and deposit types: Sedimentology, v. 59, p. 1937–2003.

Teixell, A., Labaume, P., Ayarza, P., Espurt, N., de Saint Blanquat, M., and Lagabrielle, Y., 2018, Crustal structure and evolution of the Pyrenean–Cantabrian belt: a review and new interpretations from recent concepts and data: Tectonophysics, v. 724–725, p. 146–170.

Teles, V., Chauveau, B., Joseph, P., Weill, P., and Maktouf, F., 2016, CATS: a process-based model for turbulent turbidite systems at reservoir scales: Comptes Rendus Geoscience, v. 384, p. 473–478.

Vail, P.R., Mitchum, R.M., Jr., Todd, R.G., Widmier, J.M., Thompson, S., III, Sangree, J.B., Bubb, J.N., and Hatelid, W.G., 1977, Seismic stratigraphy and global changes of sea-level, *in* Payton, C.E., ed., Seismic Stratigraphy: Applications to Hydrocarbon Exploration: American Association of Petroleum Geologists, Memoir 26, p. 49–212.

Van Der Voo, R., 1969, Paleomagnetic evidence for the rotation of the Iberian Peninsula: Tectonophysics, v. 7, p. 5–56.

Vicente Bravo, J., and Robles, S., 1991a, Geometría y modelo deposicional de la secuencia Sollube del Flysch Negro (Albiense medio, norte de Bizkaia): Geogaceta, v. 10, p. 69–72.

Vicente Bravo, J., and Robles, S., 1991b, Caracterización de las facies de la transición canal–lóbulo en la secuencia Jata del Flysch Negro (Albiense Superior norte de Vizcaya): Geogaceta, v. 10, p. 72–75.

Vicente Bravo, J.C., and Robles, S., 1995, Large-scale mesotopographic bedforms from the Albian Black Flysch, northern Spain: characterization, setting and comparisons with recent analogues, *in* Pickering, K.T., Hiscott, R.N., Kenyon, N.H., Ricci Lucchi, F., and Smith, R.D.A., eds., Atlas of Deep-Water Environments: Architectural Style in Turbidites Systems: Springer, p. 216–226.

Warren, J., 1999, Evaporites: Their Evolution and Economics: Oxford, UK, Blackwell Science, 438 p.

Warren, J., 2006, Evaporites: Sediments, Resources, and Hydrocarbons: Berlin, Springer, 1035 p.

Walker, R.G., 1978, Deep-water sandstone facies and ancient submarine fans: models for exploration for stratigraphic traps: American Association of Petroleum Geologists, Bulletin, v. 62, p. 932–966.

Wang, X., Luthi, S.M., Hodgson, D.M., Sokoutis, D., Willingshofer, E., Groenenberg, R.M., 2017, Turbidite stacking patterns in salt-controlled minibasins: insights from integrated analogue models and numerical fluid flow simulations: Sedimentology, v. 64, p. 530–552.

Winker, C.D., 1996, High resolution seismic stratigraphy of a late Pleistocene submarine fan ponded by salt-withdrawal mini-basins on the Gulf of Mexico Continental slope: Offshore Technology Conference, paper OTC 8024, Proceedings, Houston, p. 619–628.

Wynn, R.B., Kenyon, N.H., Masson, D.G., Stow, D.A.V., and Weaver, P.P.E., 2002, Characterization and recognition of deep-water channel–lobe transition zones: American Association of Petroleum Geologists, Bulletin, v. 86, p. 1441–1462.

Wu, N., Jackson, C.A-L., Johnson, H.D., Hodgson, D.M., and Nugraha, H.D., 2020, Mass-transport complexes (MTCs) document subsidence patterns in a northern Gulf of Mexico salt minibasin: Basin Research, v. 32, p. 1300–1327.

Zamora, G., Fleming, M., and Gallastegui, J., 2017, Salt tectonics within the offshore Asturian Basin: North Iberian Margin, *in* Soto, J.I., Flinch, J.F., and Tari, G., eds., Permo-Triassic Salt Provinces of Europe, North Africa and the Atlantic Margins: Elsevier, p. 371–393.

Received 28 March 2020; accepted 12 October 2020.